Molecular Dynamics Studies of Lipid Monolayer and Bilayer Systems

by

Bin Liu

A thesis
presented to the University of Waterloo
in fulfillment of the
thesis requirement for the degree of
Doctor of Philosophy
in
Chemistry

Waterloo, Ontario, Canada, 2016

I hereby declare that I am the sole author of this thesis. This is a true copy of the thesis, including any required final revisions, as accepted by my examiners.

I understand that my thesis may be made electronically available to the public.

Abstract

Lipids are a crucial ingredient of biomembranes in cells, and they play a pivotal role in many chemical and biological processes. Lipid based structures, such as lipid monolayers and lipid bilayers, both natural and artificial, are gaining importance and popularity in drug delivery. In this thesis, the main interest is on using molecular modeling and atomistic molecular dynamics simulations to study lipid monolayers and bilayers, and their physical properties and interactions with an antibiotic molecule called daptomycin. This thesis is composed of the research results from two projects.

The first project focuses on an atomistic molecular dynamcis study of lipid Langmuir monolayers composed of both pure zwitterionic dipalmitoylphosphatidylcholine (DPPC) and a mixture of DPPC and cationic cetyltrimethylammonium bromide (CTAB). The cationic CTAB lipids have been found to have significant condensing effect on the DPPC / CTAB monolayers, i.e., at the same surface tension or surface pressure, monolayers with higher CTAB molar fraction have smaller area per lipid. With this condensing effect, the DPPC / CTAB monolayers are also able to achieve negative surface tension without introducing buckling into the monolayer structure. The condensing effect is caused by the interplay between the cationic CTAB headgroups and the zwitterionic phosphatidylcholine (PC) headgroups which has electrostatic origin. Moreover, detailed analysis of the structural properties of the monolayers, such as the density profile analysis, hydrogen bonding analysis, chain order parameter calculations and radial distribution function calculations were also performed for better understanding of cationic DPPC/CTAB monolayers. A chapter is dedicated to the discussion of the mean and Gaussian curvatures of the pure DPPC and DPPC/CTAB mixture monolayers.

In the second project, MD simulations were employed to study the atomistic details of the antimicrobial activities of daptomycin, a cyclic anionic lipopeptide which treats infections caused by Gram-positive bacteria, with emphasis on its interactions with a model bacteria membrane. Despite having a net negative charge, it is selective against negatively charged bacterial membranes. It has been established that daptomycin's antibiotic activity is based on targeting bacterial membranes and that this antibacterial activity depends on calcium ions. Importantly, however, both the precise role of ions and the physical mechanisms responsible for daptomycin's action remain poorly understood. We investigate these issues using three types of molecular dynamics simulations: free energy calculations for a single daptomycin, unbiased simulations for daptomycin tetramers and micellation of daptomycin both in the absence and presence of calcium ions.

Acknowledgements

Thank-you to my family for your tremendous support. Ruochen, you are the brightest light ever in my life. My love for you lets me transcend all the difficulties I encountered during the writing of this thesis. To my parents, thank you both for the spiritual and financial support. Without your support, finishing my PhD would have been impossible for me.

A great thanks to my supervisor, Prof. Mikko Karttunen, for all of the support throughout my PhD and for providing a terrific research environment. My success as a graduate student is mostly due to his mentoring.

I would like to thank former SoftSimu group members and collaborators from around the world, and specifically my former colleague and mentor, Dr. Matthew Hoopes, from whom I learned a tremendous amount of techniques that are essential to my research. Special thanks to Prof. Toby Zeng, who gave me invaluable help in both research and my personal life. Thank you, Trang, for your great contribution of time and effort to help me cope with the pressure during the last year of my program. Special thanks to Pranav and Yuriy for proofreading this thesis.

Thanks to my advisory committee and the support staff at the University of Waterloo. Many thanks to Prof. Pierre-Nicolas Roy for your triple help, your valuable and inspiring advice on my research, your mentoring as my instructor of CHEM740, and your iMac and office space for my first year at UW. I would also like to thank Prof. Elizabeth Meiering and Prof. Goddard of the University of Guelph for your commitment of time as my advisory committee members.

I would like to thank Dr. Semen Yesylevskyy who provided the Pteros source code and the curvature evaluation plugin which are essential for obtaining the results in Chapter 4.

For funding, I thank the University of Waterloo, the Waterloo Institute of Nanotechnology, NSERC, the Government of Ontario, and Compute Canada. Thanks to Compute Canada for computer resources and their amazing support staff.

Dedication

To Ruochen, my angel daughter.

Table of Contents

List of Tables

List of Figures

Chapter 1

Introduction

The theme of the first half of this thesis is employing molecular modeling approaches, or more specifically molecular dynamics (MD) methods to investigate lipid based structures and materials, with the aim of facilitating the design of packaging material for drug delivery nanocarriers, with the help of massively parallel computer simulations. MD simulations were performed for a detailed atomistic study of lipid Langmuir monolayers composed of both pure zwitterionic dipalmitoylphosphatidylcholine (DPPC) and a mixture of DPPC and cationic cetyltrimethylammonium bromide (CTAB). The purpose of the study is to investigate how the composition of the DPPC/CTAB monolayers affects their structural and electrostatic properties in the liquid-expanded phase.

The second half of this thesis focuses on using very similar molecular modeling approaches to study the mechanism of daptomycin's antimicrobial activities. Daptomycin is a cyclic anionic lipopeptide which treats infections caused by Gram-positive bacteria. But the full picture of its antimicrobial activities is yet to be revealed. Again we employed atomistic MD studies to reveal the behavior and structural changes of daptomycin in one of the key stages of the process of killing bacteria. This chapter provides the basic theoretical and experimental background knowledge for the rest of this thesis. A lot of background will be discussed in the next chapter, Molecular Dynamics Simulation of Surfactant Monolayers, including details on parametrizing lipid molecules, simulation box setup and techniques of running monolayer simulations.

1.1 The Role of Lipid-Based Structures in Modern Drug Delivery and Drug Design

According to the World Cancer Report 2014[1], cancer is one of the most serious threats to human health and in 2012 alone it claimed 8.2 million human lives[1]. Yet the threat of cancer shows no sign of slowing down. According to the estimation of the World Health Organization in the World Cancer Report 2014[1], the number of new cases is expected to rise to an annual 19.3 million by 2025 from an estimated 14 million new cases in 2012.

The high death rate of cancer poses a tremendous challenge for researchers who look for new cancer treatment methods. Even with the rapid advance of cancer treatments, such as surgery and radiation therapy, drug treatment remains one of the most available and practical approaches for patients.

Most of the current drug treatments for clinical use involves oral ingestion or intravascular injection of low molecular mass drug molecules into the human body through blood circulation. The most serious issue is that only a small portion of the drug molecules reaches the pathological site to be treated, with the vast majority of the dose (can be as high as 99% in some chemotherapy) unleashing their toxicity on healthy human cells[2]. Patients and doctors are facing a difficult and unfortunate dilemma: if the dosage of the cancer treatment drug is too low, the portion of the drug molecules that directly attacks the pathological site will be insufficient to be effective. If the dosage is too high, the side effect caused by the toxicity will be too high for the patient to bear, sometimes outweighting the benefit of quenching the growth of the pathological site. What worsens the situation is that a lot of clinically approved drugs and development candidates for cancer treatment possesses the unfortunate characteristic of high hydrophobicity and as a result, being poorly soluble in an aqueous environment[3, 4]. The intrinsic hydrophobicity makes their clinical use challenging as serious side effect such as embolization of blood capillaries can develop[5]. Hydrophobicity refers to the physical property of a molecule that shows repulsive tedency against a mass of water. Hydrophobic molecules are usually non-polar and, thus, prefer other neutral molecules and non-polar solvents. Hydrophobicity is an entropic effect. A hydrophobic molecule in water disrupts the hydrogen bonding network of water and leads to water forming a clathrate-like structure around the hydrophobic molecule. The structure formed is more ordered and entropically unfavorable than free water molecules, as the water molecules try to arrange themselves to interact as much as possible with themselves.

Nucleic acids based cancer treatment is an emerging field in the last two decades[6]. Ribonucleic acid, or RNA was once understood as simply an intermediate between deoxyri-

bonucleic acid (DNA) and protein[7]. This picture of RNA's functionality changed drastically in early 1980s-1990s due to the discovery of catalytic RNAs[8] and RNA interference[9]. These two important events in the RNA research field led to an explosion of new RNA-based therapeutics, such as RNAi, ribozymes and aptamers[10]. One of the most promising RNA based cancer therapeutics is small interfering RNAs (siRNAs) which work by the mechanism of RNA interference (RNAi), i.e., interfering with (silencing) the expression of specific genes of cancer cells. However the daunting task of delivering siRNAs into the cytoplasm of the targeted cancer cells preludes to the promising employment of the RNAi mechanism to decimate the targeted cancer cells. There are several major hurdles to an effective delivery of siRNAs to the cytoplasm of the targeted cancer cells, despite the fact siRNAs are relatively small (about 13 kDa)[11, 12]. First, siRNAs are intrinsically unstable *in vivo* due to the plethora of ribonucleases in serum and in cells[5, 10]. Second, siRNAs have a short half-life caused by the rapid renal clearance by the kidneys and the capture by the mononuclear phagocytic system (MPS) in the liver[13]. Third, siRNAs are negatively charged and hydrophilic which prevent them from easily crossing the cell membrane[10].

The strategy of targeted drug delivery was envisaged by the pioneer Paul Ehrlich, the founder of chemotherapy, more than one century ago[14]. The ultimate goal of targeted drug delivery is concentrating drug molecules in the pathological site while reducing the relative concentration attacking healthy cells. One of the latest trends in targeted drug delivery is using nanoparticles, also called nanocarriers as the delivery agent because once they are assembled in uniform and well-defined size and shape, they could possess the ability to cross the membranes of cancer cells while minimizing the probability of unleashing the packaged drug molecules into undesirable sites, i.e., healthy cells[15, 16]. For poorly soluble drug molecules, nanocarriers can be designed to solubilize them as well as protecting them from getting metabolically destroyed by the liver. It has been shown that nanocarriers can be meticulously engineered to possess the following characteristics as siRNA delivery agents. First, they can be stable with direct contact with nucleases. Second, their size can be carefully chosen and implemented in production to elude the renal clearance by the kidneys and the capture by the mononuclear phagocytic system (MPS) in the liver[5]. It is worth mentioning that the threshold of the renal clearance sets the lower limit for the size of nanocarriers (about 5.5 nm[17]) while the threshold of the capture by the MPS sets the upper limit. Various studies show the ideal range for the size of the drug delivery nanocarriers is 50 nm - 200 nm which is large enough to escape the renal clearance but small enough to avoid the uptake by the MPS in the liver[5, 13, 18]. Third, they can balance the negative charges of the siRNAs by carrying positive charges, which makes the entire siRNA/nanocarrier entity either slightly positively charged or slightly negatively charged[19]. Fourth, they can protect siRNAs from being recognized by the immune system

as well as avoiding non-specific interactions with serum proteins.

There are several candidates as promising packaging material for designing nanocarriers as the delivery vehicle for drugs and siRNAs, among which lipid based structures and materials received much attention. And they are the focus of this thesis. Lipids as an essential component of nanocarriers can be engineered into functional structures to have the favorable characteristics mentioned above to deliver the wrapped drugs or siRNAs into the desirable sites. First, lipids can wrap into structures, such as micelles and liposomes, to protect drugs and siRNAs during blood circulation and/or improve the water solubility of drugs with high hydrophobicity. As Figure 1.1a indicates, micelles are spherical structures formed by amphiphilic lipid molecules in aqueous solutions. The formation of micelles is spontaneous only when the concentration of amphiphilic lipid is greater than the critical micelle concentration (CMC), and the temperature of the system is greater than the critical micelle temperature, or Krafft temperature[11, 20]. The polar (hydrophilic) headgroups form the surface of micelles in direct contact with water and the nonpolar (hydrophobic) tails are hidden inside and stay away from water. Figure 1.1b shows a simple diagram for a liposome which is an artificial vesicle composed of two layers of lipids. The hydrophilic polar headgroup of the outer layer faces the aqueous environment, and those of the inner layer faces inwards. As both micellar and liposomal structures have hydrophilic parts facing outwards, the nanocarriers based on them are usually water soluble. Second, nanocarriers can be engineered to have cationic lipids as its components aiming to provide electrostatic stabilization[21]. Third, lipid containing micelles and liposomes loaded with drugs can be complemented with targeting moieties to achieve active targeting to cancer cells. Figure 1.1c shows a micellar structure with drug molecules as its payload and its surface linked to three targeting moieties, i.e., antibody, receptor targeted ligands, and cell penetrating function for intracellular targeting. The micellar structure usually contains not only lipids, but also polymeric compound such as poly(ethylene glycol) (PEG) to achieve desirable characteristic [5, 21, 22, 23]. The size of the lipid containing nanocarriers with micellar or liposomal structures ranges from dozens of nanometers to several hundred nanometers[23, 24, 25, 26, 27]. Therefore these nanocarriers are not prone to encounter the renal clearance or be uptaken by the MPS in the liver.

The design and application of lipid containing micelles and liposomes as drug delivery nanocarriers require in-depth knowledge and understanding of their physical and chemical properties. The "base" structures for lipid containing micelles and liposomes which are lipid monolayers and bilayers respectively provide simplified models to capture the essential physical and chemical properties of them and faciliate both experimental and simulational studies. The MD simulation works presented in this thesis focus on cationic mixture lipid monolayers which can be seen as a simplified model for cationic lipid containing

micelles. It is worth mentioning though we simulated planar monolayers, they are sound approximations to the micellar structure of the lipid based nanocarriers discussed above, as the relatively large size of the micellar structure dictates the curvature's effect is relatively small for a local patch which can be approximately regarded as a planar monolayer[28].

1.2 The Molecular Dynamics Method

In this section, a brief introduction to the molecular dynamics methods is presented. Much of the content is a summary of several in-depth literatures[29, 30] on the molecular dynamics method. The GROMACS specific details can be found in the GROMACS manual (http://www.gromacs.org/Documentation/Manual).

1.2.1 Molecular Modeling of Biological Systems

Before we proceed to the discussion of the molecular dynamics method in detail, a broader overview of the molecular modeling of biological systems, which includes the molecular dynamics method as one of the most prominent approaches, is presented. Tamar Schlick defines molecular modeling as "the science and art of studying molecular structure and function through model building and computation"[31]. The central idea of molecular modeling is using a simplified description (model) of the molecules of an interesting system to compute the evolution of the system with the passage of time. The model should be able to capture both the internal interactions of the system and the interactions with the environment. Except for a very limited number of very small pedagogical molecular modeling cases which can be solved by hand, such as covalent bonding in some diatomic molecules (e.g. H_2), molecular modeling inevitablly involves computer simulations for all physical, chemical and biological systems of decent size.

A molecular modeling study usually involves three steps. First, modeling of the molecules of interest is performed to describe interactions in the system. Second, the evolution of the molecular system of interest is mimicked by computer simulation with the underlying model of the molecules accomplished in the first step. Third, analysis is performed to investigate the physical or chemical properties of interest.

The strength of molecular modeling is that one can directly observe the microscopic interactions and processes of the molecular system of interest, which could be difficult or even impossible for experimental studies to accomplish, usually due to the temporal and/or spatial limitations. Take our own study of daptomycin's spontaneous binding to

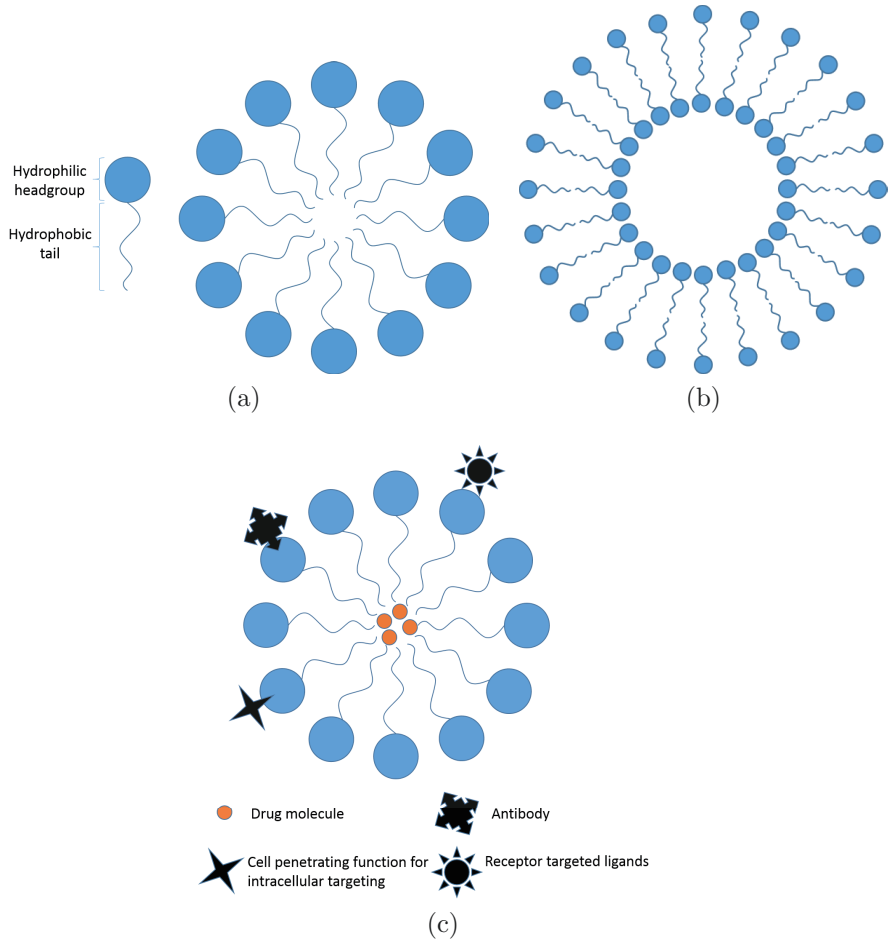

Figure 1.1: (a) A simple diagram for a micelle composed of a monolayer of amphiphilic lipids. The hydrophilic polar headgroup faces the aqueous environment and the hydrophobic nonpolar tails hides inside. In reality, water molecules are not perfectly excluded from the interior of the micelle. (b) A simple diagram for a liposome composed of a bilayer of amphiphilic lipids. Compared to a micelle, a liposome is a small artificial vesicle that has two layers of amphiphilic lipids. The hydrophilic polar headgroup of the outer layer faces the aqueous environment, and those of the inner layer faces inwards. (c) A micelle loaded with drug and targeting moieties at its surface. In real cases, the micelle could be either polymeric or lipid-based or the compound of both. The three targeting moieties may or may not exist at the same time on the same micelle surface[5].

the surface of a model bacterial membrane as example. Daptomycin is a cyclic anionic lipopeptide which treats infections caused by Gram-positive bacteria. Daptomycin gains its significance as Gram-positive pathogens rapidly acquire resistance against other antibiotics, e.g. methicillin-resistant *Staphylococcus aureus*[32]. The bacterial membrane generally differs from the eukaryotic membrane by having a significant concentration of phosphatidylglycerol lipids[33], which was properly reflected in our model. Upon the binding (Figure 1.2), hydrogen bonds develop between daptomycin and the lipids in the model bacteria membrane, and the daptomycin undergoes a structural change compared to its free state in water, which can be directly observed and analyzed in great detail in our molecular modeling approaches. To our best knowledge, though experimental measures such as NMR [34] have the capability to indirectly observe these processes, no currently existing experimental measures can directly observe them (Figure 1.2). In other words, molecular modeling approaches can provide the unparalleled temporal and spatial resolution of many microscopic molecular interactions and processes.

Molecular modeling, while providing indispensable benefit and usefulness for many molecular systems, also faces some limitations. Our own study of daptomycin's antimicrobial activities is a good example in which both the size of modeled system and the time scale of molecular process we can simulate is severely limited by the computational power we can employ. The bacterial membrane is modeled by only a few hundred lipids, which is almost negligible compared to the number of lipids in a real bacterial membrane, though this issue can be addressed by using periodic boundary condition to a large extent. We will talk about periodic boundary condition later in Section 1.2.6. The more challenging issue is the time scale of molecular process we can simulate, which almost poses as an intractable obstacle which prevents us from studying many molecular process. The process of daptomycin killing bacteria takes several minutes[35] to finish, in which some key stages of daptomycin's effect such as the aggregation of daptomycin in bacteria membrane and the flipping of daptomycin clusters occur at a similar time scale[36]. However we can only achieve simulated trajectories of daptomycin interacting with model bacteria membrane up to several microseconds. The size of the systems and the time scale of the trajectory we can achieve are typical for modern MD simulations. The current world leading level of MD simulations was done for an influenza virus particle on a mammalian membrane (approximately 120 nm)[37]. They simulated more than 10 million particles for several microseconds of simulated time. There is a huge gap between the time scale we can simulate and the time scale at which the real molecular or biological process occurs. The current limitation of molecular modeling also indicates one of the key directions for the future development of molecular modeling, i.e., simulating larger molecular systems at a much longer time scale. Also multiscale modeling is often employed to achieve the bal-

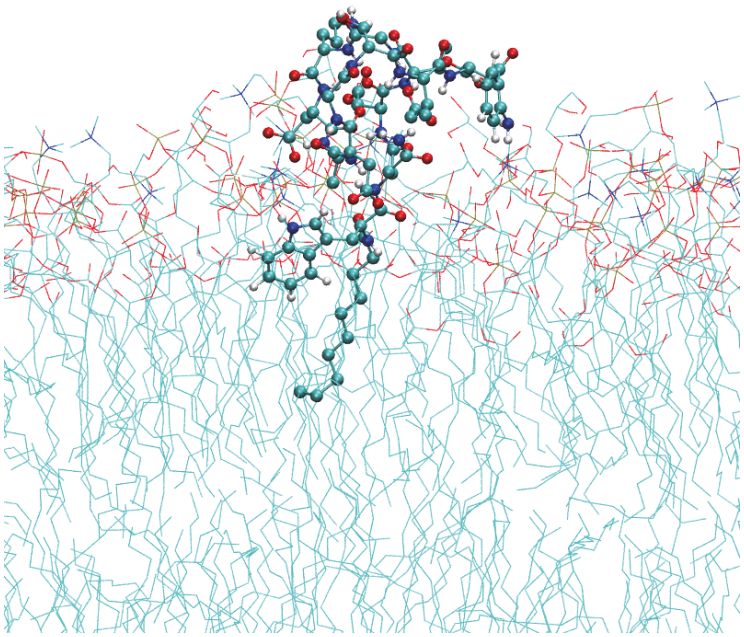

Figure 1.2: An antimicrobial daptomycin molecule in the united atom representation (shown as sticks and balls) bound to the surface of a model bacteria membrane (shown as lines).

ance between speed and accuracy[38]. For example, *ab initio molecular dynamics*[39] can be used to study a critical region of a system where chemical reactions (bond formation and breaking) occur. Outside the critial region, atomistic *classical molecular dynamics* or even coarse-grained *classical molecular dynamics*[40] can be applied to reduce the computational cost while offering acceptable accuracy. Advanced sampling techniques, such as metadynamics[41], are also extensively used to enchance the sampling in the phase space which is difficult for regular MD to reach in many cases.

1.2.2 Molecular Dynamics

Molecular dynamics (MD) simulations numerically solve Newton's equation of motion, Eq.1.1, for particles (indexed by subscript i) of an interesting system in a discretized fashion. Here we refer the most elementary and indivisible constituent of a system studied

by MD as a particle, not an atom. The reason is MD simulations can not only simulate a system of atoms, but also a system comprising of other indivisible constituent such as beads in the coarse grained approaches. Therefore particle is a more suitable and broader concept than atom to describe the most elementary and indivisible constituent of a MD simulated system.

$$F_i = ma_i \tag{1.1}$$

The force on each particle can be evaluated by taking the partial derivatives of an empirical potential energy function $V = V(r_1, r_2, ..., r_i)$, if the analytical form is available.

$$F_i = -\frac{\partial V}{\partial r_i} \tag{1.2}$$

Here the potential energy function is empirical because it is predetermined by the force field employed, not from real-time electronic structure calculations. A set of carefully designed empirical potential energy functions that fit to either experimental data or quantum chemistry calculations or both is called a force field. It is one of the most important determining factors in a MD simulation. There are many algorithms for discretizing Eq. 1.1 in conjunction with Eq. 1.2 to derive updated positions and velocities for each particle. These algorithms are named numerical integrators. One of the most widely used integrators which was also employed for all the MD simulations in this thesis, is the leap-frog integrator[42].

The general procedure of update scheme in a MD simulation is:

1. Provide an initial configuration of the particle coordinates to the MD engine as well as run parameters and a topology file which describes the interactions (bonded and non-bonded) between the particles. The initial configuration of the particle coordinates is usually generated artificially, or assembled from an experimentally determined structure or the output of another MD simulation. The initial velocities can be sampled from a Maxwell-Boltzmann distribution which defines the distribution of speeds for a molecular system at a certain temperature:

$$\frac{dN}{N} = \left(\frac{m}{2\pi k_B T}\right)^{1/2} e^{\frac{-mv^2}{2k_B T}} dv \tag{1.3}$$

where dN/N is the fraction of molecules moving at velocity v to $v + dv$, m is the mass of the molecule, k_b is the Boltzmann constant, and T is the absolute temperature.

2. Evaluate the forces on each particle by using their coordinates and the force field.

3. Use a numerical integrator to update the coordinates of each particle.

4. If a thermostat and/or a barostat is present, another treatment of the coordinates and the velocities are needed to achieve the desirable temperature and pressure.

5. Repeat Steps 2 to 4 to generate a trajectory with periodic output of the coordinates and velocities of the particles and other state data, e.g., energies and virials.

The periodic time interval for performing a cycle of Steps 2 to 4 is called a time step, which must be carefully selected to ensure the accuracy and non-divergence behavior of the numerical integrator (not too large), while keeping the computational cost of MD simulation acceptable (not too small).

The molecular dynamics method described above is called *classical molecular dynamics* in which the forces are calculated by using a force field and the motions of the particles in the system are treated under the frame of classical (i.e., non-quantum) mechanics[43]. The *classical molecular dynamics* is distinctive from the *ab initio molecular dynamics* in which the forces are calculated from the electronic structure of the system[39]. The *ab initio molecular dynamics* has the superiority of investigating chemical reactions as breaking and formation of chemical bonds are allowed, which is essentially impossible for the *classical molecular dynamics*. It should be noted that the plain *ab initio molecular dynamics* can treat the ground state of the quantum molecular system only. In order to deal with bond breaking and formation, excited states need to be included using specific methods, such as the GW-BSE method[44]. The major drawback of the *ab initio molecular dynamics* is the prohibitive computational cost, which confines its application to small systems (typically dozens of atoms at several nanoseconds of simulated time[45]). It is worth mentioning semi-empirical methods were developed to combine the strength of both the *classical molecular dynamics* and the *ab initio molecular dynamics*, such as ReaxFF (for reactive force field) [46] which can treat chemical reactions with lower computational cost compared to the pure *ab initio molecular dynamics*. For biological systems such as lipid monolayers and bilayers we investigated in this thesis, we have to resort to the *classical molecular dynamics* which allows us to study large systems consisting of hundreds of thousands, or even millions of particles[37]. All the MD simulations in this thesis are *classical molecular dynamics*.

1.2.3 Numerical integrators

The leap-frog integrator[42] mentioned above is a variant of the Verlet algorithm[47] family based on the idea of Taylor expansion, which was proposed by Loup Verlet almost half a century ago[47]. The vanilla Verlet algorithm which is also called coordinate Verlet algorithm, the position $r(t+\Delta t)$ at $t+\Delta t$ is evaluated from the positions $r(t)$ and $r(t-\Delta t)$,

and the acceleration at time t:

$$r(t-\Delta t) = r(t) - \Delta t\frac{d}{dt}r(t) + \frac{(\Delta t)^2}{2}\frac{d^2}{dt^2}r(t) - \frac{(\Delta t)^3}{6}\frac{d^3}{dt^3}r(t) + \mathcal{O} \tag{1.4}$$

$$r(t+\Delta t) = r(t) + \Delta t\frac{d}{dt}r(t) + \frac{(\Delta t)^2}{2}\frac{d^2}{dt^2}r(t) + \frac{(\Delta t)^3}{6}\frac{d^3}{dt^3}r(t) + \mathcal{O} \tag{1.5}$$

Adding these two equations to obtain

$$r(t+\Delta t) \approx 2r(t) - r(t-\Delta t) + \frac{(\Delta t)^2}{m}F(t) \tag{1.6}$$

where m is the mass of the particle. The major weakness of the coordinate Verlet algorithm is the velocity is obtained as the difference of two coordinates of the same magnitude:

$$v(t) \approx \frac{1}{2\Delta t}[r(t+\Delta t) - r(t-\Delta t)] \tag{1.7}$$

The truncation error is of the order $(\Delta t)^4$ for the new coordinates and $(\Delta t)^2$ for the velocity.

The velocity Verlet algorithm[48] was proposed to address the weakness of the coordinate Verlet algorithm:

$$r(t+\Delta t) \approx r(t) + \Delta t v(t) + \frac{1}{2}(\Delta t)^2\frac{F(t)}{m} \tag{1.8}$$

$$v(t+\Delta t) \approx v(t) + \Delta t\frac{F(t)+F(t+\Delta t)}{2m} \tag{1.9}$$

The advantage of the velocity Verlet algorithm is the new velocity is updated after the new coordinate is derived and thus based on the new forces.

The leap frog algorithm uses positions r at time t and velocities v at time $t - \frac{1}{2}\Delta t$:

$$v(t+\frac{1}{2}\Delta t) \approx v(t-\frac{1}{2}\Delta t) + \frac{\Delta t}{m}F(t) \tag{1.10}$$

$$r(t+\Delta t) \approx r(t) + \Delta t v(t+\frac{1}{2}\Delta t) \tag{1.11}$$

The formal derivation of the Verlet algorithm family is based on the Liouville formalism from statistical mechanics and the Trotter theorem[49]. The strength of the Verlet algorithms lies on their time reversibility[47] and symplecticity[50]. Time reversibility is

important because it enhances conservation of energy, angular momentum, among other conserved quantities. Symplecticity means conservation of the volume in phase space, in the absence of round-off error. This favorable property guarantees that there is no severe energy drift even in long time scales, and truncating and round-off errors will not change ensemble behavior even with different trajectories when the Verlet algorithm is used. By contrast, some other numerical integrators are neither time reversible nor symplectic, leading to overall energy drifts for long time scales[51].

1.2.4 Force Field

An empirical force field for describing the potential energy is one of the most important, if not the most important ingredients in a MD simulation.

$$V(r^N) = \sum_{bonds} \frac{k_i}{2}(l_i - l_{i,0})^2 + \sum_{angles} \frac{k_i}{2}(\theta_i - \theta_{i,0})^2 + \sum_{torsions} \frac{V_n}{2}(1 + cos(n\omega - \gamma) + \sum_{i=1}^{N} \sum_{j=i+1}^{N} \frac{q_i q_j}{4\pi\epsilon_0 r_{ij}} + 4\epsilon_{ij}\left[\left(\frac{\sigma_{ij}}{r_{ij}}\right)^{12} - \left(\frac{\sigma_{ij}}{r_{ij}}\right)^{6}\right]\right) \tag{1.12}$$

Equation 1.12 is a general form for a force field[29, 30]. Certain terms, e.g., the third term for torsion, can take a variety of other forms. The first three terms are called bonded terms, which define the intramolecular terms. The fourth term is called the non-bonded term, which describes the non-bonded interactions between particles in the system, i.e., the long-ranged electrostatic interactions and the short-ranged van der Waals interactions. The non-bonded interactions usually take a form of $\frac{1}{r^N}$. If $N > 1$, the interaction is a short-ranged one. If $N \leqslant 1$, it is a long-ranged one.

The first term is called bond stretching interaction (Figure 1.3A), in which k_i is the force constant, and $l_{i,0}$ is the equilibrium bond distance for a certain type of bond. In practical MD simulations, and also in all our MD simulations presented in this thesis, the bond stretching is constrained to allow a larger MD time step. The use of bond stretching constraint has been proved to be theoretically justified and reliable in practice. Without bond stretching constraint, the MD time step can usually not be larger than 1.4 fs, while with it, the MD time step can be selected to be 2 fs for atomistic MD simulations, i.e., not coarse-grained MD simulations in which the time step is usually much larger[52]. The most commonly used constraint algorithm with the GROMACS package[53] is LINCS[54] for any bonds except those in water and SETTLE[55] for water bonds and angles.

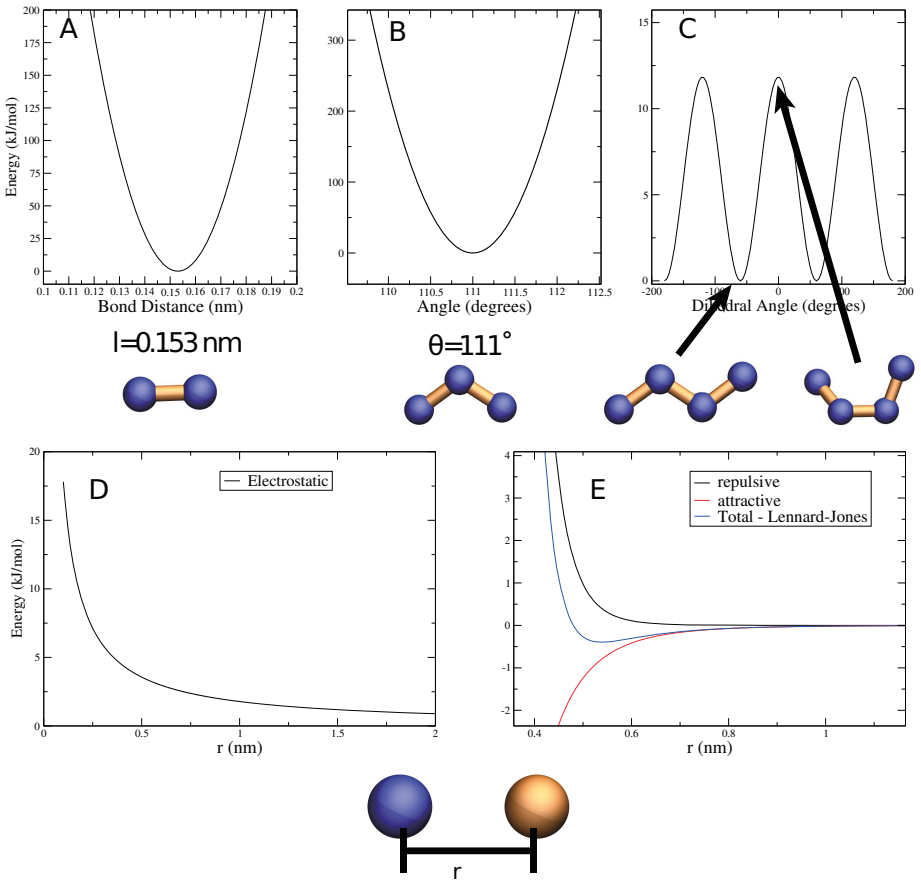

Figure 1.3: The potential functions described in Eq.1.12. (A) Bond stretching, (B) Bond bending, (C) Torsion, (D) Electrostatic interactions for 2 positive charges in a medium with a dielectric constant of 78, (E) van der Waals interactions. Courtesy of Dr. Drew Bennett.

The second term is called bond bending interaction (Figure 1.3B), or angle potential, which is defined over three consecutively bonded particles (atoms or beads) in a molecule. Again k_i is the force constant, and $\theta_{i,0}$ is the equilibrium angle. The 2 fs time step in atomistic MD simulations is chosen because as the bond stretching, the motion of the highest frequency constrained, the next fastest mode of motion is bond bending which requires no less than 2 fs time step to ensure the accuracy of the numerical integrators[54].

The third term is called the torsional interaction or the dihedral potential between four consecutively bonded particles (atoms) in a molecule to describe the dihedral potential for the angle between the plane formed by the first three atoms and the plane formed by the last three atoms (Figure 1.3C). V_n is the force constant for the dihedral potential, ω is the dihedral angel, γ is the phase factor. The dihedral potential is different from the bond stretching and bond bending potentials by having multiple minima, as demonstrated in Figure 1.3C. The number of minima is associated with n.

The fourth term describes the electrostatic interactions, where q is the charge carried by a particle, r_{ij} is the distance between two charged particles, and ϵ_0 is the dielectric constant. This is usually the most computationally costly interaction to evaluate in a MD simulation (Figures 1.3D and E), and numerous techniques have been developed to address the issue[56]. A naive estimation of the computational cost of directly evaluating all the non-bonded interactions scales with N^2 when N is the number of particles in the system. But this is actually not true because a periodic boundary condition is usually used in a MD simulation. Therefore there are essentially an infinite number of particles in the system, requiring the evaluation of non-bonded interactions for an infinite number of pairs, especially for long-ranged electrostatic interactions. Long-range electrostatic schemes are mandatory to reduce the computational cost. By using modern algorithms treating electrostatic interactions, such as the particle mesh Ewald (PME) method[57] and the particle-particle particle-mesh (PPPM) method[58], the scaling of the computational cost can be reduced to $\mathcal{O}(N \log N)$, where N is the number of charges in the simulation box. The scaling $\mathcal{O}(N \log N)$ is essentially determined by the underlying Fast Fourier Transformation (FFT) algorithm[59]. The correct and efficient protocol for the treatment of the electrostatic interactions has been discussed in-depth in Ref.[60, 61]. The poor treatment of the electrostatic interactions can cause artifacts in MD simulations, as reported in Ref.[62, 63, 64]. Simple cut-off can introduce large artifacts such as affecting structural properties of a variety of atomistic molecular systems like water, and lipids, which can be demonstrated by the wrong behavior of the radial distribution function (RDF) (see the detailed discussion in Ref.[56, 65, 66]). Simple cut-off should be avoided. It should be noted that q_i and q_j in Eq. 1.12 are partial charges of the corresponding atoms, which are usually calculated by performing quantum chemistry calculations on the molecule of

interest in an environment that is similar to the MD simulation setup. The most commonly used long range treament for electrostatic interactions is the particle mesh Ewald method (PME)[57], which is also used for all our MD simulations. With the PME algorithm, a cutoff is selected (in our case, 1.3 nm) to divide the evaluation of electrostatic interactions into a real space part, i.e., direct evaluation for charge pairs within the cutoff, and a reciprocal part in which the charges are placed on a grid to which the Fourier transformation is applied to sum up the reciprocal space contribution more efficiently.

In all our simulations, neighbor searching with group cutoff scheme was performed every 5 MD steps to generate a neighbor list, with only interactions between atoms within the cut-off calculated. The intramolecular non-bonded interactions are neglected between atoms separated by more than three bonds and the intramolecular non-bonded interactions between atoms separated by one, two or three bonds have already been accounted by the first three terms in Eq. 1.12.

The fifth term describes the van der Waals interactions, where r_{ij} is the distance between two particles, and ϵ_{ij} and σ_{ij} are the van der Waals parameters. As for the treatment of the van der Waals interactions in all our MD simulations, We employed a cutoff of 1.0 nm and shifting starting from 0.9 nm instead of plain cutoff as the latter may be a source of artifacts[62, 67, 68]. The van der Waals interaction between two atoms can also be rewritten into:

$$V_{VdW}(r_{ij}) = \frac{C_{ij}^{(12)}}{r_{ij}^{12}} - \frac{C_{ij}^{(6)}}{r_{ij}^{6}} \tag{1.13}$$

The ϵ and σ in Equation 1.12 or $C_{ij}^{(12)}$ and $C_{ij}^{(6)}$ parameters are different for different atom types and different force fields. In the OPLS force field[69], the van der Waals parameters were optimized through statistical mechanical Monte Carlo simulations and fitting to thermodynamical and structural data, such as densities, heats of vaporization and free energies of hydration. In the Amber force fields[70], van der Waals terms for various *sp2* and *sp3* carbon, as well as aliphatic and aromatic hydrogen atom types, were obtained through comparison of simulated alkene and benzene liquids with experimental data. Most of the remaining van der Waals parameters were taken from OPLS. The GROMOS force fields put more emphasis on optimizing the free enthalpy of hydration by varying both the partial charges and the van der Waals parameters[71, 72, 73]. Normally the standard geometric averaging combination rule:

$$\begin{aligned} C_{ij}^{(6)} &= (C_{ii}^{(6)} C_{jj}^{(6)})^{1/2} \\ C_{ij}^{(12)} &= (C_{ii}^{(12)} C_{jj}^{(12)})^{1/2} \end{aligned} \tag{1.14}$$

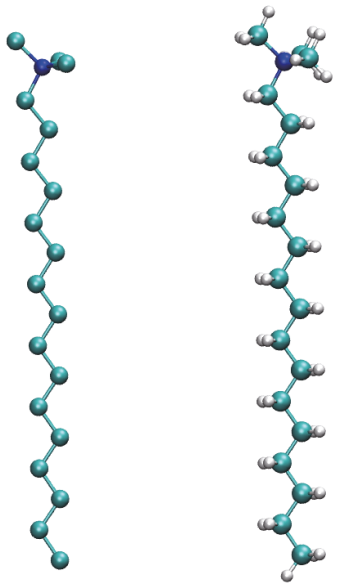

Figure 1.4: The united atom model (left) versus the all-atom model (right) for the CTAB molecule. The non-polar hydrogen atoms (white) presented in the all-atom model are absorbed into their adjacent carbon atoms (cyan) to form hydrocarbons in the united atom model. Nitrogen is shown in blue.

is used for heteroatomic van der Waals interactions, or, alternatively the Lorentz-Berthelot rules can be used:

$$\begin{aligned} \sigma_{ij} &= \frac{1}{2}(\sigma_{ii} + \sigma_{jj}) \\ \epsilon_{ij} &= (\epsilon_{ii}\epsilon_{jj})^{1/2} \end{aligned} \tag{1.15}$$

But a set of special parameters can be defined for certain pairs of atom-types[71, 72, 73]. Different force fields could use different combination rules for the van der Waals parameters[69, 70, 71, 72, 73].

The specific force field used in all our MD simulations is the GROMOS96 53a6 force field[71, 72, 73]. It uses an united-atom representation (Figure 1.4), which means a non-polar hydrogen bonded to a carbon atom is absorbed into the carbon atom to form a hydrocarbon. Compared to all-atom force fields, such as Amber, the united-atom representation in the GROMOS96 53a6 requires significantly less computational cost, especially

for lipids, for which the number of atoms can get reduced by two thirds(Figure 1.4). The GROMOS force field was originally optimized with respect to the condensed phase properties of alkanes[71, 72, 73]. It has been widely used for lipid and protein simulations. For specific lipid types, the original GROMOS force field parameters can be adjusted to obtain better parametrization, e.g., for the 1,2-dimyristoyl-*sn*-glycero-3-phosphocholine (DMPC) lipid, modification to partial charges and adjustment to the van der Waals radius for the carbonyl-ester atom can reproduce satisfactory area per lipid, the lateral self-diffusion constant and deuterium order parameters of the acyl chains. The chain order parameter is a characterizing measurement of lipid chain's ordering with insight into the phase behavior of the bilayer system[74, 75]. Ordering of nonpolar hydrocarbon chains in lipid bilayer systems can be faithfully represented by the deuterium order parameter S_{CD} measured through ^{2}H NMR experiments. If θ is the angle between a CD bond and the bilayer normal, the order parameter is defined as

$$S_{CD} = \frac{3}{2}\langle \cos^2 \theta \rangle - \frac{1}{2}, \tag{1.16}$$

separately for each hydrocarbon. The brackets stand for averaging over time and/or molecules. For water, the simple point-charge model (SPC)[76, 77] has been used in all our MD simulations to be consistent with the GROMOS force field we employed.

1.2.5 Periodic Boundary Conditions

The importance of periodic boundary conditions (PBC) arises from the dilemma that MD simulations can only simulate a very limited size system, compared to the macroscopic systems in physical reality with virtually an infinite number of particles. Considering the size of the system, or the number of atoms in current state-of-art MD simulations (tens of million atoms simulated[37]), the number of atoms would be negligible, compared to the number of atoms in a macroscopic system, except for the simulation of microscopic clusters. Luckily in macroscopic systems, only a small fraction of the atoms are located in the vicinity of the boundaries. This enables us to use PBC to tackle the finite size issue. PBC means that atoms are enclosed in a simulation box, which is replicated to all the three Cartesian directions by translation with the entire Euclidean space filled. One "original atom" in the simulation box would have an infinite number of "image" atoms which would move completely in synchronization with the "original" one (Figure 1.5a). When an atom enters or leaves the simulation box, an image atom would leave or enter the box on the opposite side. Therefore the number of atoms in the simulation box is always a constant, which was determined during the simulation box setup. PBC allows MD simulations to

partially address the finite size issue by "pretending" to simulate an infinite one, at the risk of possible artifacts (Figure 1.5b). The possible artifacts include imposed symmetry by using a specific PBC type, such as cubic PBC[78]. Chapter 4 is dedicated to the discussion of monolayer curvatures where small and relatively large simulation boxes give vastly different results.

Besides the most simple PBC type, i.e., rectangular space-filling unit cell, other PBC types, such as rhombic dodecahedron and the truncated octahedron[79] have proven their value for simulating approximately spherical structures in solution, as they are closer to being a sphere and thus require fewer solvent molecules to fill the box given a minimum distance between the spherical structure's images.

1.2.6 The Statistical Mechanics Behind The Molecular Dynamics Methods

Thermodynamics summarizes the experimentally measured relations between various macroscopic observables such as temperature, volume, pressure of a system. On the other hand, statistical mechanics starts with postulates about the properties and interactions of the microscopic constituent particles to derive the physical behavior of the macroscopic systems. The direct output of an atomistic MD simulation is usually atomic and molecular coordinates and velocities which are microscopic information. Then statistical mechanics has to be employed to derive the macroscopic properties of the simulated system from the microscopic information generated by the MD simulation. In this section, a brief review of the most relevant notions in thermodynamics and statistical mechanics for MD simulations is given. More in-depth discussion of statistical mechanics can be found in literatures[80, 81].

The pivotal notion in thermodynamics is thermodynamic equilibrium. A system is in thermodynamic equilibrium if it is in thermal, mechanical and chemical equilibrium with the environment. Thermal equilibrium means that there is no net heat inflow or outflow between the system and the environment. The condition for reaching thermal equilibrium is that the temperatures of the system and the environment are the same. Mechanical equilibrium means that the net forces $\sum_i \vec{F}_i$ and torques $\sum_i \vec{\tau}_i$ must be zero. Chemical equilibrium means that the chemical potentials of all substances μ_i in the system and the environment are constant in time and uniform in space.

MD methods can be employed to study the properties of a simulated system in the equilibrium state or in a dynamic process. If the purpose of a MD simulation is to investigate the equilibrium properties, an equilibration stage of MD run is usually needed for the

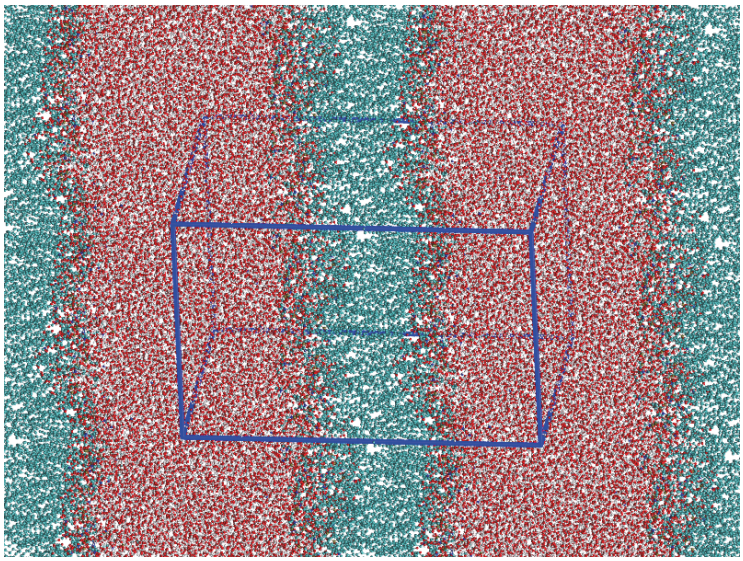

(a)

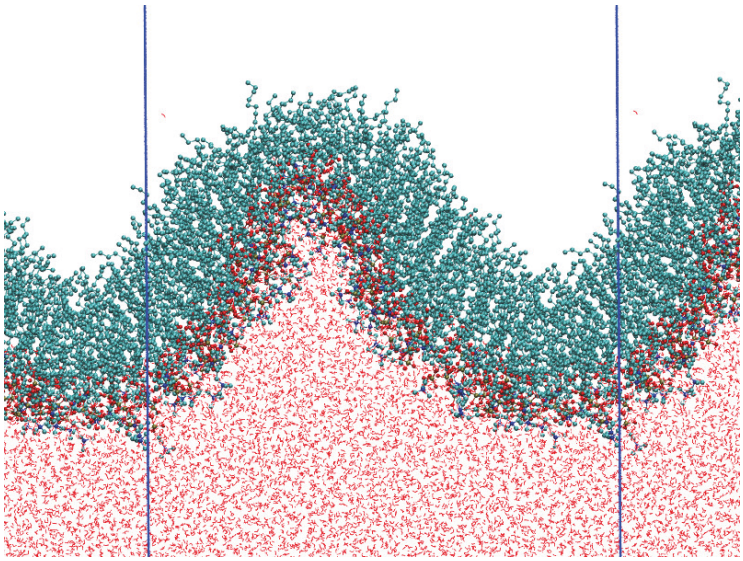

(b)

Figure 1.5: Illustrations of periodic boundary conditions and the associated artifacts. (a) A lipid bilayer system with lipids shown as cyan, and water as red and white lines. The unit box boundaries are depicted by thick blue lines. (b) A highly buckled lipid monolayer in which the periodicity of the buckling highly modulated by the size of the simulation box, which is an artifact.

system to achieve equilibrium. Reaching equilibrium requires all the macroscopic observables in a MD simulation, including energies, virials, temperature, pressure tensors and macroscopic geometries, etc., to converge to an equilibrium range, i.e., showing only small fluctuations but no systematic drift. For lipid systems we simulated, other macroscopic observables, such as area per lipid or hydrogen bonding numbers, are available to judge if the system has reached equilibrium.

A fundamental notion in statistical mechanics is ensemble. An ensemble can be defined as a collection of a number of macroscopically identical but essentially independent systems[82]. Here the term macroscopically identical means, each of the system constituting an ensemble satisfies the same macroscopic conditions, such as volume, energy, pressure, temperature, and total number of particles etc. The term essentially independent means the systems (in the ensemble) differ only in microscopic conditions, such as the coordinates of the particles constituting the system. Consider a classical system of N particles subjected to certain macroscopic conditions. The positions and momenta for the N particles are denoted, respectively, as $q_1, q_2, ..., q_{3N}$ and $p_1, p_2, ..., p_{3N}$, which evolve in time within a $6N$ dimensional phase space. A microstate is a point in the phase space corresponding to a specific set of q_i, p_i. An ensemble is a collection of all possible microstates for the system subjected to certain macroscopic conditions which are called macrostate[80, 81]. The most simple and easily implemented ensemble in MD simulations is the NVE ensemble, a.k.a., the microcanonical ensemble, for which the macrostate is constant number of particles N, constant volume V and constant energy E. This ensemble describes a system isolated from the environment. The fundamental postulate of statistical mechanics dictates that for an isolated system with an exactly known energy and exactly known composition, the system can be found with equal probability in any microstate consistent with that knowledge[80, 81]. The distribution function of microstates is

$$\rho(q,p) = \frac{1}{\Omega}\delta(H(q,p) - E), \tag{1.17}$$

where δ is the Dirac delta function, $\rho(q,p)$ is the probability for the system to be in the microstate q, p, Ω is the partition function which is the total number of possible microstates in the ensemble, and H is the Hamiltonian.

However this ensemble is seldom realizable in experimental conditions. To obtain direct comparison with experimental data, more realistic ensembles such as the NVT ensemble, a.k.a., the canonical ensemble, for which the macrostate is constant number of atoms N, constant volume V and constant temperature T, and the NPT ensemble, a.k.a., the isothermal-isobaric ensemble, for which the macrostate is constant number of atoms N, constant pressure P and constant temperature T, are required for practical MD simulations[29, 30].

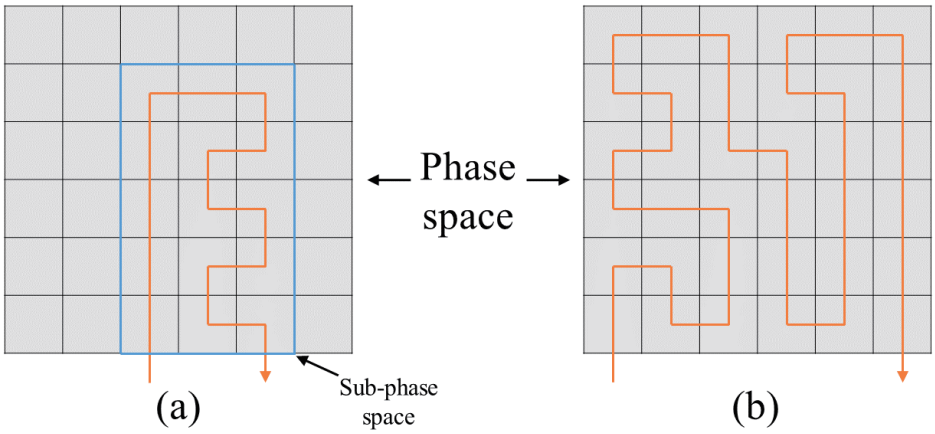

Figure 1.6: (a) A non-ergodic trajectory which only traverses a subset of phase space. (b) An ergodic trajectory which traverses all possible microstates in phase space.

The NVT ensemble describes a closed system in contact with a heat bath at a constant temperature T[80, 81]. The distribution function is

$$\rho(q,p) = \frac{1}{Z} exp[-(H(q,p)/kT], \tag{1.18}$$

where Z is the canonical partition function, and k is the Boltzmann constant[80, 81].

For a macroscopic observable X, the expectation value is governed by all microstates and their distribution in the ensemble[80, 81]. For a canonical ensemble, the expectation value $< X >$ can be calculated as

$$\langle X \rangle = \langle X \rangle_{ens} = \frac{\int X e^{-H(q,p)/kT} d\tau}{\int e^{-H(q,p)/kT} d\tau} \tag{1.19}$$

where $< X >_{ens}$ is called the ensemble average and $d\tau$ is the volume element of the phase space[80, 81].

The fundamental statistical mechanics notion behind the whole MD methods framework is the ergodicity hypothesis which states over long periods of time, the time spent by a system in some region of the phase space of microstates with the same energy is proportional to the volume of this region, i.e., that all accessible microstates are equiprobable over a

long period of time[29, 30]. In more plain words, the ergodic hypothesis draws an equality between ensemble averages and quantities from time average. Because of the equality between ensemble averages and quantities from time average, one can derive the ensemble averages from averaging the MD simulation trajectory, which represents the evolution of the system with time[29, 30].

$$X = X_{ens} = \lim_{M\to\infty} \frac{1}{M} \sum_{i=1}^{M} X_i = \lim_{\tau\to\infty} \frac{1}{\tau} \int_0^{\tau} X(t)dt \approx \frac{1}{n_{steps}} \sum_{n=1}^{n_{steps}} X(C(n)) \tag{1.20}$$

where i represents a possible microstate that a system might be in, and M stands for the number of all possible microstates for the system in a given ensemble, $X(t)$ is the value of X evaluated in a trajectory at time t. The rightmost approximate equality will be discussed later.

One important implication that can be drawn from the ergodicity hypothesis is given a long enough trajectory of a MD simulation, the measured average of a macroscopic observable X, does not depend on the initial configurations or conditions of the simulated system[29, 30]. In MD simulations, a system experiences an evolution in time determined by the Hamilton's equations:

$$\frac{dq_i}{dt} = \frac{\partial H(q,p)}{\partial p_i} \tag{1.21}$$

$$\frac{dp_i}{dt} = -\frac{\partial H(q,p)}{\partial q_i} \tag{1.22}$$

where $H(q,p)$ is the Hamiltonian of the system. Consider a MD trajectory in phase space denoted by $C(t)$. The instantaneous value of a macroscopic observable X evolves with the trajectory as $X(C(t))$. If the simulated trajectory is not long enough, only a subset of the phase space, i.e., a portion of the ensemble, can be traversed by the trajectory (Figure 1.6(a)). Then the average $X(C(t))$ will depend on the initial configurations or conditions which are usually artificial, and the length of the trajectory. Thus it is a biased measurement of the macroscopic observable X. If the simulated trajectory is long enough, the entire phase space, i.e., the whole ensemble, will be traversed by the trajectory (Figure 1.6(b)). Then the average $X(C(t))$ is the true expectation value of X, and it does not depend on the initial configurations or conditions[29, 30].

In the real world MD simulations, the phase space, which usually contains infinite number of possible microstates, can never by fully traversed[62]. However, a MD simulation with a long enough trajectory can be approximately regarded as having visited all the relevant states in the phase space. As the trajectory in a MD simulation is discretized, the measurement of X is made for a certain number of time steps n_{steps}. This is where the rightmost approximate equality in Eq.1.20 originates[29, 30].

1.2.7 Thermostat and Barostat

To achieve desirable ensembles such as the NVT ensemble or the NPT ensemble, algorithms are needed to properly maintain the temperature and/or pressure at the desired value. There are also practical technical reasons to avoid using the NVE ensemble in MD simulations. The MD methods are not exact due to numerical approximations such as various cutoffs for different interactions as well as round-off errors. This leads to unavoidable energy drifts especially when electrostatic interactions are involved, which breaks the definition of the NVE ensemble[83]. Essentially the NVE ensemble is not realizable for the vast majority of simulational cases.

For temperature coupling (thermostat), there are a number of algorithms that work well in different situations. The most basic idea for implementing a thermostat is coupling the simulated system and an "imaginary" heat bath. Since the temperature is essentially determined by the average kinetic energy, maintaining the system's temperature can be achieved by scaling the velocities of the atoms. The excess or shortage of kinetic energy required to maintain the desirable temperature will be transferred to/from the external heat bath,

$$\bar{K} = \frac{1}{2} N_f k T \tag{1.23}$$

where $\bar{K}$ is the average kinetic energy, N_f is the number of degrees of freedom, k is the Boltzmann constant, and T is temperature. The rescaling factor α for the velocities is obtained as

$$\alpha = \sqrt{\frac{\bar{K}}{K}} \tag{1.24}$$

However, directly applying such an algorithm will not generate a strict NVT ensemble. The essential issue of the simple velocity scaling is it can not capture the energy fluctuations correctly. And the calculations of some macroscopic observables, such as heat capacity, depend on correct energy fluctuations[29, 30]. Imagine the velocity scaling is applied for every MD step. Then the kinetic energy will remain a constant during the whole trajectory, which contradicts the calculation of the fluctuation of the kinetic energy by statistical mechanics on NVT ensemble[29, 30]:

$$\sigma_k^2 = \frac{1}{2} N_f k^2 T^2 \tag{1.25}$$

That is why the thermostat we used for all our MD simulations, i.e., the V-rescale algorithm

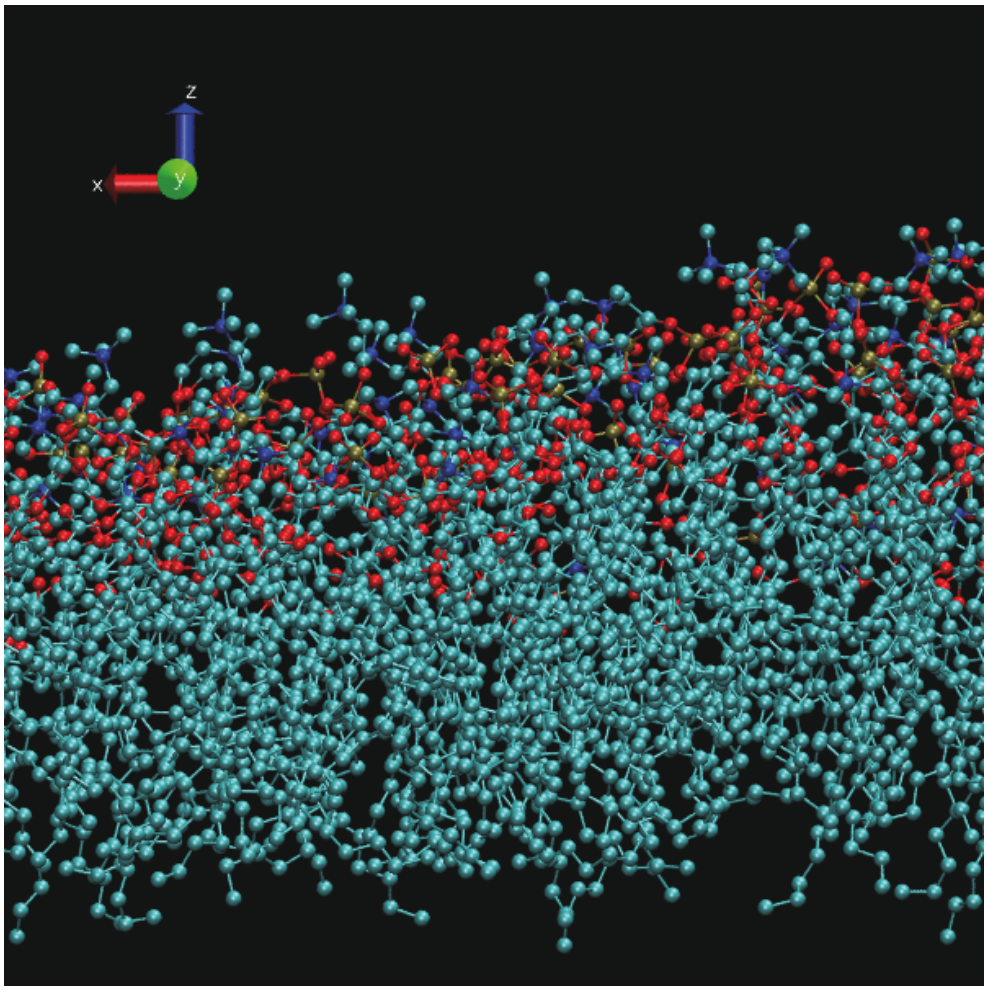

Figure 1.7: A monolayer system with semi-isotropic symmetry. The monolayer has translational and rotational symmetry in the xy plane.

introduces a stochastic term to generate a strict NVT ensemble[84].

$$\alpha = \quad \overline{\frac{K_t}{K}} \tag{1.26}$$

where K_t is drawn from the NVT equilibrium distribution for the kinetic energy:

$$\bar{P}(K_t)dK_t \propto K_t^{N_f/2-1} e^{-\beta K_t} dK_t \tag{1.27}$$

A common issue for various thermostat is in a heterogeneous system, such as a lipid bilayer in water, different components could have different temperatures, e.g., "hot" lipids and "cool" water, though the overall temperature is correctly sampled from the NVT ensemble[85]. This issue is usually addressed by coupling different components to the corresponding heat baths, instead of using a single heat bath. One should not assign too few atoms into a temperature coupling group, e.g., assigning the ions to a separate temperature coupling group, which would introduce artifacts into the simulation.

For pressure coupling (barostat), the nature of the system symmetry could be considered. Lipid bilayer or monolayer systems usually possess semi-isotropic symmetry, i.e., translational and rotational symmetry in the xy plane (Figure 1.7). To accommodate such symmetry, semi-isotropic pressure coupling should also be enabled. Two of the most commonly used barostats are the Berendsen weak-coupling algorithm[83] and Parrinello-Rahman algorithm[86, 87]. Both algorithms were extensively used in our MD simulations. The NPT stage in our MD simulations usually starts with the Berendsen algorithm to allow first-order fast decay of pressure towards the equilibrium (Eq. 1.28)and the use of Berendsen algorithm is beneficial for removing the steric force caused by the artificially constructed simulation box.

$$\frac{dP(t)}{dt} = \frac{1}{\tau_P}(P_{bath} - P(t)) \tag{1.28}$$

Similar to the implementation of the thermostat described above, the Berendsen barostat achieves the convergence towards the desirable pressure by scaling the coordinates for all the atoms

$$r_i' = \lambda^{1/3} r_i \tag{1.29}$$

where the scaling factor λ is evaluated by

$$\lambda = 1 - \kappa \frac{dt}{\tau_P}(P - P_{bath}) \tag{1.30}$$

Here κ is the compressibility defined in classical thermodynamics, $\kappa = -\frac{1}{V}(\frac{\partial V}{\partial P})_T$. Here the coupling constant τ_P appears several times, which is often a parameter that needs to be chosen as the input to the MD simulation. τ_P characterizes the rate at which the deviation $P_{bath} - P(t)$ exponentially decays. For all our MD simulations, a τ_P of 1.0 ps and a compressibility of $4.5 \cdot 10^{-5}$ bar^{-1} are always used.

The main issue for the Berendsen barostat is it does not generate the true NPT ensemble, or more specifically, the fluctuations in pressure or volume which could be essential for calculating thermodynamic properties, are not correct. The Parrinello-Rahman algorithm gives the true NPT ensemble. It allows for the simulation box to change shape as well as size. It may not be suitable for systems that are far from equilibration, as its second-order decay nature requires much longer equilibration time, and sometimes it might even fail. In almost all our MD simulations, the first NPT stage which employs the Berendsen thermostat for equilibration is followed by the second stage using the Parrinello-Rahman algorithm for the statistical averages.

1.3 Lipid Monolayers and Bilayers and Their Molecular Dynamics Simulations

1.3.1 Lipid Molecules

There are a number of definitions for lipid molecules. Each of them captures a key aspect of the broad category of lipids. One definition is a substance that is insoluble in water but soluble in alcohol, ether, and chloroform, which is from the pure experimental chemists' perspective. Another definition is hydrophobic or amphiphilic small molecules with a major part consisting of hydrocarbons as its building blocks. Some people give the definition of lipids by enumerating the subcategories: fatty acids, glycerolipids, glycerophospholipids, sphingolipids, sterol and prenol lipids, etc[88]. The lipid molecules used in the MD simulations presented in this thesis are illustrated in Figure 1.8. The common feature of them is they are comprised of a hydrophilic headgroup and one or two hydrophobic chains. The DPPC, DMPC, and DMPG lipids are glycerophospholipids as they have a glycerol backbone which is connected to the headgroup (phosphatidylcholine for DPPC and DMPC and phosphatidylglycerol for DMPG) and two hydrocarbon chains (*sn-1* and *sn-2*)[88]. The hydrocarbon chains of DPPC each have 16 hydrocarbons while the hydrocarbon chains of DMPC and DMPG each have 14 hydrocarbons. The DPPC, DMPC, and DMPG lipids are all saturated lipids, meaning all the C-C bonds in their hydrocarbon chains are single

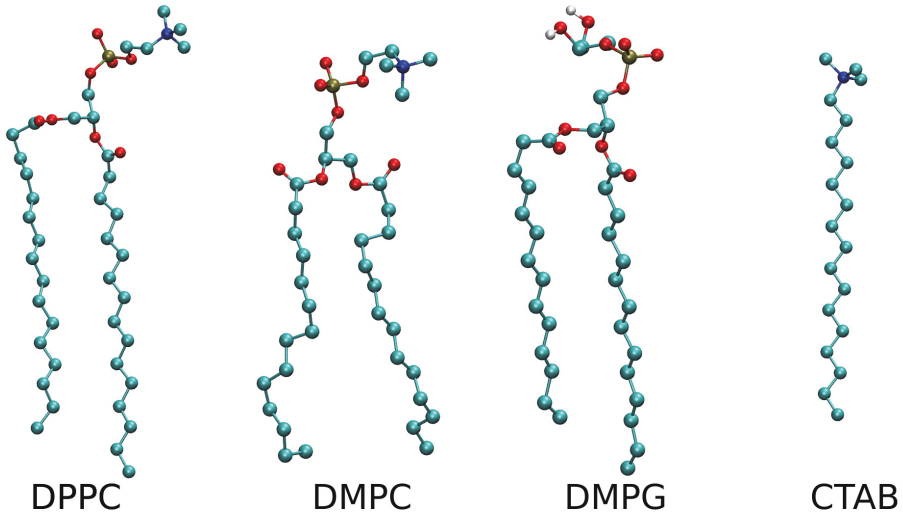

Figure 1.8: The lipid molecules simulated in this thesis in the united-atom representation. Dipalmitoylphosphatidylcholine (DPPC), 1,2-dimyristoyl-*sn*-glycero-3-phosphocholine (DMPC), 1,2-Dimyristoyl-*sn*-glycero-3-phosphorylglycerol (DMPG) belong to a family of lipids called glycerophospholipids, which is characterized by the glycerol backbone connected to a headgroup and two hydrocarbon chains. DPPC and DMPC differ only in the number of hydrocarbons in the hydrocarbon chains. DMPG differs from DPPC and DMPC by having a different headgroup, i.e., PG (phosphatidylglycerol) versus PC (phosphatidylcholine)[88]. CTAB, on the other hand, is a simple molecule with a choline headgroup and a hydrocarbon chain[89].

bonds[88]. There are glycerophospholipids which contains double bonds in their hydrocarbon chains, such as 2-oleoyl-1-pamlitoyl-sn-glyecro-3-glycerol (POPG)[90]. But they were not used in our MD simulations. The CTAB molecule is a simple molecule composed of a choline headgroup and a 16 hydrocarbons long aliphatic chain[89].

The charge state of a lipid molecule is usually determined by its headgroup as the hydrocarbons in aliphatic chains are neutrally charged. The four lipid types used in our MD simulations cover a wide spectrum of charge states. CTAB is a cationic lipid (positively charged) at the physiological condition (pH = 7) determined by the choline group. DPPC and DMPC are zwitterionic lipids (containing both the positively charged choline group and the negatively charged phosphate group). DMPG is an anionic lipid due to the negatively charged phosphate group[91].

In lipid monolayers and bilayers which are not too buckled, the area occupied by a lipid molecule is largely determined by the type of the headgroup and how the headgroup orients as the cross section of the headgroup is much larger than the hydrocarbon chains[88]. On the other hand, the thickness of the monolayer or bilayer is mainly determined by the length of the hydrocarbon chain[88].

1.3.2 Amphiphilic Lipids as Surfactants and Lipid Monolayers

A central property in surface physics and surface chemistry is surface tension. From the perspective of an observable phenomenon, surface tension is the elastic tendency of a fluid surface to acquire the least surface area possible. Figure 1.9a gives an intuitive illustration of how surface tension arises. In a fluid comprising of atoms or molecules of the same or similar kind, an atom or molecule in the fluid bulk interacts with the atoms or molecules in its neighborhood or say the first few coordination shells, which is usually energetically favorable for the system. At the interface between the fluid and air, the situation is different. The favorable interactions between fluid atoms or molecules of the same or similar kind (called cohesion in some literature)[92] is usually stronger than the interactions between a fluid atom or molecule and air (called adhesion in some literature)[92]. However, a fluid atom or molecule at the surface has less atoms or molecules of its kind in its neighborhood. This reduces the chance of forming favorable interactions with the net effect of giving rise to high system energy (incurring an energy penalty), compared to the impossible situation of having all the fluid atoms or molecules in the fluid bulk (which is topologically unachievable in 3D Euclidean space, but possible in other "imaginary" differential manifolds). The fluid instead tries to minimize its surface area, giving rise to the phenomenon of surface tension. Surface tension has an unit of mN/m with the value for bare air/water interace as 72 mN/m at room temperature[93].

Lipids are either hydrophobic or amphiphilic depending on the polarity of the headgroup. If the headgroup is nonpolar, the lipid molecule is hydrophobic. Otherwise, it is amphiphilic due to having the hydrophobic chain(s). The four lipid types used in our MD simulations are all amphiphilic, which make them excellent candidates for surfactants. A surfactant is an agent that lies at the interface between the polar phase, which is usually water, and the non-polar phase, which could be air, pentane, hexane, benzene, etc, to reduce the surface tension[94, 95]. As demonstrated in Figure 1.9b, amphiphilic lipids can work as a surfactant as they can form a monolayer at the interface between the polar phase and the non-polar phase to reduce the surface tension by orienting their polar hydrophilic headgroup in the polar phase and their nonpolar hydrophobic chain in the non-polar phase[96]. Therefore both phases are not directly in contact with each other. In other words, both phases are experiencing the part of the surfactant molecules of their similar kinds. As a result, the boundary effect that creates surface tension is no longer significant[96].

Monolayers formed at an air-liquid interface by amphiphilic molecules are called Langmuir monolayers or films, named after Irving Langmuir, the 1932 Nobel Prize Laureate in Chemistry. The most conventional way to characterize a monolayer's physical behavior is by measuring the surface tension-area per lipid isotherms, or equivalently, the surface pressure-area per lipid isotherms. The surface pressure of a monolayer is linked to the surface tension of the monolayer under the same condition by

$$\Pi(A_L, T) = \gamma_0(T) - \gamma(A_L, T), \tag{1.31}$$

where $\gamma_0 \equiv \gamma_0(T)$ is the bare water/air surface tension which is a function of temperature, and Π, the surface pressure of a monolayer and γ, the surface tension of the monolayer, which are functions of the area per lipid A_L and temperature. In experiments, the observable is usually Π, the surface pressure of a monolayer, which can be directly measured by Langmuir-Blodgett trough experiments. In MD simulations, the observable is usually γ, the surface tension of a monolayer which can be calculated from the diagonal components of the pressure tensor in the simulation box[93]:

$$\begin{aligned}\gamma(t) = \frac{1}{2} \int_0^{L_z} \left\{ P_{zz}(z,t) - \frac{P_{xx}(z,t) + P_{yy}(z,t)}{2} \right\} dz \\ = \frac{L_z}{2} \left\{ P_{zz}(z,t) - \frac{P_{xx}(z,t) + P_{yy}(z,t)}{2} \right\}\end{aligned} \tag{1.32}$$

$$\gamma = \langle (P_N - P_L) \cdot L_z \rangle / 2, \tag{1.33}$$

where L_z is the box size in z-direction, $P_N = P_{zz}$ is the normal pressure, $P_L = (P_{xx}+P_{yy})/2$ is the lateral pressure and the brackets denote averaging over time. The pressure tensor in molecular dynamics can be computed from the kinetic energy and the virials[97]. There is a caveat when one converts the simulated surface tension of a monolayer to the corresponding surface pressure. All the currently available water models can only generate the correct bare air/water surface tension for a certain range of temperature. The bare air/water surface tension to be used in Eq. 1.31 is not the experimental value of 72 mN/m at room temperature, but the value generated by the water model of choice to ensure consistency.

The surface pressure-area isotherm can be employed to study monolayers' phase behavior. For each lipid type, there is a characteristic main phase transition temperature T_m at which the phase transition from gel to liquid occurs[93]. The surface pressure-area isotherms are qualitatively different when the temperature is below or above T_m. When the temperature is below T_m, as the area per lipid increases, the monolayer can undergro a series of transitions from the condensed phase (C) to the liquid-condensed phase (LC), to the coexistence of the LC phase and the liquid-expanded phase (LE), to the LE phase, until the gas phase. When the temperature is above T_m, as the area per lipid increases, the monolayer can only undergo the transition from the LE phase to the gas phase, unless the area per lipid is very small[93]. In the MD simulations we performed, lipids were usually in the LE phase which is characterized by the translational disorder of lipids and the conformational disorder of the aliphatic chains. As for the MD simulations of DPPC monolayers, the temperature was set to 323 K, which is above the T_m = 314 K of DPPC [98]. As for the MD simulations of DMPC and DMPG, the temperature was set to 310 K, which is above the T_m = 296.5 K of DMPC [99], and the T_m range of 291 K - 303K of DMPG [100].

Until now, a planar geometry for lipid monolayers was assumed. At extreme conditions, i.e., with very high surface pressure, the surface tension of the monolayer can even be a negative value, which could eventally lead to the destablization of the planar geometry of the lipid monolayer into a 3D geometry. In some literature, it is called monolayer collapse[88, 93, 101, 102, 103]. This phenomenon was clearly observed in our simulations of pure DPPC monolayers under very high surface pressure. The monolayers did not completely lose their 2D structure. Instead severe buckling was developed along a direction in the xy plane. Examples of monolayer buckling will be given in the Chapters 2&3.

1.3.3 Lipid Bilayers

Figure 1.9c demonstrates a simple model lipid bilayer. A lipid bilayer is constituted by two oppositely oriented leaflets, with the hydrophobic chains pointing inwards, effectively

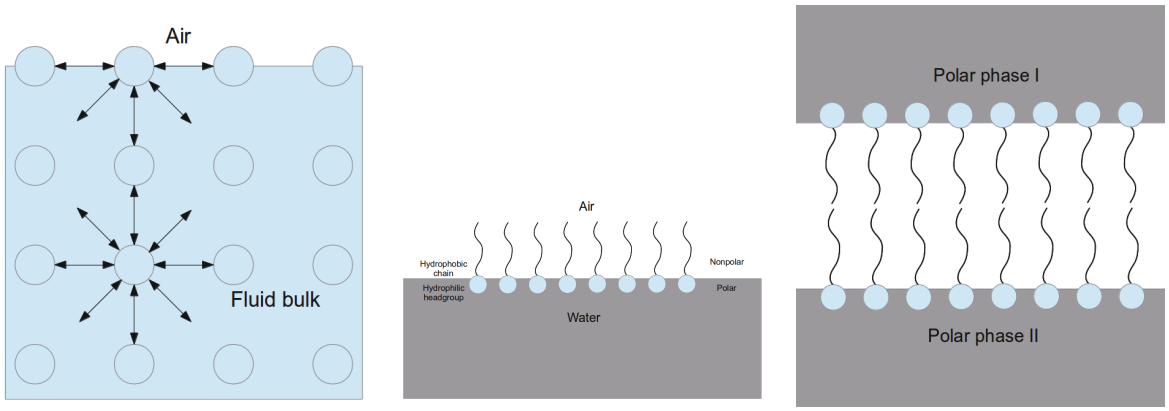

(a) (b) (c)

Figure 1.9: (a) A simple illustrative diagram to explain how surface tension arises. The interactions between an atom in the fluid bulk with the atoms in its coordination shells generally reduce the system energy. However a fluid atom at the surface between the fluid and air has significantly less atoms of its kind in its coordination shells, resulting in lower chance to reduce the system energy. This difference in term of energy can be regarded as the excess energy of placing an atom in the surface, which is defined as surface tension. (b) An illustration of a Langmuir monolayer consisting of amphiphilic lipids. The polar hydrophilic headgroup is facing the polar phase, which is water in this example, and the nonpolar hydrophobic chain is facing the nonpolar phase, which is air in this example. The Langmuir monolayer serves as a surfactant layer helping water reduce the surface tension. (c) An illustration of a model lipid bilayer. The two leaflets of the bilayer assumes a tail to tail orientation, effectively hiding their hydrophobic chains from contacting with the two polar phases to avoid energy penalty. The polar headgroups of the lipid bilayer are almost immersed into the two polar phases. This model can be used as the most simple model for cell membranes, with one of the polar phases stands for the exterior environment, and the other one stands for the cell's inner environment.

hiding the hydrophobic chains from contacting with the two polar phases. The polar headgroups of the lipid bilayer are almost immersed into the two polar phases. Lipid bilayers are vital to almost all living organisms as they are the main component of cell membranes. Lipid bilayers function as the barrier to separate the cell's inner and exterior environment. Water, ions, proteins and other molecules are not allowed to move directly from one side to the other side of a lipid bilayer, despite a lipid bilayer being two layers of lipid molecules in thickness.

The biological membranes consist of many different types of lipids and proteins. The major lipid types in living cells' membranes (bilayers) are phospholipids[92]. DPPC, DMPC and DMPG used in our MD simulations are phospholipids. In MD simulations, it is impractical to include all kinds of lipids and proteins into the simulation. This also poses as a technical difficulty to experiments studying the properties of lipid bilayers. Instead model lipid bilayers constituted by only one or two lipid types are usually used[104, 105]. In the MD simulations to study Daptomycin's antimicrobial activities, mixture bilayers of DMPC and DMPG were used to mimick the bacterial membranes, which were also employed in an experimental study of the antimicrobial activity of amphipathic α-helical peptides[106].

1.3.4 Membrane Elasticity

Elasticity refers to the ability of an object to reverse a deformation when the source of the deformation disappears. The elasticity theory of membranes investigates energy changes that result from four basic classes of membrane deformations, i.e., shearing, stretching, thickness change and bending[107]. As cell membranes are essentially fluid phospholipid bilayers, the shear modulus is not well defined as the lipids resemble a fluid at physiological conditions. Stretching, on the other hand, is an important elastic phenomenon in biological membranes. Hooke's law can be applied here to describe the stretching in the most simplistic way:

$$E_{stretch} = \frac{1}{2} K_{stretch} \frac{(A - A_0)^2}{A_0} \tag{1.34}$$

where A_0 is the area at zero external stress, and the modulus $K_{stretch}$ is the constant between a quadratic deviation of the area from its unstressed state and the respective energy. Characteristic values of $K_{stretch}$ fall in the range 55-70 $k_B T/nm^2$[107]. Biological membranes have a relatively low tensile strength, compared to more elastic materials, i.e., they can only stretch a small amount before rupture occurs[107].

Changing the membrane thickness can be seen as stretching of the membrane in the perpendicular direction. At the lowest order of approximation, again Hooke's law can be

applied to describe the energy cost of thickness deformation:

$$E_{thickness} = \frac{1}{2} K_{thickness} \int dS \left(\frac{w - w_0}{w_0} \right)^2 \tag{1.35}$$

The characteristic value for $K_{thickness}$ is 60 $k_B T/nm^2$[107].

Membrane bending turns out to be the dominant deformation for fluid phase membranes. And much theoretical and experimental work has been dedicated to the study of membrane bending[108, 109, 110, 111]. Membrane bending is a deep topic which could require length of text to describe it in detail. Here a concise description of the most fundamental ideas is given. The description of bending is closely related to the concept of curvature. The curvatures that were commonly used to characterize membranes are the mean and Gaussian curvatures which can be defined on arbitrary points except singularities on a 2D surface in the 3D Euclidean space. For each point p except singularities on a 2D surface S, a normal vector can be defined[112]. There are an infinite number of planes containing the normal vector, each effectively cutting the 2D surface into a plane curve for which a curvature at point p can be defined. Among the infinite number of curvatures which can be defined in this way, the maximal curvature κ_1 and the minimal curvature κ_2 can be found and called the principal curvatures for point p on surface S. The mean curvature is defined as

$$H = \frac{1}{2}(\kappa_1 + \kappa_2) \tag{1.36}$$

And the Gaussian curvature is defined as

$$G = \kappa_1 * \kappa_2 \tag{1.37}$$

The meanings of the mean curvature H and Gaussian curvature G are summarized in Table 1.1. At the lowest order of approximation, the bending energy can be described as

$$E_{bending} = \frac{K_b}{2} \int dS H^2 + \frac{K_G}{2} \int dS G \tag{1.38}$$

where K_b and K_G are the bending moduli associated with the mean and Gaussian curvatures respectively[107].

A more sophiscated model to describe the contribution of bending to the free energy of the membrane is called the Helfrich free energy model[113]:

$$F = \int dS \ \gamma + \frac{1}{2} K_b (H - H_0)^2 + K_G G \tag{1.39}$$

where γ is an area coefficient, also called line tension and H_0 is called the spontaneous curvature.

Table 1.1: The meaning of the mean and Gaussian curvatures[114]

	H	G
≥ 0	Surface S is convex at p	Surface S is equivalent to sphere at p
$= 0$	Surface S is flat on average at p	Surface S is equivalent to cylinder at p
≤ 0	Surface S is concave at p	Surface S is saddle-like at p

1.4 Mechanism for Daptomycin's Antimicrobial Activities

Daptomycin, trade name Cubicin®, is a cyclic lipopeptide with a branch of three amino acid residues and a lipid tail. It was approved by the U.S. Food and Drug Administration (FDA) in 2003 as an antibiotic to treat bacterial infections inflicted by Gram-positive pathogens[115]. Daptomycin gains its significance as Gram-positive pathogens rapidly acquire resistance against other antibiotics, e.g. methicillin-resistant *Staphylococcus aureus*[32]. It consists of a total of 13 amino acid residues, with 10 of which forms a macrolactone which is formed by connecting the C-terminus with the hydroxyl group of Threonine (Thr) via an ester bond (Figure 1.10). Some of the 13 amino acids are non-standard ones, such as kynurenine (Kyn), ornithine (Orn) and methylglutamic acid (mGlu). The lipid tail which is a decanoyl aliphatic chain is acylated with the N-terminus of the peptide chain. At pH=7, daptomycin carries approximately -3 charges caused by the three anionic aspartic acid sidechains, the anionic mGlu sidechain, and the cationic Ornithine (Orn) sidechain[115]. Figure 1.10 shows the block diagram for daptomycin with chirality, and pKa values for the sidechains which could change their protonation states at different pH values.

Daptomycin is a type of antimicrobial peptides (AMPs)[116]. Antimicrobial peptides are a diverse group of molecules, which can be classified into subcategories according to their amino acid composition and structure[116]. AMPs have generally between 12 and 50 amino acids. So daptomycin is a relatively small AMP. Most AMPs are cationic and amphiphilic[117]. The mechanisms by which AMPs kill bacteria are diversified[118] and may differ for different bacterial species[119]. The mechanisms for cationic AMPs' antimicrobial action is relatively straightforward to explain[119]. Compared to the membranes of plants and mammals which usually have no net charges on their outer leaflet[120], bacterial membranes usually have negative charges on their outer leaflet due to considerable concentration of PG lipids and cardiolipin[121, 122]. Therefore, the outer leaflet of the bacterial membrane are more exposed to the attack of cationic AMPs. In other words,

electrostatic interactions play a central role in the binding of cationic AMPs to bacterial membranes[121, 122]. The eventual killing of bacteria by AMPs in most cases can be attributed to the transmembrane pore forming, which fatally depolarizes bacteria[118].

Anionic AMPs, on the other hand, constitute a relatively rare subcategory of AMPs[118]. Besides daptomycin, dermcidin[123] from humans and maximin H5[124] from amphibians are the most studied anionic AMPs. The common feature of anionic AMPs is their high concentration of glutamic and aspartic acids[118, 123, 124], as evidenced in the block diagram of daptomycin Figure 1.10.

Though daptomycin was discovered three decades ago[125, 126, 127], the mechanism for its antimicrobial action remains to be fully understood. A number of experiments confirmed daptomycin's antimicrobial action requires the presence of Ca^{2+} ions in the environment[128, 129, 130, 131, 132, 133, 134] and phosphatidylglycerol (PG) lipids in the membranes[135, 136, 137, 138, 139] which can partially explain the specificity of daptomycin to kill bacteria as PG lipids have a relatively high concentration in bacterial cell membranes but is scarce in human ones.

Various models for daptomycin's antimicrobial action have been proposed. These models can be classified into two distinctive categories. The first category of models are based on daptomycin's inhibition effect on the biosynthesis of lipoteichoic acid which is a major constituent of the cell wall of Gram-positive bacteria with the presence of Ca^{2+} ions[130, 140]. However this model has been challenged by the *in vitro* experiments of daptomycin's activities against *Staphylococcus aureus* and *Enterococcus faecalis*[133]. The second category of models involve daptomycin's binding to Ca^{2+} which could possibly bring a conformational change of daptomycin, following by daptomycin's insertion into the membrane bilayer which leads to membrane depolarization and cell death[36, 131, 132, 141, 142, 143]. However the models within the second category have important difference in term of the detailed mechanisms for action, e.g., where and how the oligomerization of daptomycin occurs. Jung et al.[141, 144] proposed a two-step mechanism of action. First in the presence of Ca^{2+}, daptomycin binds to PG lipids with a minor conformational change. This step increases the chance of oligomerization and micelle formation. In the second step, daptomycin interacts with PG lipids experiencing a major conformational change to make daptomycin insert into bilayer membranes, again in the presence of Ca^{2+}. Straus et al. revised the model proposed by Jung et al. in which during the first step, daptomycin aggregates in solution in the presence of a minimum of 1:1 Ca^{2+} to daptomycin stoichiometric ratio[142]. However the aggregate of daptomycin needs to dissociate later to allow daptomycin interacting with bacterial membranes. They also proposed daptomycin applies positive curvature strain on the lipids and daptomycin may also oligomerize in the membrane. Recently Zhang et al. proposed an even detailed mechanism for daptomycin's antimicrobial activities regarding

the order of binding of daptomycin to the lipid membranes and oligomerization and how oligomerization occurs[36, 143]. The proposed mechanism are illustrated in Figure1.11 with the upper subfigure corresponding to the step 1 in Fig. 7 of Ref.[143], and the lower subfigure corresponding to the steps 2 and 3 in Fig. 7 of Ref.[143]. In their models, daptomycin's spontaneous binding to the bacterial membrane (steps 1 and 2 in Figure1.11) precedes oligomerization in the membrane, which is in turn followed by insertion of daptomycin multimers into membrane. The first intermediate product of the oligomerization of daptomycin in the bacteria membrane is a daptomycin tetramer sitting in the outer leaflet of the membrane bilayer (step 3 in Figure1.11). Then a flip of the tetramer translocates itself from the outer leaflet into the inner leaflet, which is followed by aligning with another daptomycin tetramer sitting in the outer leaflet to form a daptomycin octamer to serve as a functional pore to depolarize the bacterial membrane (step 4 in Figure1.11). They derived their model from their FRET experiment results with an estimation of the number of daptomycin monomers in a daptomycin multimer in the bacterial membrane[36, 143].

Though with such a multitude of experimental work on daptomycin's antimicrobial action, whether and how daptomycin binds to the bacterial membrane bilayer and whether and how daptomycin aggregates inside the membrane remains an unanswered question. Experimental measures such as NMR and FRET are often limited by the experimental conditions and temporal and spatial resolutions, regarding solving the problem of daptomycin's antimicrobial action. Molecular dynamics simulations which can provide atomistic level details of daptomycin's interactions with model phospholipid bilayers, pose as valuable tools to complement the experimental measures to give a more complete and thorough picture of daptomycin's antimicrobial action. To our best knowledge, the only existing MD simulation works on daptomycin besides ours was by Scott et al.[145] who applied time-averaged distance restraining potential to the structural change of daptomycin upon binding to DHPC micelles with and without the presence of Ca^{2+} and by Ho et al.[146] to unravel the problem of how daptomycin binds to Ca^{2+} in solution and the possible binding sites and conformational change involved in this process. However the interactions between daptomycin and a model lipid bilayer which mimicks the bacterial cell membrane in the presence of Ca^{2+} is yet an interesting and possibly fruitful field to be exploited by MD simulations.

In Chapter 5, we aim to explore a key stage of daptomycin antimicrobial action by using state-of-art MD simulation techniques, i.e., a single daptomycin molecule's spontaneous binding to a model phospholipid bilayer mimicking the bacterial membrane consisting of equal molar ratio of 1,2-dimyristoyl-*sn*-glycero-3-phosphocholine (DMPC) and 1,2-Dimyristoyl-*sn*-glycero-3-phosphorylglycerol (DMPG). The mixture bilayer of DMPC and DMPG has been widely used as the model "bacterial" membrane by a number of exper-

imental studies[36, 143, 147, 148, 149] with an application to study antimicrobial peptide's interactions with the model "bacterial" membrane[147] and a few MD studies[91]. We employed various analysis techniques to give an insight into the behaviors of daptomycin and its interactions with the other components of the simulated systems, especially the DMPC/DMPG lipids and Ca^{2+} ions at the atomistic level. More specifically, we evaluated the potential of mean force (PMF) for the spontaneous binding process with a comparison to the PMF for the binding to a pure DMPC bilayer, the center of mass (COM) motion of the daptomycin molecule and its residues relative to the DMPC/DMPG bilayer midplane, the radial distribution functions (RDFs) between Ca^{2+} and daptomycin, daptomycin's effect on lipid orientation, hydrogen bonding, and the last but not least, we used principal component analysis (PCA) techniques to investigate the change of main-chain conformation upon daptomycin's spontaneous binding to the model DMPC/DMPG bilayer.

We are aware that there are other important stages of the proposed model of action for daptomycin, including but not limited to the insertion of daptomycin into the membrane bilayer, the process of oligomerization of daptomycin into multimers in the lipid membrane bilayer, the possible translocation of the daptomycin tetramer into the inner (lower) leaflet of the membrane bilayer, and the possible assembly of a daptomycin octomer to form a pore on the membrane. We did not attempt to simulate these stages because they are essentially intractable by contemporary MD simulations due to the time scale issue, i.e., they occur at several magnitude longer time scale (milliseconds to minutes)[130, 150] than what we are capable of simulating which is in this paper, the order of 1-10 µs.

1.5 Structure of This Thesis

Chapter 2 is dedicated to details of parametrizing lipid molecules, simulation box setup and techniques of running monolayer simulations, which complements the background introduction on drug delivery, lipid structure and systems and the molecular dynamics method in the previous sections of this chapter.

We employed atomistic molecular dynamics simulations to study lipid Langmuir monolayers composed of both pure DPPC and a mixture of DPPC and CTAB aiming to reveal how the composition of the DPPC/CTAB monolayers affects their structural and electrostatic properties, which will be fully discussed in Chapter 3.

In Chapter 4, we analyzed the same simulation trajectories which have been used in the analysis presented in Chapter 3. This chapter is dedicated to the discussion of DPPC/CTAB monolayers' mean and Gaussian curvatures and the artifact introduced by

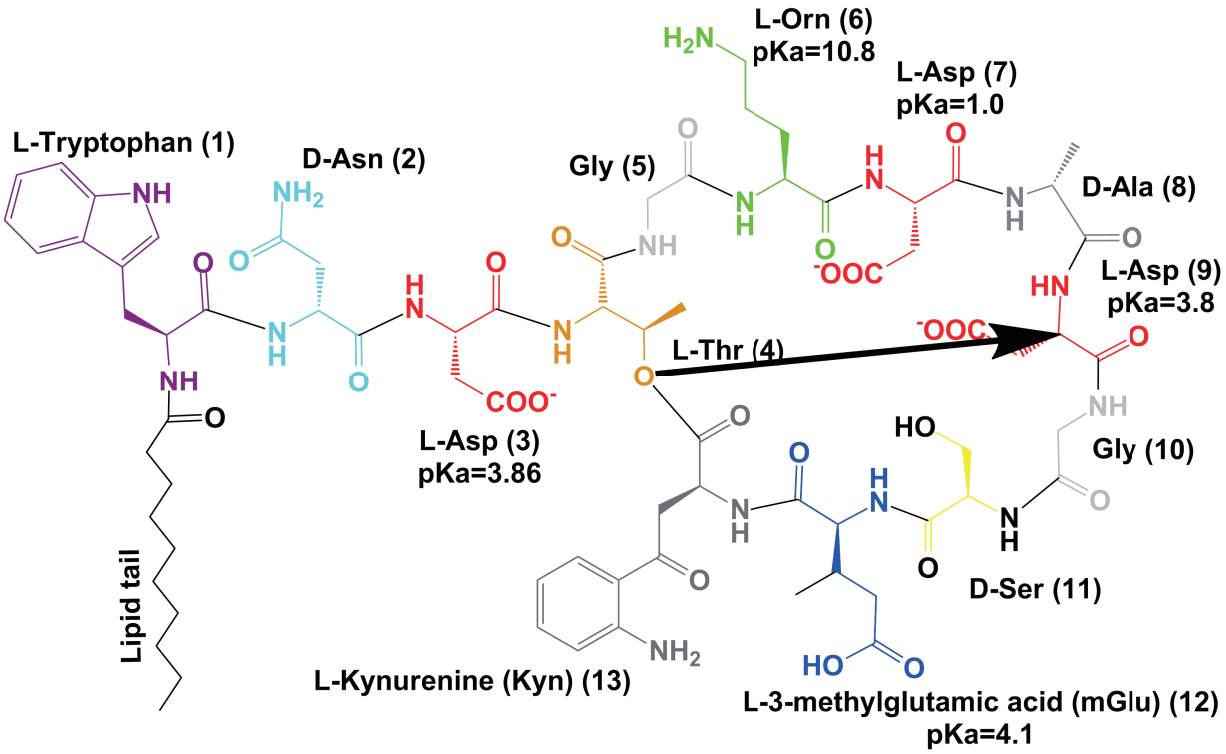

Figure 1.10: Color block diagram of daptomycin. The numbering of the residues is shown in the parenthesis following the residue names. Side chains which can change their protonation states under various pH environment are shown with their pKa values. The literature pKa values for Asp3 ranging from 3.86-4.3[151, 152], Asp7 as 1.0[152], Asp9 as 3.8[152], Orn ranging from 10.7-10.8[153, 154], mGlu ranging from 4.1-4.6[152, 155]. Only one pKa value, not the range, is labeled for the Asp3, Asp7, Orn and mGlu sidechains as only the protonation states of the sidechains matter in this MD simulation work as the protonation state and thus the charge state must be determined *a priori* before the simulation box setup. At pH = 7, daptomycin carries approximately -3 charges. The arrow shows the vector used to define the molecules ori-entation.

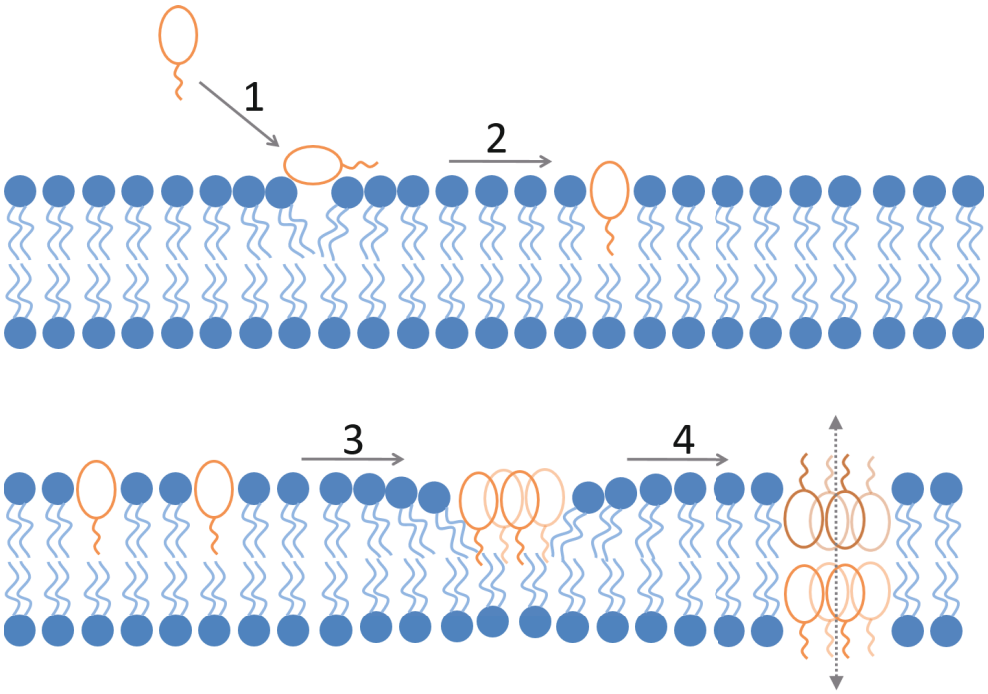

Figure 1.11: Proposed mechanism for daptomycin's antimicrobial activities[36, 143]. (1) Daptomycin's spontaneous binding to the bacterial membrane. characterized by forming hydrogen bonds between daptomycin and the phospholipids in the bacterial membrane. (2) Daptomycin inserts its lipid tail into the bacterial membrane and gets partially embedded. (3) Oligomerization of daptomycin molecules into tetramers in the outer leaflet of the bacterial membrane. (4) A flip of the tetramer translocates itself from the outer leaflet into the inner leaflet, which is followed by aligning with another daptomycin tetramer sitting in the outer leaflet to form a daptomycin octamer to serve as a functional pore to depolarize the bacterial membrane.

using small simulation box, as small and relatively large simulation boxes give vastly different results.

We also conducted atomistic molecular dynamics simulations to study the mechanism of daptomycin's antimicrobial activities, or more specifically, the behavior and structural changes of daptomycin in one of the key stages of the process of killing bacteria, i.e., the spontaneous binding of daptomycin to the model bacteria membrane. The detailed results will be presented in Chapter 5.

Chapter 2

Molecular Dynamics Simulation of Surfactant Monolayers

The contents of this chapter were adapted from the book chapter published in

Bin Liu, Jirasak Wong-Ekkabut, Mikko Karttunen. "Molecular Dynamics Simulation of Surfactant Monolayers", Chapter 11 in Computational Methods for Complex Liquid-Fluid Interfaces (page 249-264), Edited by Mohammad Taeibi Rahni, Mohsen Karbaschi, and Reinhard Miller Copyright (2015) CRC Press

2.1 Introduction

In this review, we provide a brief introduction to molecular simulations of lipid / surfactant monolayers. We do not aim to provide a comprehensive review. Instead, we first discuss the very timely problem of nanoparticle interactions with the lung surfactant and how that can be studied by simulations. After that, we provide a detailed introduction on the various aspects of building a monolayer simulation and show a case study using simulations of cationic surfactants and zwitterionic lipids. The aim is to provide the reader with a detailed view of how to build simulations, what aspects are important and what kind of properties can be analyzed. In our other contributions of this volume we discuss electrostatic interactions in detail. That discussion is also valid here and we refer the reader to that chapter regarding the details of how the important electrostatic interactions must be account for in interfacial systems.

2.2 Parametrizing lipid molecules

The previous section demonstrated the utility of molecular simulations. In this section, we discuss the details how to obtain parameters for lipid or surfactant molecules when they are not readily available from prior research.

Before being able to perform any MD simulations, one must obtain force field parameters, or in the case they do not exist, parametrize the molecules of interest so that the MD program can understand their compositions, structures and interactions with each other and other components in simulation. This is an essential step as it determines the simulation's correctness, quality and value. Although lots of lipid and surfactant molecules have been parameterized, for many lipid molecules, significant manual work, including *ab initio* calculations for partial charges and constructing topology files which describe the modelling or parametrization understandable to a MD program, is still mandatory to obtain a quality parametrization for lipid molecules. Tools for generating topology files automatically from a structure file such as a PDB file exist [156]. But the quality of the generated topology files is usually far from being desirable.

There are two broad categories for the force fields in lipid modelling, the atomistic approach and the coarse-grained (CG) approach. The CG force fields, as used in the lung surfactant study in the previous section, such as the famous MARTINI model [157, 158], are known for their speed and larger system sizes. Atomistic force fields, on the other hand, are often able to provide quantitative predictions that can be verified by experiments, and are versatile. The atomistic force fields can be classified into two flavors, the all-atom ones and the united-atom ones. In an all-atom force field, such as OPLS [69, 159], AMBER [160, 161, 162, 163] and CHARMM [164, 165, 166], all atoms are explicitly present in the simulation. In an united-atom force field, such as the GROMOS force field [71, 167, 168], the nonpolar hydrogens bonded to the carbons in a acyl chain are absorbed into the carbons to which they are bonded, to form a 'united atom' to reduce the number of interacting sites. Here, we focus on some practical issues and skills useful in obtaining good quality parametrization for lipid molecules by using one of the most widely used atomistic force field for lipid simulations, the GROMOS force field and its derivative, the Berger lipid model [169]. It is also worth noting that the OPLS force field has also found many applications in lipid simulations (yet work remains to be done for OPLS peptide parameterization [73]). In addition, there is currently a very interesting open collaboration platform called *Matching lipid force fields with NMR data* available on the Internet at `http://nmrlipids.blogspot.ca`. This approach is pioneered by Markus Miettinen and Samuli Ollila is groundbreaking and may lead to fully new developments and integration of experimental and computational lipid data.

From the practical point of view, a good way to obtain a quality parametrization for a lipid molecule is by studying and reusing mature, well-tested parametrization for other lipid molecules which share notable amounts of parts as the lipid to be parametrized. It may, of course, be the case that no such parametrization exists. This shortcut approach has been applied to many lipid molecules with success. One of the most famous 'baseline' lipid parametrization from which many other parametrizations were derived is the DPPC parametrization [170] based on the GROMOS force field and the Berger lipid model. Many other saturated dichained lipids, including DMPC [171] and DLPC can be easily parametrized by adding or removing repeating hydrocarbons. Borrowing the parametrization for the double bonded hydrocarbons, this DPPC parametrization can be adapted to construct parametrization for unsaturated dichained lipids, such as DOPC, POPC and SOPC in principle. A word of warning should be said, however: Double bonds can be tricky to parametrize and it has been shown that old parametrizations are wrong and can influence the observed physical properties of lipids and their interactions with others [172, 173]. Similarly, the PC headgroup can also be substituted by other parametrized headgroups, such as the PG headgroup to obtain parametrizations for the corresponding PG lipids [174].

If the headgroup of the lipid of interest has not been parametrized, one can use the parameter set of a force field to parametrize it. The parameter set includes equilibrium position and force constant for bonded interactions such as bond stretching, bond angle bending and proper and improper dihedral interactions, van der Waals radii and constants. What is usually missing in a force field for a specific headgroup is the partial charges. Quantum chemistry calculations are needed to obtain the partial charges to parametrize a headgroup. Ideally, one should apply quantum chemistry approaches to calculate the partial charges for the entire lipid. However, as the computational cost of a quantum chemistry calculation scales as the third order or even more of the number of electrons in the system, it becomes quickly intractable as the size of the lipid increases. Fortunately, the "locality" of partial charges and the "insulating" property of hydrocarbons can be employed to reduce the computational cost. The "locality" of partial charges means the partial charge of a specific site (an atom or an united atom) is only influenced heavily by its first and second bonded neighbors. One important exception is aromatic rings. In any cases, an aromatic ring must be treated as a whole. The "insulating" property of hydrocarbons means one hydrocarbon can be essentially regarded as a neutrally-charged dividing point to separate two independent partial charge regions. Therefore, one can perform quantum chemistry calculations for a pseudo molecule composed of a headgroup and a methyl or ethyl group. If the headgroup contains one or more hydrocarbons, one can divide the headgroup again into smaller parts and cap them with methyl or ethyl groups

to form pseudo molecules. Usually the accuracy of partial charges obtained from such a pseudo molecule is within the tolerance of a MD simulation for lipids.

Quantum chemistry calculations for partial charges can be performed by using the well-known Gaussian package [175] and some open source packages such as the GAMESS family which includes GAMESS-US [176, 177] and Firefly [176, 178] as its two major variants. One of the most popular basis set, e.g. 6-31G* and 6-31G(d,p) [179, 180, 181] which offer both decent accuracy and acceptable computational cost, is often used for calculating the partial charges for a lipid. 6-31G* has also been employed to obtain the partial charges in the AMBER force field [182]. These basis sets usually work well for neutral and cationic lipids. But for anionic lipids, 6-31+G* or 6-31+G(d,p) [183, 184] which include diffuse function to account for the presence of significant charge density that are distant from the atomic nuclei, are needed to get accurate results at the cost of slower or even difficult convergence. To take the effect of electron correlation on partial charges into account, post-Hartree-Fock (HF) methods or density functional theory (DFT) methods are usually employed as they are generally superior to the plain Hartree-Fock level calculation in which electron correlation is totally neglected. Moeller-Plesset level 2 (MP2) method which is a post-HF method, is usually preferable as it can take most of electron correlation into account at affordable computational cost. DFT methods can also work well provided one chooses an appropriate exchange-correlation functional (E_{xc}). The quantum chemistry packages mentioned above can offer four sets of partial charges, i.e., those by Mulliken population analysis [185, 186], Löwdin population analysis [187, 188], electrostatic potential analysis (ESP) [189, 190] and natural population analysis (NPA) [191, 192, 193]. NPA can only be done by the natural bond orbital (NBO) module [193] which exists as a plugin for all the major quantum chemistry packages. Once one obtains the four sets of partial charges, one should first use one's chemical instinct to judge which set is most reasonable. Our experience shows that usually the NPA scheme is the choice as it is not sensitive to the choice of basis set, theory level, or initial structure of the molecule being investigated. But the choice of partial charge scheme could differ from case to case. In principle, one should also employ polarized continuum model (PCM) [194, 195, 196, 197] to reflect the influence of the aqueous environment on partial charges. However, our experience shows the use of PCM makes negligible difference for partial charges of the molecules for biological or physiological simulations.

Quantum chemistry calculations for partial charges usually take two steps. First, one uses the plain HF level calculation to perform geometry optimization for the molecule being investigated and obtain the "equilibrium" structure. We put a double quote to encompass the word equilibrium because the geometry optimization usually ends up in a local minimum or even a saddle point on the potential energy surface as the global minimum

is extremely difficult to reach if possible at all. This is caused by the high dimensional and very complex potential energy surface landscape of any molecule of decent size. The point of performing this step is getting a structure reasonably close to the real equilibrium structure for the second quantum chemistry calculation step and in real MD trajectories, molecules are always close to their equilibrium structures but seldom sit there. The second step involves using the optimized structure obtained in the first step to perform single point calculation at either MP2 level or with a DFT method to account for electron correlation. Our experience shows the partial charges obtained by using a MP2 level or DFT calculation are distinguishable from those from the plain HF level calculation, but reasonably close.

One may encounter the difficult situation in which one bonded interaction in the molecule being parametrized has not been parametrized in a specific force field. One obvious approach is to look for experimental results to find the equilibrium position and force constant for it. One can also resort to quantum chemistry calculations to perform a scan of the potential energy surface on the dimension of interest. In the following example (Figure 2.1, the angle bending interaction between CH2-(C=O)-C(benzene) is not parametrized in the GROMOS force field [71]. The first step to parametrize it using the harmonic oscillator approximation is capping CH2 with CH3 (methyl group) to form a pseudo molecule. To facilitate the parametrization, one would better convert the structure representation of this pseudo molecule from Cartesian to internal coordinates (Z-matrix representation) which can be accomplished by using chemical visualization programs such as MacMolPlt [198]. Then one can generate a set of input files for quantum chemistry calculations with single point structures represented by Z-matrix and with varying CH2-(C=O)-C angles which should cover the guessed equilibrium angle. This set of quantum chemistry calculations usually can give a set of system energies which can be almost perfectly fitted to a parabola against the varying CH2-(C=O)-C angles. From the fitting, one can retrieve the equilibrium angle and force constant for this angle bending interaction.

2.3 Simulation box setup

Once parametrization for all molecules has been obtained, the next step for the simulation is to construct a simulation box which consists of all the components needed and has the appropriate geometric configuration. In theory, any box types that can fill up the entire space with periodic boundary condition can be used for monolayer simulations, including some perhaps bizarre sounding box types like rhombic dodecahedron or truncated octahedron. For the easy of analysis and practical reasons, the simplest rectangular box type is almost always used unless there are some special requirements.

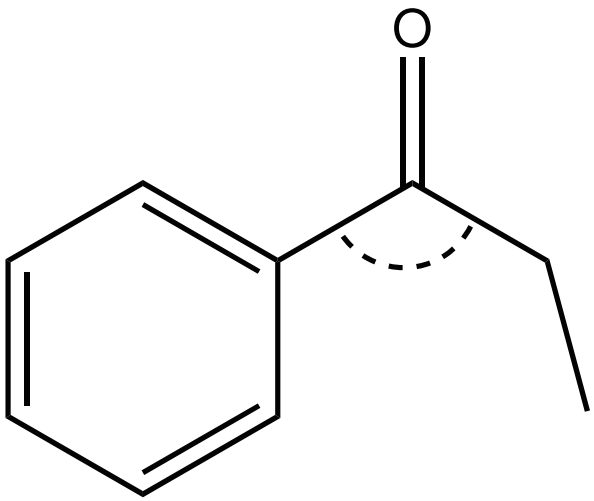

Figure 2.1: Diagram for a pseudo molecule for parametrizing the angle bending interaction between CH2-(C=O)-C(benzene).

For monolayer at air/water interface simulations, there are two popular geometrical configuration setups, see Figure 2.2. In Figure 2.2a, the simulated monolayer is placed at the interface between the water and air phases, and a wall potential is applied to the bottom of the water phase to prevent molecules from escaping. The water slab should be thick enough to allow recovery of bulk water property for the region that has a direct effect on the monolayer[199]. Another very popular configuration is displayed in Figure 2.2b where two symmetrical monolayers are separated by a water slab thick enough to restore bulk water property in the middle and hence prevent interactions between these two monolayers [104]. Caution should be taken when one uses the setup in Figure 2.2a with the NPT ensemble, or in a situation in which severe buckling may develop, as the varying box size or monolayer geometry may interfere with the wall potential and cause artifacts.

One way to check if the water slab in Figure 2.2b is thick enough is to calculate water dipole orientation along the z-axis and calculate the Debye screening length. In the vicinity of the polar headgroups of the monolayers, water dipole orientation is distinctively different from that in bulk water region which should be isotropic. With either configuration, the air phase (essentially vacuum in most simulations) needs to be thick enough to prevent the interactions between the simulated system and its periodic images in z-direction.

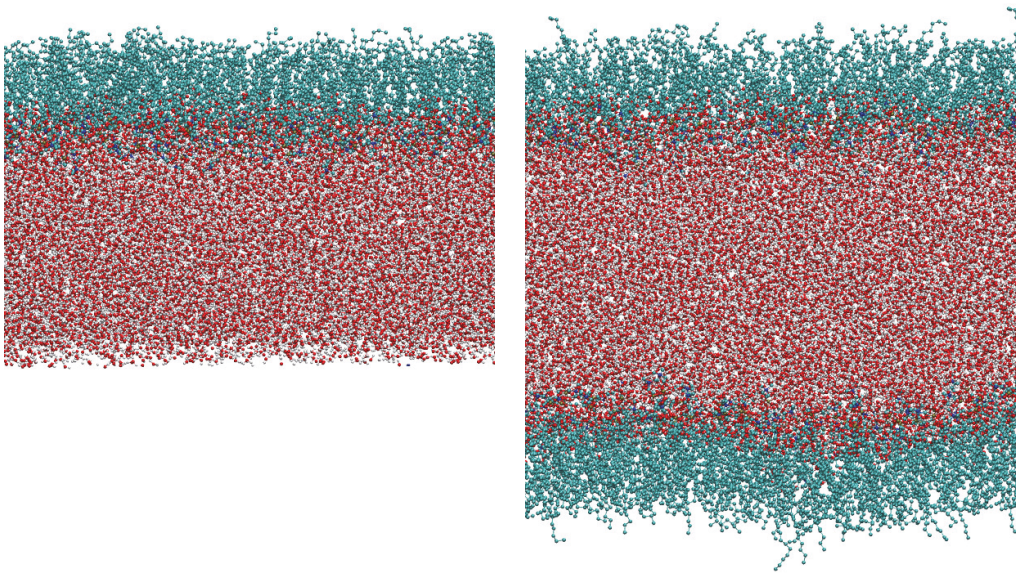

(a) (b)

Figure 2.2: Two types of simulation box setup for monolayers at the air/water interface. (Left) A wall potential is applied to prevent water from escaping. (Right) Symmetrical monolayers separated by a thick water slab. Monolayers displayed here consist of DPPC lipids modeled by the GROMOS force field and the Berger lipid model.

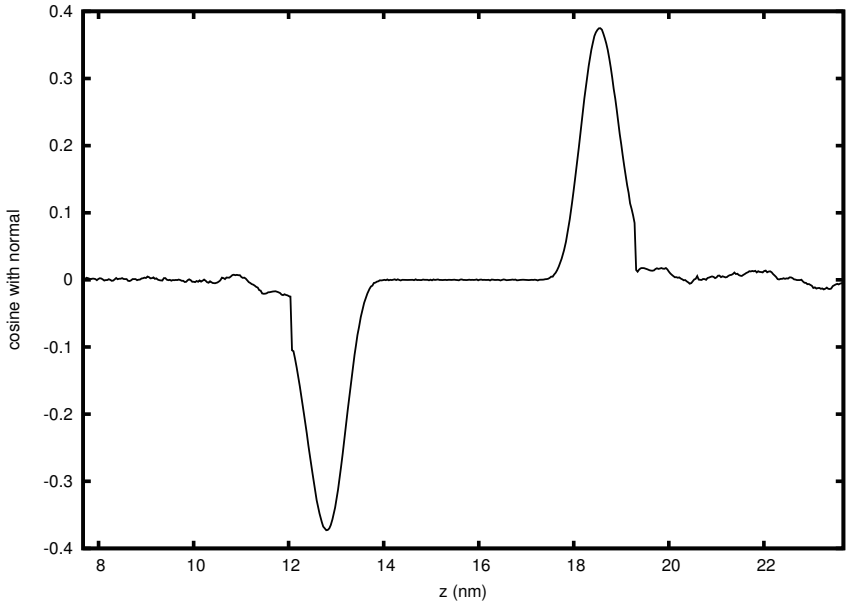

Figure 2.3: Water dipole orientation for the symmetrical configuration in Figure 2.2b. The two symmetrical peaks correspond to the phosphate region in the DPPC headgroup which significantly reorients water dipole. Bulk water property rapidly resumes away from the headgroup region. The ripples in the lipid chain region and in the air phase are caused by small number of water molecules escaped from the water slab.

2.4 Running monolayer simulations

Once the simulation box has been constructed, the production simulations are usually the least complicated step compared to parametrization or analysis (which will be discussed in detail below). Modern MD packages, such as GROMACS [53], NAMD [200], AMBER [201], usually provide reliable default parameter settings and excellent documentation. One must, however, always pay attention to the particular demands of the system and verify that the behavior is physically correct [64]. Typically, one needs to conduct trial simulations to verify the choice of parameters against existing experiments or other simulation results.

Usually monolayer simulations start with the energy minimization step. Steep descent and conjugate gradient (CG) methods are the most popular choices. This step relaxes the energy introduced by the artificial system setup which could otherwise make the following dynamic simulation steps unstable. Failing to complete the minimization step usually indicates serious issues in either parametrization or simulation box setup or both.

Depending on the goals one wants to achieve with a monolayer simulation, the next step could be either a constant temperature (NVT) simulation which comprises of both the equilibration stage and the production stage, or a series of NVT simulations or constant temperature constant pressure (NPT) simulations for equilibration followed by a production NPT simulation. The choice of thermostat and/or barostat determines the quality of NVT or NPT simulations to a large extent. Popular thermostats include Nosé-Hoover [202, 203] or Nosé-Hoover chains [204], Berendsen thermostat or its variants [83], Andersen thermostat [205] and the increasingly popular V-Rescale thermostat [84] which has proven to be suitable for both equilibration and production simulations [63]. Popular barostats include Berendsen coupling [83] which is very useful for situations where the system is far from equilibration as it provides first-order decaying towards equilibrium, and the Parrinello-Rahman coupling [86] which serves the production stage very well and is generally the recommended method.

In the past, treating long-ranged Coulombic interactions were computationally intensive and tricky to handle. The Particle-Mesh Ewald (PME) algorithm [57] is becoming the *de-facto* standard treatment for Coulombic interactions as it offers both satisfactory accuracy and very decent efficiency [56, 60, 65, 206, 207] provided one chooses appropriate cut-off ranges. The choice of real-space range is usually less important when PME is used than with other algorithms that treat Coulombic interactions such as Reaction Field [208], since in PME the real-space cutoff is no more than a division of computational burden into a real-space part and a reciprocal space part. The lower sensitivity to the choice of cut-off range in PME is another advantage. Recent reviews are provided in Refs. [56, 60]. Our other

contribution in this book also contains a detailed discussion of electrostatic interactions when interfaces are present.

2.5 Analysis and a case study for DPPC/CTAB monolayers

In this section, we discuss both the conventional analysis that can be relatively easily done and some advanced analysis techniques which have been recently developed in the context of monolayer simulations. As shown in Figures 2.2b and 2.4, both pure DPPC monolayers and DPPC/CTAB mixtures were simulated by employing the symmetrical configuration setup [104]. Each monolayer in the simulation box consists of 128 lipids. CTAB (cetyltrimethylammonium bromide) is a cationic surfactant [209]. It has a trimethyl ammonium headgroup and a lipid chain of 16 hydrocarbons. A series of NVT simulations with various simulation box sizes at various CTAB molar fractions were conducted.

Snapshots along the trajectory are often an intuitive and important way to gauge how the simulation evolves in time. Figure 2.4 displays snapshots at the end of 1 μs trajectories for three monolayers with various CTAB molar fractions. The visualizations were obtained by using the VMD [210, 211] software, possibly the most popular MD visualization tool. Severe buckling occurs in the pure DPPC monolayer (Figure 2.4a) at a low area per lipid 0.4 nm^2 which indicates high surface pressure. The monolayer with 20% CTAB displays much milder buckling and with 30% CTAB buckling almost disappears. This indicates CTAB stabilizes the flat geometry of DPPC monolayers, especially with high surface pressure.

The goals of conducting an MD simulation can be categorized into studying statistical properties and investigating dynamical processes. Before taking statistics, one must ensure equilibrium has been reached and that the trajectories from the equilibration have been discarded from the analysis. The most common approach to judge if the system has entered equilibrium is to investigate the trend of various energies, including total, kinetic, potential and other energies belonging to various degrees of freedom. If at least one of them is still displaying a systematic increase or decrease, the system is still not in equilibrium. This is, however, not a sufficient criterion and other quantities, e.g., the number of hydrogen bonds, must be monitored. In addition, analysis of fluctuations is often a useful way to analyze equilibrium.

One of the most important characterization for the behavior of monolayers is the surface tension/pressure to area per lipid isotherms. From the pressure tensor in the simulation

box, the surface tension of a monolayer can be evaluated [93] as

$$\gamma = \langle (P_N - P_L) \cdot L_z \rangle / 2 = \langle (P_N - P_L) \rangle \cdot L_z / 2, \tag{2.1}$$

where L_z is the box size in z-direction, $P_N = P_{zz}$ is the normal pressure and the third diagonal component of the pressure tensor, $P_L = (P_{xx} + P_{yy})/2$ is the lateral pressure and P_{xx} and P_{yy} are the first and second components of the pressure tensor. The brackets denote averaging over time. The second equality applies only to NVT simulations where the box size in z-direction is a constant, which applies to the case study here.

To get a more direct comparison between simulations and experimental data, the surface pressure of a monolayer can be evaluated, which can be accomplished by deducting the surface tension of the monolayer from the bare air/water surface tension under the same condition:

$$\Pi(A_L, T) = \gamma_0(T) - \gamma(A_L, T), \tag{2.2}$$

where $\gamma_0 \equiv \gamma_0(T)$ is the bare water/air surface tension which is a function of temperature, and both Π and γ are functions of the area per lipid A_L and temperature.

However no water model can reproduce the real bare air/water surface tension for a broad range of temperature which might be used in biological or physiological simulations. Therefore instead of using experimental data for bare air/water surface tension, the simulated values by the specific water model used in a simulation should be employed to ensure consistency. In addition, density profiling is a valuable tool to investigate the relative positioning of all relevant components in the simulation box and the change of it caused by other factors.

2.6 Discussion and conclusions

In this mini-review, we have provided a detailed discussion of how to set up monolayer simulations, the caveats and various technical details as well as software commonly used for such simulations. Our aim was not to provide a comprehensive review of the vast literature on the topic but rather to provide a fairly hands-on approach to help the interested readers to set up, run and analyze their own simulations.

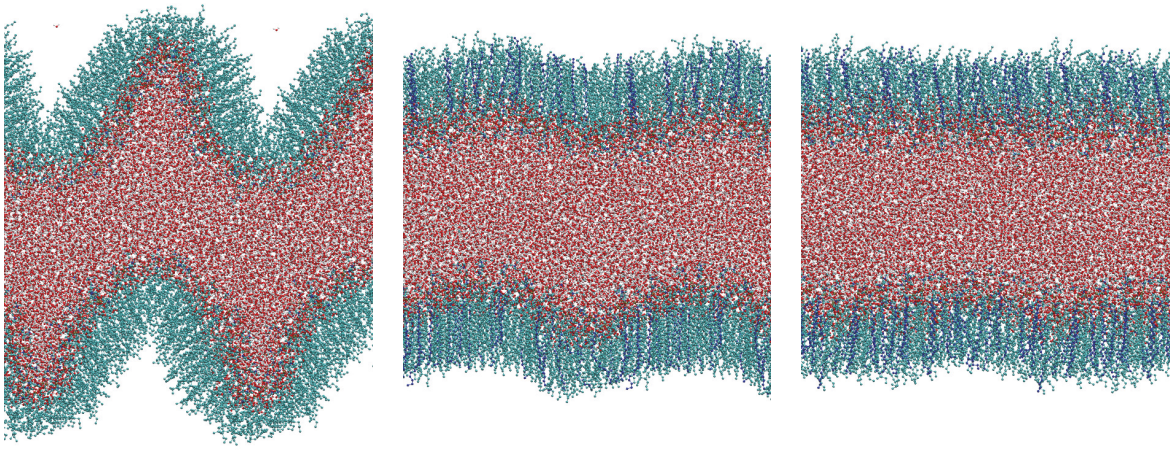

(a) (b) (c)

Figure 2.4: Pure DPPC monolayer and DPPC/CTAB mixtures at area per lipid 0.4 nm^2. (Left) High surface pressure at very low area per lipid induces buckling in pure DPPC monolayer. (Center) 20% cationic CTAB (deep blue) with 80% DPPC mixture has only very wild surface undulation. (Right) 30% cationic CTAB (deep blue) with 70% DPPC mixture resumes flat geometry even at very low area per lipid.

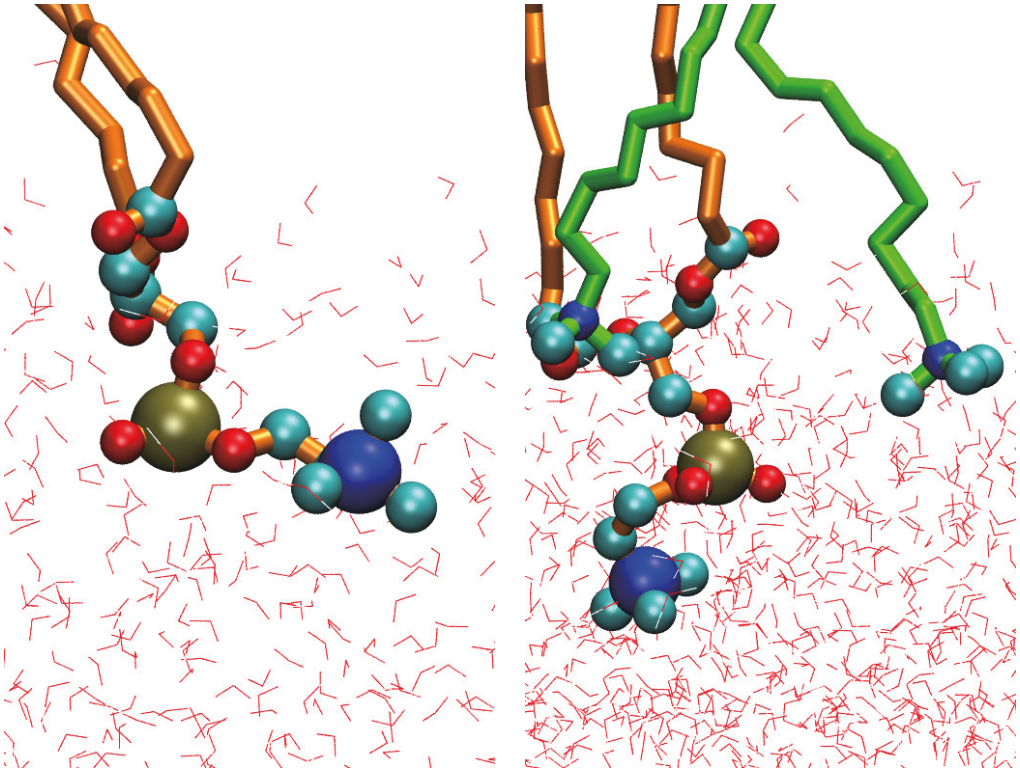

(a) (b)

Figure 2.5: Phosphorus (the large tan atom)-Nitrogen (the large blue atom) vector in PC headgroups reoriented by neighboring cationic CTAB. (Left) The P-N vector of DPPC is oriented almost parallel to the monolayer plane. (Right) The cationic CTAB (green lipid tail) essentially reorients the P-N vector of DPPC.

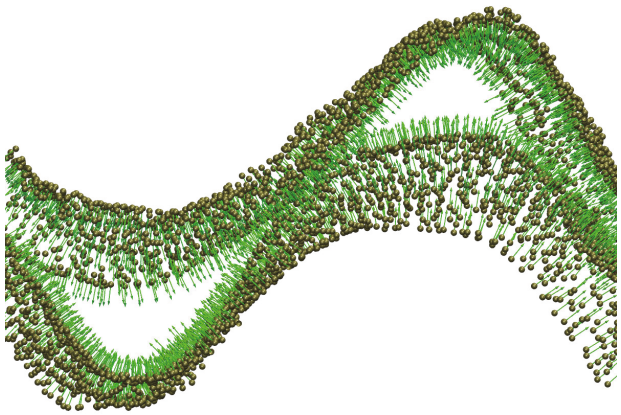

Figure 2.6: The normal vectors (green arrows) for highly buckled DPPC monolayers separated by a water slab. Each monolayer has 2048 DPPCs. Water is disabled in visualization for clarity. Phosphates were chosen to approximate the interface between water and DPPC monolayers. The normal vectors always point toward water.

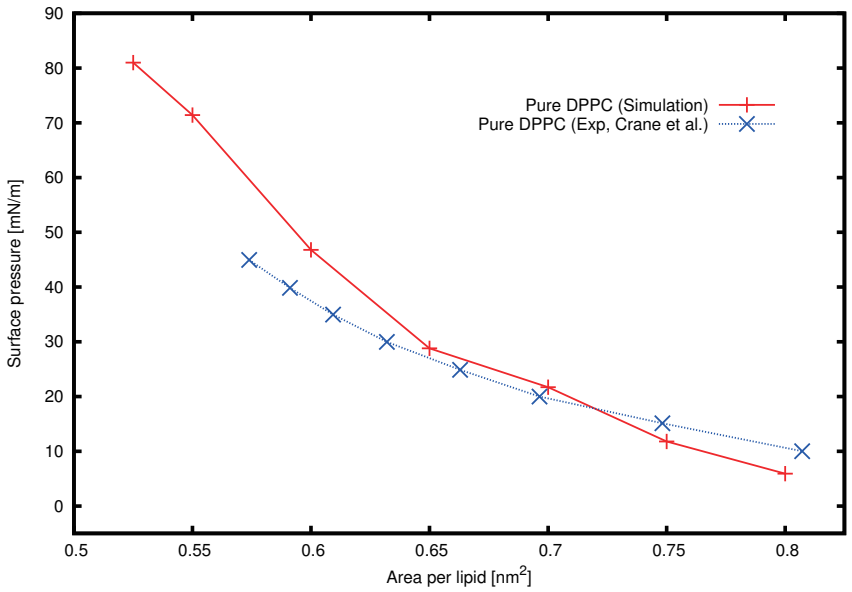

Figure 2.7: Surface pressure-area per lipid isotherms for pure DPPC monolayers simulated at 323K. The experimental data were obtained by Crane et al. [212]

Chapter 3

Molecular Dynamics Simulations of DPPC/CTAB Monolayers at the Air/Water Interface

The contents of this chapter were adapted from the article published in

Bin Liu, Matthew Hoopes, Mikko Karttunen. Molecular Dynamics Simulations of DPPC/CTAB Monolayers at the Air/Water Interface. The Journal of Physical Chemistry B 118, 11723-11737 Copyright (2014) American Chemical Society.

3.1 Introduction

Cationic lipid monolayers are promising packaging material for DNA/RNA based drug delivery[16, 213, 214, 215, 216, 217, 218, 219, 220, 221, 222, 223, 224]. They allow one to overcome the unfavorable properties of DNA/RNA as drugs, namely, the negative charges they carry and hydrophilicity, which would otherwise essentially compromise the circulation time and effectiveness of the drug[225].

Atomistic molecular dynamics (MD) simulations are a powerful yet versatile tool for investigating biomolecular systems. In particular, MD simulations can provide one insight into the atomistic details of the structure and dynamics of biomolecular systems. Not only do they complement to experiments, but they also allow investigations of various static and dynamic properties not readily accessible by current experimental methods.

In this work, we employed atomistic MD simulations to study lipid monolayers composed of both pure zwitterionic dipalmitoylphosphatidylcholine (DPPC), and mixtures of DPPC and cationic cetyltrimethylammonium bromide (CTAB) at the air/water interface. Lipid monolayers are excellent model systems that can capture some of the essential properties of micelle-like structures or liposomes[226] which are the basic structures of packaging materials for DNA/RNA based drug delivery; the relevance and utility of Langmuir monolayers as suitable models has been recently reviewed by Stefaniu et al.[219].

DPPC molecules are a major component of lung surfactant in human body[227]. CTAB is a common cationic surfactant[209] and it has been widely used for providing a buffer solution to extract DNA[228]. CTAB is currently being used and further developed for drug delivery applications. Peetla et al. used Langmuir film balance experiments and found that polystyrene nanoparticles with their surfaces modified with CTAB or DMAB (which can be regarded as a dichained version of CTAB) have stronger interactions with an endothelial cell model membrane than unmodified nanoparticles. Polystyrene can be regarded as a "placeholder" for drugs.[214] CTAB is also often used in combination with other molecules (such as chitosan, PLA, and PLGA) and such combinations have been reported to reach good uptake effincies for DNA delivery as has been shown by Basarkar et al.[215] Interestingly, Gaweda et al. compared CTAB to four other cationic agents for DNA compaction[216]. They found CTAB and CTAC to be the least efficient. They traced this to the structural properties of the hydrocarbon chains, in particular to their flexibility. These two apparently contradictory discoveries show the importance of understanding the structural aspects of CTAB and the details of its interactions with other molecules. Other studies in this direction include Mezei et al.'s very recent finding that the flexibility of CTAB's chain structure helps it to have better DNA helix/surfactant ratios as compared to some other compounds[217]. Moreover, CTAB mixtures can display a rich variety of structures, which could be useful for designing drug delivery agents. Small angle x-ray scattering was used by Krishnaswany et al. to study the structures of DNA, CTAB and hexanol as a function of hexanol content[218]. Interestingly, they found a structural transitions between hexagonal and lamellar structures. The use of cationic lipids, cationc surfactants (including CTAB) and polymers in cancer therapy has recently been reviewed by Bilensoy[16]. The above works demonstrate the value of CTAB or CTAB-containing mixtures as promising packaging materials for drug delivery.

Pure CTAB monolayers have been studied by MD simulations[229, 230] and experiments[231, 232]. However, as the above disucssion illustrates, in real applications cationic lipids are seldom the only component of the packaging material. Instead, mixtures consisting of zwitterionic lipids and cationic lipids are much more useful as they can integrate the desirable properties of both ingredients. Considering the amount of work devoted to the studies of

either DPPC monolayers/bilayers, or CTAB monolayers/micelles[89, 230, 233, 234, 235], and the importance of CTAB as a promising packaging material for drug delivery, it is surprising to see that, to the best of our knowledge, no published work has been done to investigate the properties of DPPC/CTAB mixtures, especially as a viable packaging material for gene delivery. Our objective is to investigate how the composition of the DPPC/CTAB monolayers influences their structural and electrostatic properties under conditions corresponding to the liquid-expanded phase.

By varying the molar fraction of CTAB, we found the CTAB molecules condense the DPPC/CTAB monolayers, i.e., they reduce the area per lipid under the same surface pressure. Further analysis of the DPPC P-N vector, radial distribution functions, molecular positions and binding suggest that while the condensation effect has a strong correlation with the P-N vector reorientation, contributions from other factors are important. Our work paves the way to further studies of DNA/RNA-monolayer complexes which could lead to real applications of DPPC/CTAB monolayer as a drug delivery agent.

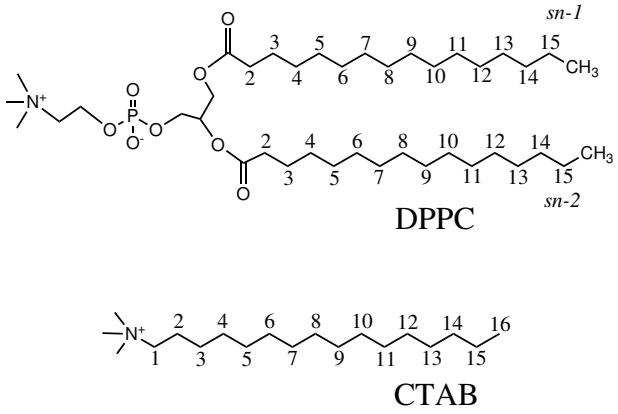

Figure 3.1: DPPC and CTAB molecules showing the numbering of carbons in the acyl chains.

3.2 Methods

The DPPC parametrization was obtained from Tieleman et al[236]. and the GROMOS96 53a6 force field[71] was used for the simulations. The partial charges of the CTAB cation were obtained by using the quantum chemistry package GAMESS-US[176, 177] to perform the calculations at Mller-Plesset level 2 using 6-31G(d,p) basis set[179, 180, 181].

The Polarized Continuum Model (PCM)[194, 195, 196, 197] was used to take the influence of the aqueous environment into account. Four sets of partial charges, i.e., Natural Population Analysis (NPA) by using the Natural Bond Orbital (NBO) module[193], Mulliken population analysis[185, 186], Lwdin population analysis[187, 188] and Electrostatic Potential (ESP)[189, 190] were obtained. The NPA partial charges given by the NBO module were chosen to parametrize the CTAB cation as the NPA scheme is not sensitive to the choice of basis set, theory level or initial structure of the molecule being investigated[191, 192]. This was also the case in our quantum chemistry calculation for CTAB. The NPA partial charges obtained at Hartree-Fock level are very similar to the partial charges for CTAB parametrization obtained at Hartree-Fock level which has been used in the MD simulations of CTAB micelles by Cat et al.[233]. Our NPA partial charges are slightly different from the partial charges by Cat et al., as we took electron correlation into account by employing MP2 level calculations. The parametrization is available at: http://www.softsimu.net/downloads.shtml

The simulation box contains two symmetrical monolayers separated by a Simple Point Charge (SPC) water[76, 77] slab (see Figures 3.2 and 3.4). Similar setup has been employed in other MD studies of monolayers[237, 238, 239, 240, 241]. Another useful system setup for simulating monolayers is setting up a monolayer and a water slab and employing a wall potential to prevent water from escaping into vacuum[199]. The thickness of the water slab (> 4 nm), which is more than has been used in previous MD simulations of symmetrical DPPC monolayers[238], was carefully selected to prevent interactions between the two monolayers. Standard periodic boundary conditions were used in all three directions. The thickness of vacuum between the system and its periodic images in the z-direction was at least 20 nm, essentially eliminating interactions between them. Each simulated system consisted of 256 lipids, i.e., 128 lipids per monolayer. Both pure DPPC monolayers and mixtures composed of DPPC and CTAB were simulated. Mixtures with 20%, 30%, 40%, 50% CTAB molar fractions were obtained by randomly substituting CTAB molecules for DPPC molecules in a pure DPPC monolayer. Molar fractions are defined with respect to the total number of lipid molecules.

The GROMACS 4.5.5 software package[53] was used. Constant temperature simulations (NVT ensemble) were conducted at T=323 K using the V-rescale thermostat[84]. Langmuir-Blodgett trough experiments were mimicked by using a series of simulation box sizes. This protocol has been used in previous simulations of monolayers at the air/water interface[239, 240, 242]. The area per lipid is defined as the area of the simulation box in the x-y plane divided by the number of lipids, including both DPPC and CTAB, in the monolayer. Steepest descent energy minimization was first performed, followed by full dynamic simulations. Each of the simulation trajectories was 1 µs long with time step of 2

fs. The first 100 ns was discarded as equilibration period; 100ns was sufficient for reaching equilibrium as there were no changes in any macroscopic quantities, including energies, virials, temperature, pressure tensors and macroscopic geometries, etc. All the bond lengths except those for water molecules were constrained by using the P-LINCS algorithm[54]. Water molecules were constrained by the SETTLE algorithm[55]. Neighbor searching with group cutoff scheme was performed every 5 MD steps. Previous studies show that to be a safe update frequency for neighbor searching for lipid systems without pores[63]. Coulombic interactions were treated with the PME algorithm[57] with a cutoff of 1.3 nm. The PME algorithm was used for its accuracy[56, 60, 65, 206], and it is also computationally efficient[56, 207]. Shifted van der Waals interactions were employed with a cutoff of 1.0 nm and shifting starting from 0.9 nm. Shifted van der Waals interactions were used instead of plain cutoff as the latter may be a source of artifacts[68]. Overall charge neutrality was maintained by adding chloride counterions instead of bromide counterions. This approach is justified by the fact in MD simulations, ions mostly behave as point charges such that ions carrying the same charges but with different mass have little difference in affecting the properties of monolayers or bilayers. The trajectories were visualized by VMD[210, 211].

3.3 Results

Snapshots at the end of the 1 µs trajectories are shown in Figures 3.2, 3.3 and 3.4. The pure DPPC monolayer (Figures 3.2 and 3.3) shows severe buckling when the area per lipid is 0.5 nm^2 or below. Monolayer buckling under high surface pressure, and eventual collapse, have been observed in experiments[243, 244, 245, 246, 247]. In addition, the buckling of lung surfactant monolayers in which DPPC is a major component has been studied by MD simulations by Baoukina et al[88, 248]. They described monolayer buckling as a stage of monolayer collapse which is initiated by undulations. Monolayer buckling has been also reported in the simulations of sodium alkyl sulfate surfactant monolayers at the water/trichloroethylene interface[249]. In contrast, buckling is far less obvious in mixtures with 20% CTAB (Figure 3.4d). In mixtures with 30% CTAB or higher (Figures 3.4a, 3.4b, 3.4c), buckling almost totally disappears. The cationic CTAB lipids show a high tendency to stabilize and maintain the flat geometry of monolayers under very high surface pressure.

3.3.1 Surface Tension/Surface Pressure to Area Per Lipid Isotherms

Monolayers are typically characterized by surface tension-area per lipid and surface pressure-area per lipid isotherms. The surface tension of a monolayer can be calculated from the

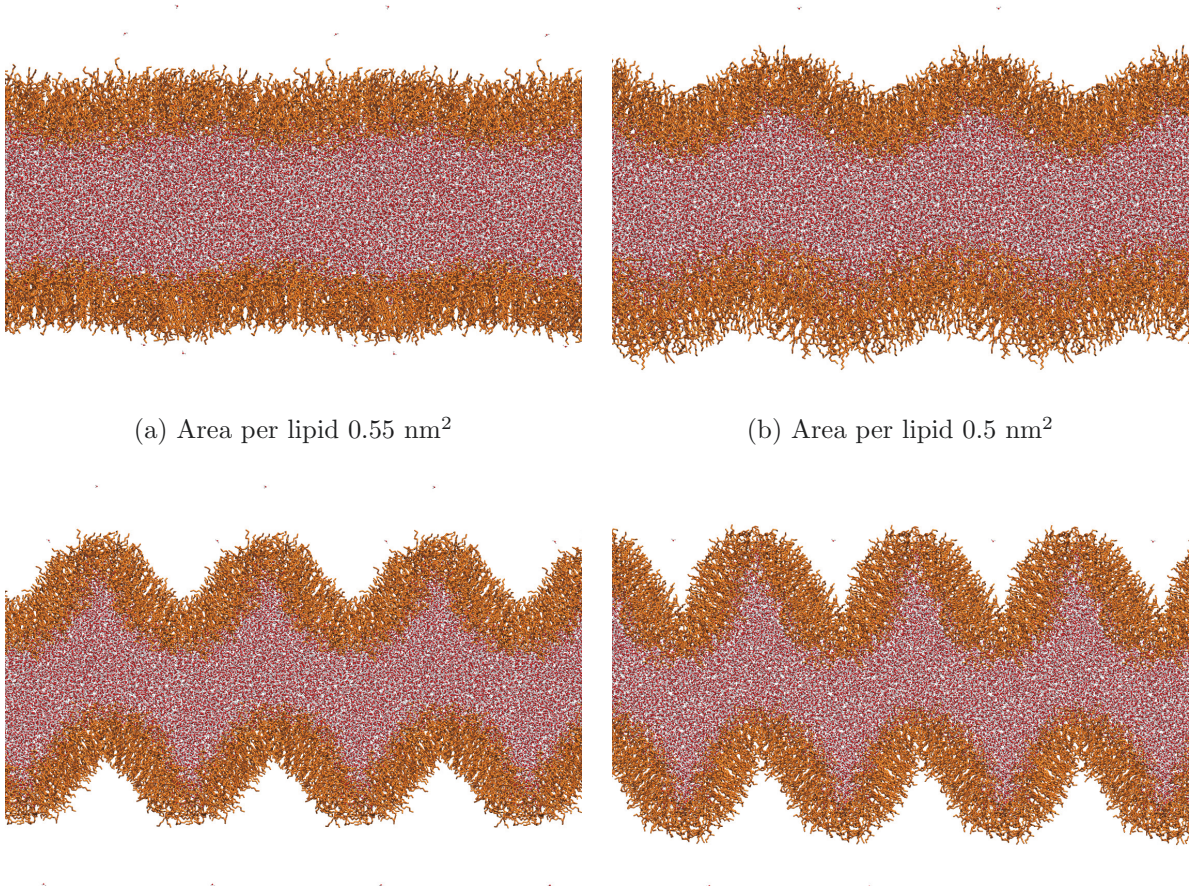

(a) Area per lipid 0.55 nm^2

(b) Area per lipid 0.5 nm^2

(c) Area per lipid 0.45 nm^2

(d) Area per lipid 0.4 nm^2

Figure 3.2: Snapshots of pure DPPC monolayers at the end of the 1 µs trajectories. DPPC shows as orange, oxygen in water shows as red dots, hydrogen in water shows as white dots. Monolayer buckling becomes severe as area per lipid decreases below 0.5 nm^2.

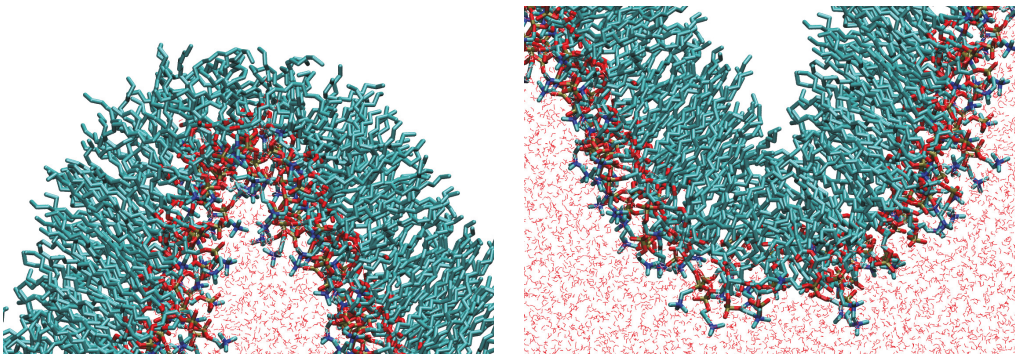

(a) (b)

Figure 3.3: Snapshots of the buckled pure DPPC monolayer with area per lipid 0.4 nm^2. They show the high curvature areas of Figure 3.2d.

diagonal components of the pressure tensor in the simulation box[93]:

$$\gamma = \langle (P_N - P_L) \cdot L_z \rangle / 2 = \langle (P_N - P_L) \rangle \cdot L_z / 2, \tag{3.1}$$

where L_z is the box size in z-direction, $P_N = P_{zz}$ is the normal pressure, $P_L = (P_{xx} + P_{yy})/2$ is the lateral pressure and the brackets denote averaging over time. The second equality applies only to NVT simulations when the box size in z-direction is fixed, as is our case. This equation is valid only when the monolayer maintains a flat geometry. When buckling occurs, an additional term is needed to take the local curvature into account[108, 250]. This term was not considered when the surface tensions were calculated. Similar issues have been reported in Baoukina et al.'s simulations of lung surfactant[93].

The calculated surface tension-area per lipid isotherms are shown in Figure S.1. At the same area per lipid, the surface tension of the monolayers increases as the molar fraction of CTAB increases. This effect is obvious when the area per lipid of the monolayer is low, and diminishes as the area per lipid increases. Second, negative surface tension appears with stable flat monolayer geometry for mixture monolayers of DPPC and CTAB when area per lipid is below 0.5 nm^2 (Figures 3.4b,3.4c,3.4d). This means enlarging the interficial area between air and water with the presence of the DPPC/CTAB surfactant mixtures can be energetically favorable. The role the cationic CTAB plays can be summarized as a cohesive force to stabilize the monolayer. Third, one can see an anomaly in the isotherm for pure DPPC monolayer when the area per lipid is small. The irregular increase of surface tension with decreasing area per lipid can be explained by the buckling of the pure DPPC monolayer (Figures 3.2b,3.2c,3.2d).

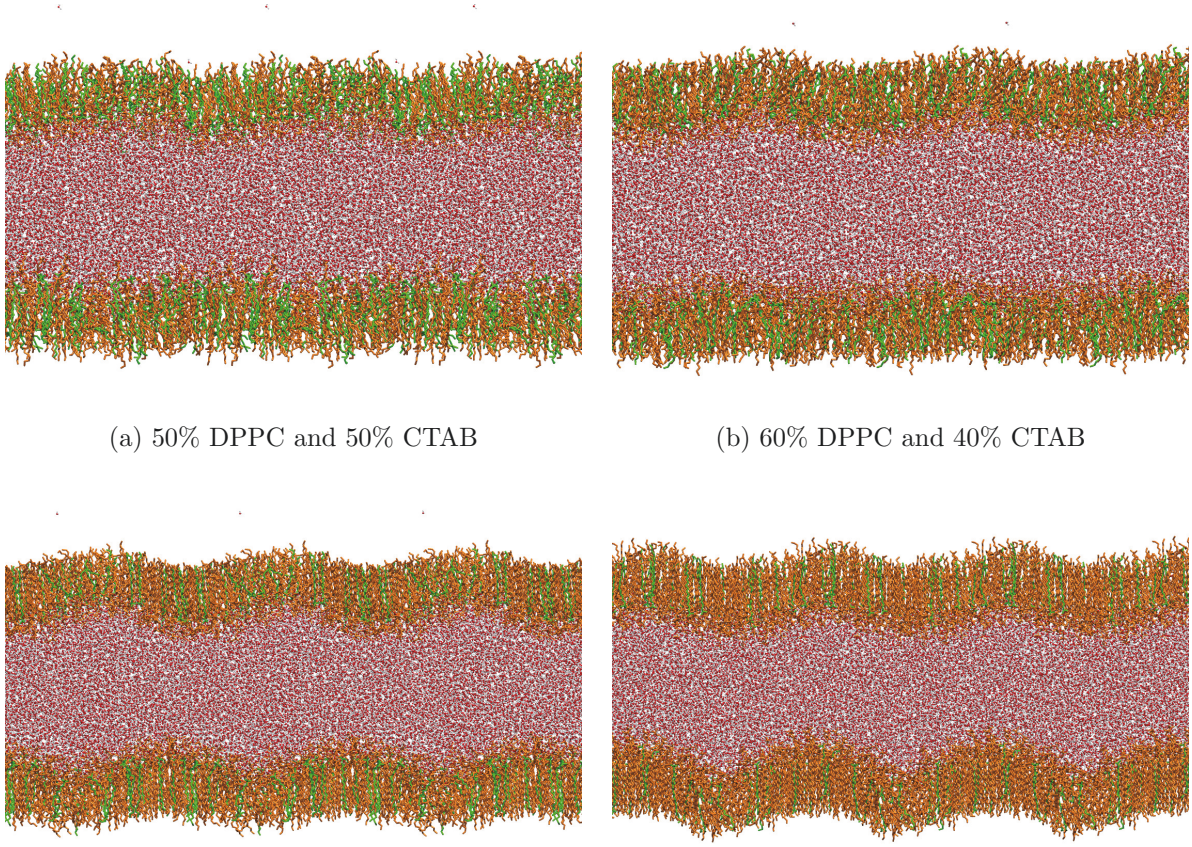

(a) 50% DPPC and 50% CTAB

(b) 60% DPPC and 40% CTAB

(c) 70% DPPC and 30% CTAB

(d) 80% DPPC and 20% CTAB

Figure 3.4: Snapshots of monolayers at the end of the 1 µs trajectories with various CTAB molar fractions and area per lipid 0.4 nm^2. DPPC shows as orange, CTAB as green. Oxygen in water shows as red dots, hydrogen in water as white dots. Compared to the pure DPPC monolayers shown in Figure 3.2, the mixtures shown here maintain flat geometry at very low area per lipid (0.4 nm^2). The system containing 20% CTAB displays very mild buckling.

The surface pressure of a monolayer is a more convenient quantity for direct comparison between simulations and experimental data. The surface pressure of a monolayer can be directly calculated from the surface tension of the monolayer and bare water/air surface tension under the same condition,

$$\Pi(A_L, T) = \gamma_0(T) - \gamma(A_L, T), \tag{3.2}$$

where $\gamma_0 \equiv \gamma_0(T)$ is the bare water/air surface tension which depends on temperature, and both Π and γ depend on the area per lipid A_L and temperature. To our knowledge, no water model can reproduce the correct bare water/air surface tension for the whole temperature range of interest in biological or physiological simulations. Since the SPC model is employed, 49.0 mN/m is used as the bare water/air surface tension at 323 K[97], instead of using the experimental value 67.6 mN/m to ensure the consistency[251].

Figure 3.5 shows that the calculated surface pressure isotherm for the pure DPPC monolayer is in good agreement with the experimental data[212] and MD simulation data[252]. Our data overlaps with the experimental data when the area per lipid is between 0.65 nm^2 and 0.8 nm^2. Below 0.65 nm^2, small deviation, although within the margin of error, from the experimental data can be seen.

Experimental studies of CTAB containing monolayers have mostly focused on containing both CTAB and other components, e.g., PG lipids or alcohol, at various interfaces, including air-water interfaces or water-solid interfaces[231, 232, 253, 254, 255, 256, 257]. The surface pressure-area isotherms for pure CTAB monolayers have been measured by Knauf et al.[231]and Nakahara et al.[232] under various conditions. Their data are shown in Figure 3.5. The measurement by Knauf et al. was done on 0.1 M NaCl at the airwater interface at 293 K. The measurement by Nakahara et al. was done with 5 M NaBr and 5 M NaCl at the air-water interface at 298.2 K. Compared to CTAB-DPPC mixtures, the pure CTAB monolayers have significantly lower surface pressure at low area per lipid region, which is a further proof of the condensation effect of the cationic CTAB. With large area per lipid, the pure CTAB monolayers display slightly larger surface pressure than the mixtures, which could be attributed to different experimental/simulational conditions.

An interpretation of the surface tension-area per lipid isotherms or the surface pressure-area per lipid isotherms is the condensation effect of the cationic CTAB on DPPC/CTAB monolayers, i.e., at the same surface tension or surface pressure, monolayers with higher CTAB molar fraction have smaller area per lipid. The same effect of another naturally occurring cationic lipid sphingosine on POPC monolayers has been reported in experiments[258]. This condensation effect is largely attributed to reorientation of the P-N vector in the headgroups of DPPC (see the discussion in P-N vector orientation section).

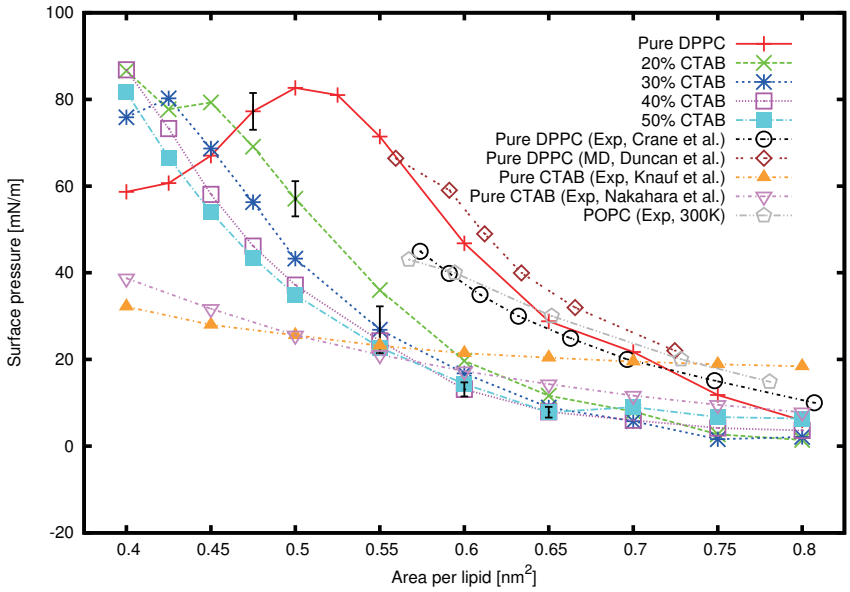

Figure 3.5: Pressure-area isotherms for the simulated systems. The molar fractions of CTAB in the monolayers are 0% (red, solid), 20% (green, long-dashed), 30% (blue, short-dashed), 40% (magenta, dotted), and 50% (cyan, dotted-long dashed). The experimental data for pure DPPC monolayers are shown as a black, dotted-short dashed line with open circle markers[212]. The atomistic MD simulation data for pure DPPC monolayers are shown as brown rhombus markers[252]. The experimental data for pure CTAB monolayers are shown as orange, dotted-short dashed line with open triangle markers (0.1 M NaCl, 293 K)[231] and violet, dotted-short dashed line with filled triangle markers(5 M NaBr and 5 M NaCl, 298.2 K)[232]. Each curve for the simulation data has one characteristic error bar which was obtained by block averaging[259]. The experimental data for POPC monolayers measured at 300 K ($T_m \approx 270$K [260]) is also shown as gray pentagons, as they are also in the LE phase[261]. The condensation effect of CTAB on DPPC monolayers, i.e., systems with higher CTAB molar fraction has lower area per lipid at a specific surface pressure, is shown. The decrease of surface pressure of pure DPPC monolayer and mixtures with 20% and 30% CTAB molar fractions at low area per lipid is caused by monolayer buckling.

3.3.2 Water Orientation and Density Profiles

Figure 3.6 shows how the molar fraction of CTAB affects water dipole orientation. The pure DPPC monolayer shows a single high peak which is highly correlated to the peaks of the density profiles of phosphate and choline groups (Figure S.2). With increasing CTAB molar fraction, the height of the main peak diminishes and valleys develop. The position of the valleys are correlated to the peak of the density profile of chloride ions which are generally concentrated near the choline groups (Figure S.2). Similar correlation has been reported in the MD studies of DPPC bilayers by Feller et al.[237] and DMPC monolayers by Alper et al.[262]. Our water orientation agrees with Gurtovenko et al.'s results on water orientation in the vicinity of DMPC/DMTAP bilayers in both trend and magnitude[171].

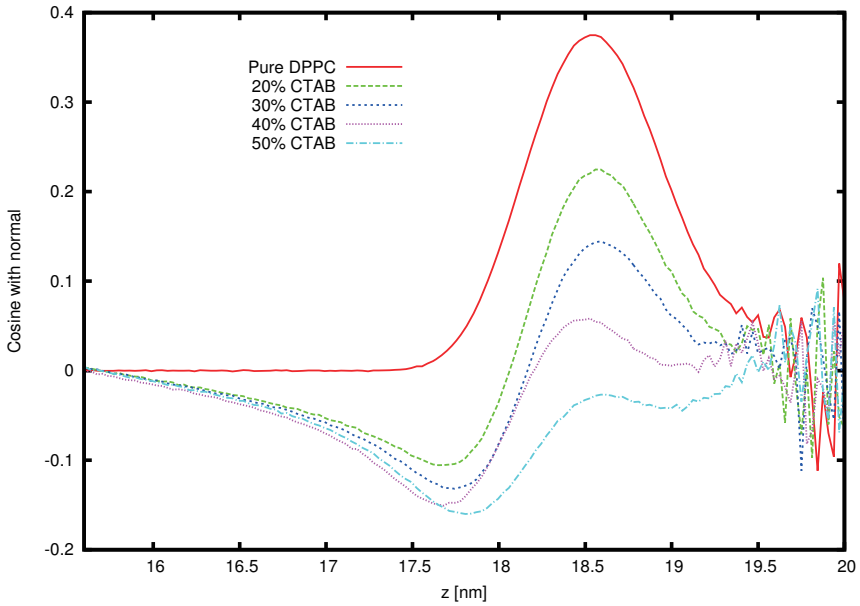

Figure 3.6: Water dipole orientation measured between 100 ns and 1 µs for the pure DPPC monolayer and mixtures with area per lipid 0.65 nm^2. The y-axis corresponds to the midplane of the water slab. The noise on the right is caused by very small number of water molecules escaped from the water slab into air. The peaks and valleys of water orientation are strongly correlated to the peaks of the density profiles of the charged functional groups (Figure S.2), indicating the charged groups' strong modulation effect on water orientation.

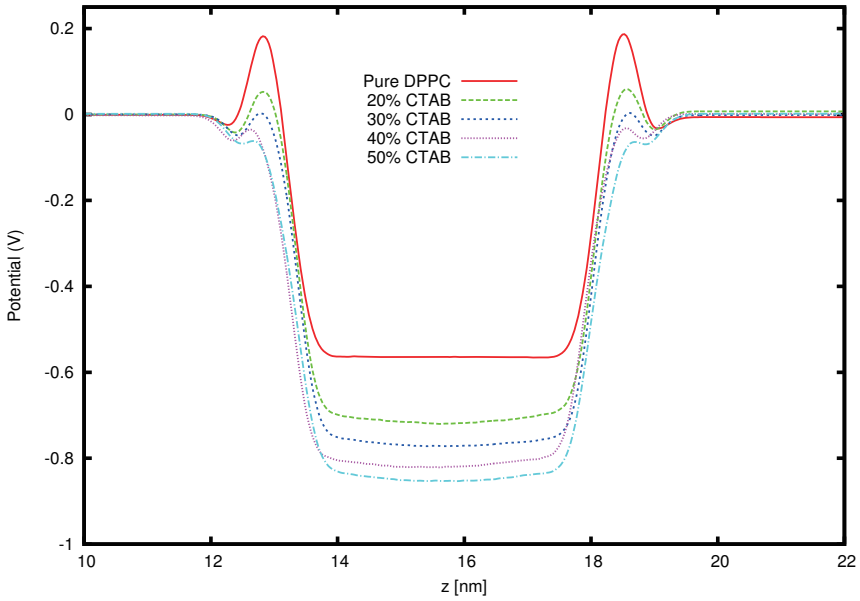

Figure 3.7: Electrostatic potentials of monolayers with various CTAB molar fractions at the area per lipid = 0.65 nm^2. The peaks for the pure DPPC monolayer correspond to the peaks of the density profiles for phosphate and choline groups. The trend of decreasing heights of the peaks as the molar fraction of CTAB increases is a reminiscence of the corresponding water dipole orientation. Meanwhile, the potentials of the water slab regions decreases from -0.55 V to -0.83 V as the molar fraction of CTAB increases from zero to 50%.

3.3.3 Electrostatic Potential

Figure 3.7 shows the electrostatic potentials of monolayers with various CTAB molar fractions. Generally, the electrostatic potentials of symmetrical monolayers separated by a water slab have a well shape. The well depth increases as the molar fraction of CTAB increases. Similar electrostatic potential profiles, including very similar value for the well depth for DMPC bilayers, have been reported by Gurtovenko et al.'s MD studies of cationic DMTAP/DMPC bilayers[171]. The pure DPPC monolayer and mixtures with the molar fraction of CTAB lower than 40 % also have peaks at the positions of the peaks of the corresponding density profiles for phosphate and choline groups. The trend of decreasing heights of the peaks as the molar fraction of CTAB increases is a reminiscence of the corresponding water dipole orientation.

3.3.4 Monolayer Thickness

Monolayer thickness is an important characteristic of the interfacial region at the air/water interface. We define the thickness as the full width of the lipid density profile at half of the maximum density in the bilayer. Figure 3.8 shows that CTAB reduces the monolayer thickness. This effect diminishes as area per lipid increases. Our algorithm for evaluating monolayer thickness only works well for monolayers without buckling. When a monolayer buckles, local curvature is introduced into the monolayer making even the concept of thickness not well-defined. Therefore, the datapoints presented by triangles in Figure 3.8 which correspond to the pure DPPC monolayer with buckling can not reflect the true thickness of it. The increase of monolayer thickness due to buckling was also observed by Baoukina et al.'s simulations of collapse of lung surfactant monolayers[88, 248]. In their case, buckling leads to monolayer folding, which also makes the concept of monolayer thickness not well-defined. In experiments, the process of the total thickness of a lysozyme monolayer as a function of surface pressure in a cycle of compression and decompression has also been observed[263], in which the dramatic increase of monolayer thickness was also attributed to buckling.

3.3.5 Hydrogen Bonding

Because neither DPPC nor CTAB have hydrogen donors and CTAB does not have acceptors either, the only two kinds of hydrogen bonding that can form in the simulated system are those between the phosphate groups of DPPC (acceptors) and water (donors), and

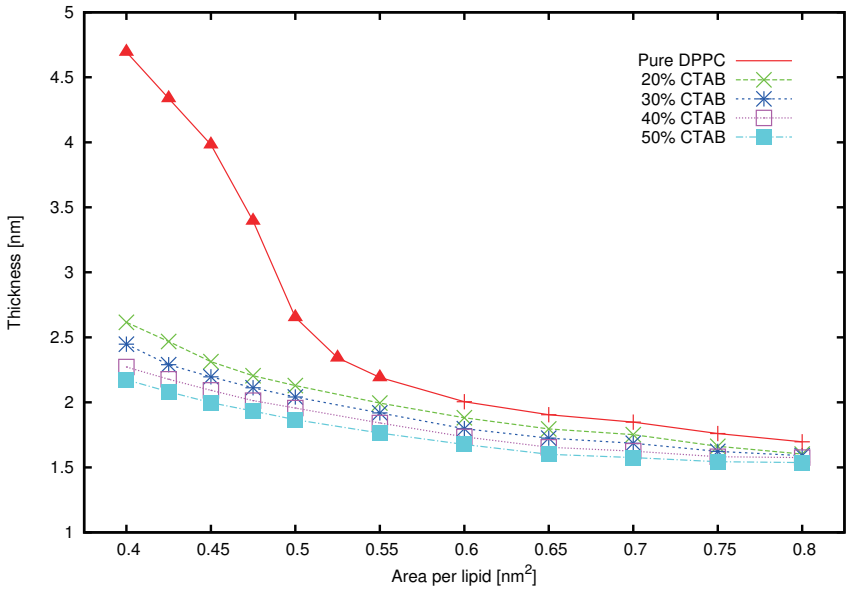

Figure 3.8: Monolayer thickness. The molar fractions of CTAB in the monolayers are 0% (red, solid), 20% (green, long-dashed), 30% (blue, short-dashed), 40% (magenta, dotted), and 50% (cyan, dotted-dashed). The error bars are of the same size as the symbols. The error bars were calculated from the difference between two leaflets in the same system. The cationic CTAB lipids have significant effect of reducing monolayer thickness, especially at low area per lipid. The datapoints with triangle symbols for the pure DPPC monolayer can not reflect the true thickness of the monolayer as they were measured with the presence of severe buckling which introduces local curvatures into the monolayer, making even the concept of monolayer thickness not well-defined.

those between the carboxyl groups of DPPC (acceptors) and water (donors). The usual geometrical criterion involving distance and alignment was used to determine hydrogen bonding. The cutoff radius for donor-acceptor pairs is 0.35 nm which corresponds to the first minimum of the radial distribution function of SPC water[264]. The cutoff angle for hydrogen-donor-acceptor angle is 30 degrees[265]. Figure 3.9 shows the number of hydrogen bonds normalized with respect to the DPPC molar fraction in the monolayer to get meaningful comparison between systems with various CTAB molar fractions. The two figures show exactly the same trend, i.e., the number of hydrogen bonds between DPPC and water increases with CTAB molar fraction, but the effect diminishes as the CTAB molar fraction approaches 40%. Again dramatic increase in the number of hydrogen bonds between pure DPPC monolayer and water is caused by buckling: more DPPC lipids are exposed to water.

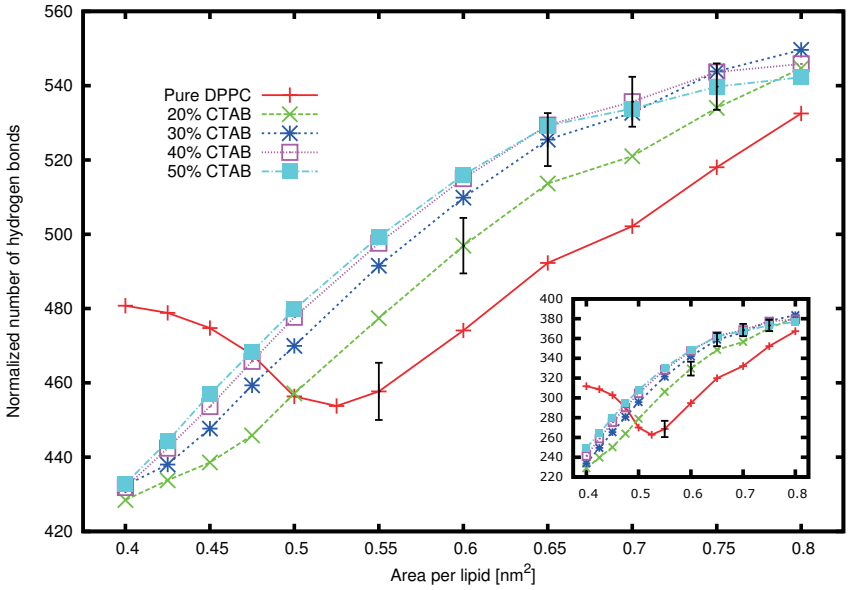

Figure 3.9: Hydrogen bonds between phosphate groups of DPPC and water normalized by the molar fraction of DPPC. Inset: Hydrogen bonds between carboxyl groups of DPPC and water normalized by the molar fraction of DPPC. Each curve for the simulation data has one characteristic error bar which is the standard deviation obtained from the statistics of the trajectories between 100 ns and 1 µs. CTAB has the effect of increasing hydrogen bonding formation. The dramatic increase of hydrogen bonding for pure DPPC monolayer is caused by buckling at high surface pressure.

3.3.6 Chain Order Parameter

Ordering of the DPPC hydrocarbon chains can be used to characterize the phase behavior[74, 75]. Ordering of nonpolar hydrocarbon chains in lipid monolayers is typically characterized by the deuterium order parameter S_{CD} measured through ^{2}H NMR experiments. If θ is the angle between a CD bond and the monolayer normal, the order parameter is defined as

$$S_{CD} = \frac{3}{2}\langle \cos^2 \theta \rangle - \frac{1}{2}, \tag{3.3}$$

separately for each hydrocarbon group. The brackets stand for averaging over time and molecules. Since we employed a united atom force field, the positions of the deuterium atoms are not directly available but have to be reconstructed from the coordinates of three successive nonpolar hydrocarbons, assuming an ideal tetrahedral geometry of the central CH_2 group. The coordinates of both possible deuterium atoms for each carbon were reconstructed and both were taken into account to give the final contribution to the order parameter[266, 267, 268]. $S_{CD} \in [-\frac{1}{2}, 1]$, with 1 indicating perfect alignment with respect to the z-axis, and -1/2 indicating perpendicular orientation with respect to the monolayer normal. Value of zero indicates isotropic orientation.

Figure 3.10 shows the averaged chain order parameters in pure DPPC monolayers. The experimental data for chain order parameter of DPPC monolayer at the air/water interface are not available as the NMR measurements of chain order parameter still require a solid substrate. Some experiments [269, 270] which used various solid substrates, including quartz and indium tin oxide, indicate that the overall averaged chain order parameter ranges from 0.09 to 0.27 for DPPC monolayers. Our results (Figure 3.10) show that the averaged chain order parameter ranges from 0.07 to 0.27.

An interesting comparison can be made between chain order parameter profiles of the acyl chains in simulated DPPC monolayers and those in DPPC bilayers investigated experimentally and by simulation. Figure S.3 shows our simulation results for chain order parameter profiles of the acyl chains in DPPC monolayers with area per lipid = 0.6 nm^2 and area per lipid = 0.65 nm^2, as well as the results for DPPC bilayers obtained from both experiments[271, 272] and MD simulations[65, 273, 274]. Figure S.3 shows that despite of having different structures (monolayer vs bilayer), their results are generally very similar to our simulation results at area per lipid = 0.65 nm^2. Only for the first to the eighth hydrocarbons, the simulated DPPC monolayer with area per lipid = 0.65 nm^2 has slightly lower chain order parameters than DPPC bilayers have. For the other hydrocarbons, the difference is negligible. Even the difference in chain order parameters for the first to the eighth hydrocarbons can be fully explained by that all the values for area per lipid used or

measured in the experiments and simulations are higher than 0.6 nm^2 and slightly lower than 0.65 nm^2 (0.633 nm^2 by Petrache et al.[271], 0.627 nm^2 by using the Berger lipid model by Pandit et al.[273], 0.648 nm^2 by using the GROMOS 54A7 force field[275], 0.631 nm^2 by using the parameter set by Kukol et al.[276], 0.641 nm^2 by using the parameter set by Anézo et al.[277] simulated by Poger et al.[274]) and 0.645 nm^2 obtained by Patra et al.[65]. Another experimental studying reported 0.640 nm^2 for area per lipid in the L_α phase[278].

Figure 3.11 shows the order parameters for the acyl chains of DPPC with various CTAB molar fractions and different area per lipid. The average of two sets of order parameters for the *sn-1* and *sn-2* chains is shown here. The low order parameters for DPPC in pure DPPC monolayer with area per lipid 0.4 nm^2 (Figure 3.11a) and area per lipid 0.45 nm^2 (Figure 3.11b) is caused by buckling because each infinitesimal area of the monolayer has its own normal due to the curvature. As buckling gradually disappears with increasing area per lipid, the order parameters for DPPC in pure DPPC monolayer rapidly assume their normal range of values (Figures 3.11c and 3.11d). CTAB has the effect of making the acyl chains of DPPC less ordered as shown in Figure 3.11. The order parameters for DPPC's acyl chains decreases monotonically with increasing molar fraction of CTAB. Previous MD studies of cationic DMTAP/DMPC bilayers[171] and cationic DOTAP/DMPC bilayers[279] report that the chain order parameters for DMPC increase as the molar fraction of cationic DMTAP or DOTAP increases from zero to 50%, but decrease as it increases further from 50% to 89%. Such phenomenon was not observed in our simulations. This difference in behavior can be explained by two reasons. First, at a given area per lipid, higher CTAB molar fraction means lower surface pressure which can lead to lower chain order parameter. Second, CTAB has only one lipid chain instead of two lipid chains which can be found in DMTAP/DOTAP/DPPC. Therefore higher CTAB molar fraction means less steric constraints on DPPC lipid chains.

The order parameters also decreases with increasing area per lipid of the monolayer indicating higher area per lipid makes lipids' acyl chains less ordered.

3.3.7 P-N Vector Orientation

The orientation of the phosphatidylcholine headgroup of DPPC can be characterized by the vector connecting the phosphorus and the nitrogen atoms in the headgroup. Figure 3.12 shows that the molar fraction of CTAB in the monolayer is strongly correlated with the P-N vector orientation. In the pure DPPC monolayer, the P-N vector aligns almost parallel to the air-water interface with 9 degrees pointing to the water slab as the average

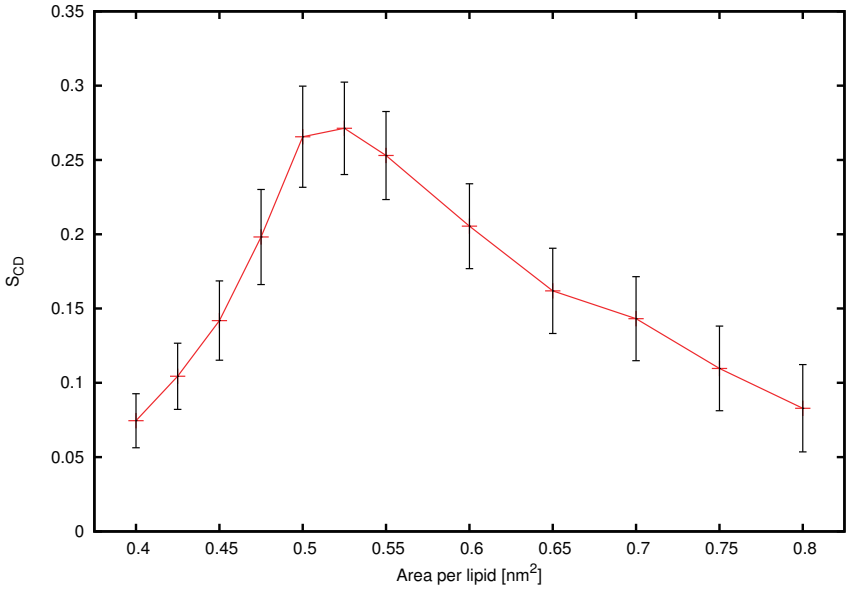

Figure 3.10: Chain order parameter (Eq.3.3) averaged over all carbons in aliphatic chains in pure DPPC monolayers at various area per lipid. The experimental data for averaged chain order parameter for DPPC monolayer at various air/solid interfaces range from 0.09 to 0.27[269, 270]. The error bars are the standard deviations of the corresponding data points.

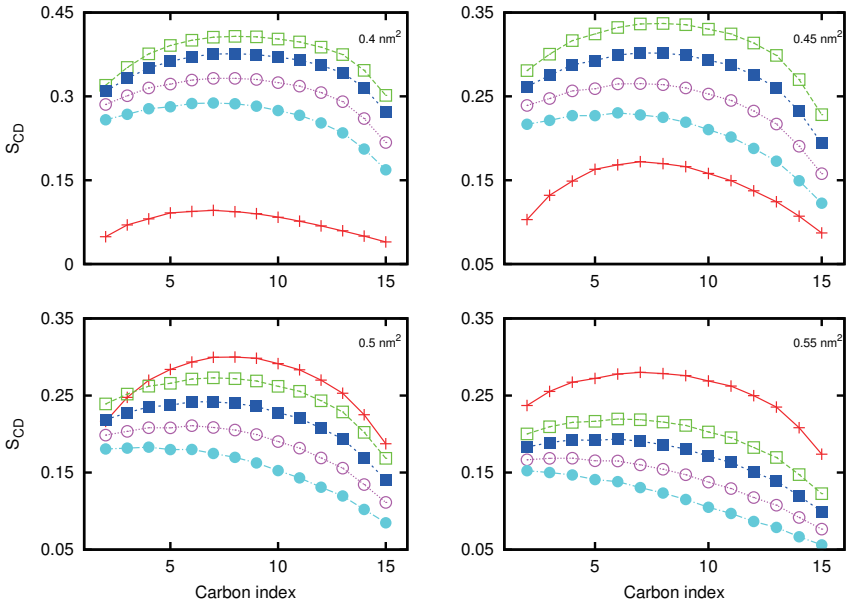

Figure 3.11: Chain order parameter averaged over the *sn-1* and *sn-2* carbon chains of DPPC. The molar fractions of CTAB in the monolayers are 0% (red, cross), 20% (green, open square), 30% (blue, filled square), 40% (magenta, open circle), and 50% (cyan, filled circle). The labels on the upper-right corners of the subfigures are area per lipid used in the simulations. The unusually low order parameters for pure DPPC monolayers when area per lipid is 0.4 nm^2 and 0.45 nm^2 are indication of severe buckling. CTAB has the effect of lowering the chain order parameter for the acyl chains of DPPC. The error bars are of the same size as the symbols.

angle between the P-N vector and the surface of the monolayer, which agrees with both the direct evidence from neutron scattering experiments [280] and indirect evidence from surface potential measurements[281, 282]. The MD simulation in Ref [283] shows that the angle of P-N vectors with the surface of the monolayer is 5 degrees pointing to water in average. Other MD simulation works[252, 284] show the probability distribution of P-N tilt angle has a maximum near 90 degree with respect to the z-axis. All experimental or theoretical results indicate the P-N vector orientation is mainly determined by the phase of the monolayer. They suggest that in liquid expanded (LE) phase, the P-N vector of the DPPC headgroups is more likely to have an in-plane orientation, while in the liquid condensed (LC) phase, it tends to tilt toward the normal with more features in the distribution of P-N orientation with respect to the monolayer normal, such as bimodal distribution at $T < T_m$ shown in Ref.[284]. As the simulations were performed at T=323 K (T_m = 314.4 K[285, 286]) for pure DPPC in aqueous solution, the monolayers remain in the LC phase. This is clearly manifested by our P-N vector orientation results for DPPC monolayers, which is supported by theoretical[252, 283, 284] and experimental studies[280, 281, 282]. A similar comparison can be drawn between the P-N vector orientation in DPPC monolayers and that in DPPC bilayers as we already did for the chain order parameters. A simulation study in Ref [287] shows the average value for the angle between the P-N vector and the bilayer plane is 9 degrees with the P-N vector pointing outward from the bilayer when the bilayer is in the liquid phase, which agrees with our results very well, while another simulation study in Ref [288] shows the average value is 19 degrees when the bilayer enters the gel phase. Similar results were also reported by other MD simulation studies[273, 274, 289]and measurements from neutron diffraction experiments[290].

The increasing molar fraction of CTAB in the monolayers essentially reorients the P-N vector more vertically. This phenomenon has an electrostatic origin. With the cationic CTAB molecules added, DPPC lipids tend to reorient their P-N vectors from a more lateral to a more vertical orientation with respect to the normal to maximize the distance between the positive charges of CTAB and the choline groups. P-N vector reorientation is correlated with the condensation effect, i.e., smaller area per lipid. This correlation can be explained by the fact that the headgroups of DPPC are quite rigid and their orientation determines the area per lipid to a large extent. Meanwhile, the condensation effect has also other important contributions, such as from the relative vertical positioning of CTAB. Besides lateral diffusion, CTABs can also adjust their vertical positions to minimize the total free energy consisting of the enthalpic contributions from electrostatic interactions between charged groups and entropic contributions from the relative positioning of acyl chains of DPPC and CTAB to allow the most favourable packing. CTABs can also bind to the two negatively charged regions of DPPC. This can be demonstrated by the resi-

dence time histogram of CTAB-phosphate and CTAB-carbonyl charge pairs (Figure S.4). CTAB spent 65.6% and 83.9% of the total simulated time with phosphate and carbonyl groups respectively in the charge pair state. The condensation effect of cationic lipids on zwitterionic lipid system has been reported by other simulations and experimental studies. Gurtovenko et al. employed MD simulations to investigate how DMTAP, another cationic monovalent lipid, condenses bilayers consisting of DMPC lipids[171]. Their major finding was the condensation effect is generally caused by DMTAP's effect on the P-N vector of their neighboring DMPC lipids, i.e., DMPC lipids in their first coordination shells. In another study, Zhao et al. showed on how cationic DOTAP lipids condense DMPC bilayers and reorient the P-N vector[279]. They showed that the average angle between the P-N vector of DMPC and the bilayer normal decreases monotonically as the molar fraction of DOTAP increases from zero to 90%. However, the average area per lipid as a function of DOTAP fraction was not monotonic. It decreased first until the DOTAP fraction reached 40%-50%, and then started to increase. Seelig et al.[222, 223] and Doux et al.[224] used NMR to investigate the effect of charged lipids on the P-N orientation of PC headgroups. Their basic conclusion is that the inclusion of negatively charged lipids leads to a more parallel orientation of the P-N vector of the PC headgroup with respect to the membrane surface, whereas incorporation of cationic lipids drives the positively charged end of the vector further away from the membrane surface toward the aqueous phase, leading to a more vertical orientation. Seelig et al. even proposed using PC headgroups as sensors of electric charge in membranes[222].

Another interesting feature in the figure is the changed trend of P-N vector orientation with respect to the area per lipid when the CTAB molar fraction increases from zero to 50%. In the pure DPPC monolayer and mixtures with low CTAB molar fraction, the average angle between the P-N vector and the normal is not sensitive to area per lipid. When the molar fraction of CTAB is above 30%, the average angle between the P-N vector and the normal is clearly dependent on area per lipid. The explanation for this phenomenon is the average angle between the P-N vector and the normal is mostly determined by coordination number N_C of DPPC with CTAB, i.e., the number of CTAB lipids in the first coordination shell of DPPC lipids, instead of area per lipid itself (see the detailed explanation in the Electrostatic Interactions of PC and TAB Headgroups section).

3.3.8 Diffusion

The lateral diffusion constant was computed through the mean square displacement (MSD) of atoms from a set of initial positions and performing least squares fitting to a straight

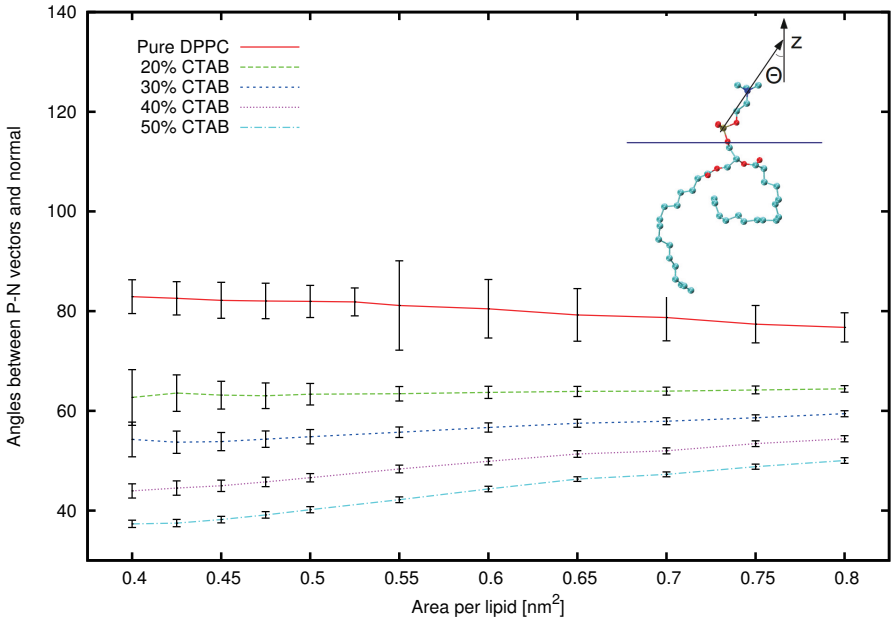

Figure 3.12: Phosphorus-nitrogen orientation in DPPC. The error bars are the standard deviations of the corresponding data points. The cationic CTAB essentially reorients the P-N vectors in DPPC's headgroups from a more lateral to a more vertical orientation, which is a major cause for the condensation effect of CTAB. A schematic representation for P-N vector orientation is shown in the inset.

line[53]:

$$D_\alpha = \lim_{t\to\infty} \frac{1}{4t}\langle r^2(t)\rangle = \lim_{t\to\infty} \frac{1}{4tN_\alpha} \sum_{i=1}^{N_\alpha} \langle r_i^2(t)\rangle. \tag{3.4}$$

Here, the subscript α denotes lipid species, i.e., in our case, either DPPC or CTAB. $\langle r_i^2(t)\rangle$ is the average squared lateral displacement of the i^{th} lipid belonging to type α at time t. N_α is the total number of lipids of type α in the system. The motion of the center of mass of the corresponding leaflet has been removed from $r_i^2(t)$. The error estimate is the difference of the diffusion coefficients obtained from fits over the two halves of the fit interval. The diffusion of DPPC lipids is dramatically fastened by the presence of CTAB (Figure 3.13). The diffusion of CTAB also increases with an increasing molar fraction of CTAB (the inset of Figure 3.13). This phenomenon can be explained by the fact that CTAB has a much smaller size compared to that of DPPC, which is far less obtrusive to lipid diffusion at given area per lipid. Useful information can be obtained by comparing our results to those by other MD studies of lipid systems. Gurtovenko et al. reports a simulated pure DMPC bilayer at 323 K has a lateral diffusion coefficient of $12.9 \pm 1.5\,\mu m^2/s$[171] and Patra et al. reports a simulated pure DPPC bilayer at 323 K has $12.7 \pm 0.5\,\mu m^2/s$. Various experiments report pure DPPC bilayers at 323 K have lateral diffusion coefficients ranging from $10\,\mu m^2/s$ to $13\,\mu m^2/s$[291, 292, 293]. Our simulations give a lateral diffusion coefficient of $15.45 \pm 2.03\,\mu m^2/s$ at the same temperature for pure DPPC monolayer with area per lipid = 0.65 nm^2. The slightly higher diffusion coefficient for pure DPPC monolayer is rather reasonable as the lipids in monolayers do not experience the obstruction from the other leaflet of lipids during diffusion as the lipids in bilayers do.

The lowest diffusion coefficients in Figure 3.13 are between $5\,\mu m^2/s$ and $10\,\mu m^2/s$, indicating a minimal diffusion length of 1.41 nm during the first 100 ns trajectories for equilibration which is 2.2 times the width of a single lipid in either x- or y- direction. This implies effective mixing of lipids during the equilibration stage, which is another proof of the correctness of our statistics.

3.3.9 Radial distribution functions

Figures S.5 and S.6 show the radial distribution functions (RDF) for the N-N and P-P pairs in the DPPC headgroups and the lateral (2D) radial distribution function for the center of mass of the DPPC molecules in the pure DPPC monolayer when area per lipid of the monolayer is 0.65 nm^2. The x-coordinates of the main peak ($x = 0.85$ nm) for N-N pairs, the main peak ($x = 0.54$ nm) and the second peak ($x = 0.91$ nm) and the valley ($x = 0.75$ nm) for P-P pairs match the results by Patra et al.[65] very well. However, the

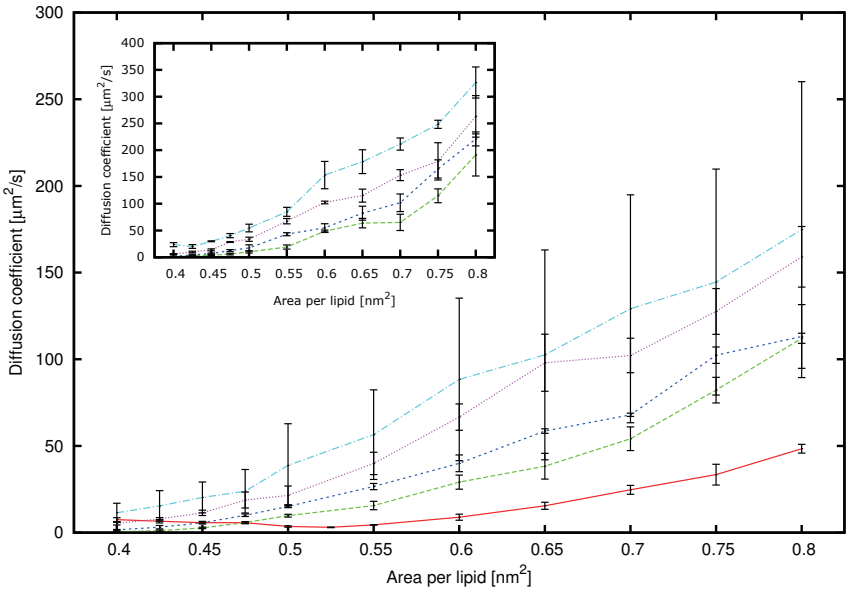

Figure 3.13: Lateral (2D) diffusion coefficient of DPPC as a function of area per lipid and CTAB molar fraction. Inset: Lateral(2D) diffusion coefficient of CTAB as a function of area per lipid and CTAB molar fraction. The molar fractions of CTAB in the monolayers are 0% (red, solid), 20% (green, long-dashed), 30% (blue, short-dashed), 40% (magenta, dotted), and 50% (cyan, dotted-dashed). The error bars are given by the difference of the diffusion coefficients obtained from fits over the two halves of the fit interval. The diffusion coefficients of both DPPC and CTAB increase essentially as the molar fraction of CTAB increases.

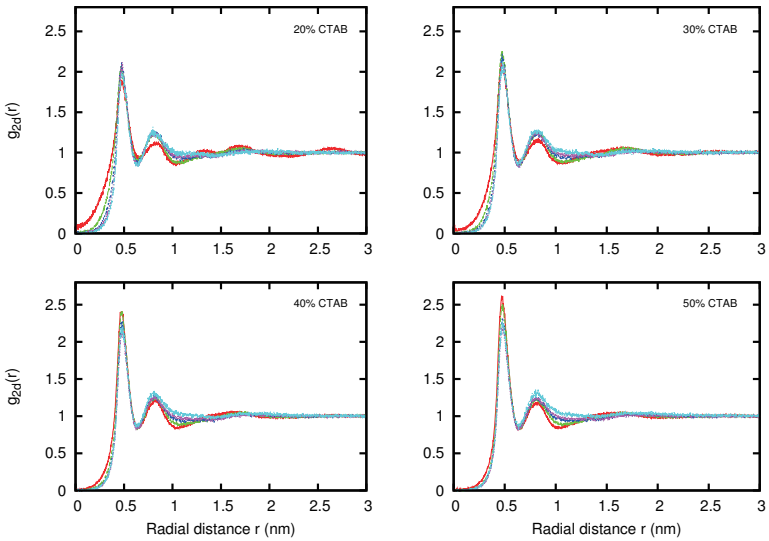

Figure 3.14: Lateral radial distribution functions (RDF) $g_{2d}(r)$ for the phosphorus atom in the DPPC headgroup and the nitrogen atom in the CTAB headgroup. The area per lipid of the monolayers are 0.4 nm^2 (red), 0.5 nm^2 (green), 0.6 nm^2 (blue), 0.7 nm^2 (magenta), and 0.8 nm^2 (cyan). Monolayers with higher CTAB molar fraction have significantly higher main peaks. However, the radii of the first coordination shells (the x-axis coordinates of the first valleys) are always approximately 0.64 nm and the x-axis coordinates of the main peaks are always approximately 0.47 nm regardless of CTAB molar fraction and area per lipid.

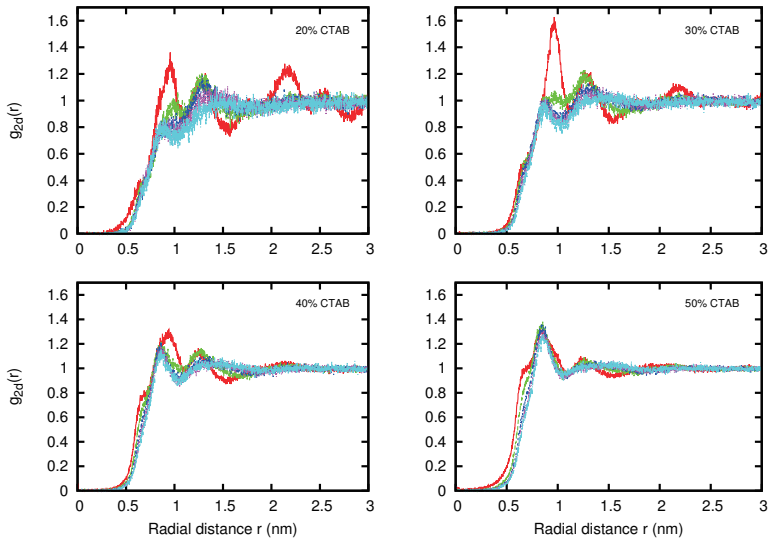

Figure 3.15: Lateral radial distribution functions (RDF) $g_{2d}(r)$ for pairs of nitrogen atoms in the CTAB headgroup. The area per lipid of the monolayers are 0.4 nm^2 (red), 0.5 nm^2 (green), 0.6 nm^2 (blue), 0.7 nm^2 (magenta), and 0.8 nm^2 (cyan). The oscillating RDFs with 20% or 30% CTAB molar fraction at area per lipid = 0.4 nm^2 are due to monolayer buckling. With stable flat geometry for the monolayer, the RDFs generally display a feature of double peaks, which has been observed in anionic DMPA Langmuir lipid monolayers[294].

y-coordinates between our RDFs and theirs are not directly comparable as in 3D RDFs for monolayers, due to the inhomogeneity of the system, i.e., nitrogens or phosphorus are highly confined to a very thin sheet of space, RDFs do not converge to unity at large distance[295].

The lateral radial distribution functions between the phosphorus atom in the DPPC headgroup and the nitrogen atom in the CTAB headgroup were also calculated. Figure 3.14 shows higher CTAB molar fraction makes the main peak of the lateral RDF of the corresponding monolayer higher. But neither area per lipid nor the CTAB molar fraction have significant effect on the x-axis coordinates of the main peaks (approximately 0.47 nm) or the first valleys (approximately 0.64 nm). This indicates the radius of the first coordination shell of DPPC with CTAB is generally a constant regardless of the system composition and area per lipid.

Figure 3.15 shows the lateral RDFs between the nitrogen atoms in the CTAB headgroup. Due to the electrostatic repulsion, the main peaks shift to larger distance (approximately 1.0 nm). Monolayer buckling manifests itself again in the RDFs with 20% or 30% CTAB molar fraction at area per lipid = 0.4 nm^2. When the flat geometry resumes, the RDFs generally display a feature of double peaks with significantly lower peak heights compared to those of RDFs for phosphorus (DPPC) and nitrogen (CTAB). Similar feature was observed in the RDFs for negatively charged phosphorus atoms in the anionic DMPA headgroups[294]. Although the superlattice model predicts the superlattice structure could exist in monolayer systems populated with either cationic lipids or anionic lipids[296], the size of our monolayer does not allow a proper comparison and hence we cannot validate the model.

3.3.10 Electrostatic Interactions of PC and TAB Headgroups

Figure S.7 shows the coordination number N_C of the phosphorus atom in DPPC with the nitrogen atom in CTAB as a function of area per lipid and CTAB molar fraction. The presence of the nitrogen atom in CTAB in the first coordination shell of the phosphorus atom in DPPC can also be interpreted as the formation of PC-TAB charge pairs. The most important feature on the figure is the higher the CTAB molar fraction, the larger the coordination number changes upon area per lipid changing from 0.4 nm^2 to 0.8 nm^2. When the molar fraction of CTAB is low, coordination number N_C of DPPC with CTAB does not change much upon the change of area per lipid as the CTAB molecules are dilute in the monolayers. With increasing CTAB molar fraction, the decrease in area per lipid will significantly increase coordination number N_C of DPPC with CTAB, making the effect of

CTAB reorientating the P-N vector in DPPC headgroups much more pronounced. Together with the information by Figure 3.12, this is another convincing evidence that supports the P-N vector orientation is mostly determined by the coordination number N_C of DPPC with CTAB, which could be a common feature of cationic lipids' effect on zwitterionic lipid systems with PC headgroups.

Another type of charge pair that can exist is PC-PC charge pair. It forms when the nitrogen atom of one DPPC molecule is within the first coordination shell of the phosphorus atom of another DPPC molecule. Figure S.8 shows the coordination number N_C of the phosphorus atom with the nitrogen atom in DPPC as a function of area per lipid and CTAB molar fraction. The intramolecular charge pairs have been excluded from the counting. The formation of PC-PC pairs was essentially inhibited by the presence of CTAB. Together with the information in Figures S.2 and 3.12, it can be concluded that in the pure DPPC monolayer, the phosphate groups and the choline groups generally lie in the same plane with similar z-coordinates, therefore there is relatively high probability for the formation of PC-PC charge pairs; with the presence of CTAB, the P-N vector of DPPC was reoriented such that the phosphate groups and the choline groups are no longer in the same plane, therefore the formation of PC-PC charge pairs was largely supplanted by the formation of PC-TAB charge pairs. Similar phenomenon, i.e., the inhibition of PC-PC charge pairs by PC-TAP(cationic) charge pairs, has been observed in the DMPC-DOTAP bilayers by Zhao et al.[279].

3.4 Discussion and conclusions

The design of novel delivery agents for DNA/RNA based drugs has attracted much attention due to their promising high selectivity[297] and low toxicity[298]. Cationic lipid monolayers, as model systems for micelle-like structures for packaging materials, provide a valuable platform to gain insight into the underlying properties of such structures[299].

In this paper, we employed MD simulations to study monolayers consisting of zwitterionic DPPC and cationic CTAB at the air/water interface when the conditions correspond to the liquid-expanded phase. First, agreement between simulations and existing experimental and simulational results for the pure DPPC monolayer was established. Then the molar fraction of CTAB was systematically varied to study the effect of composition on structural and electrostatic properties. The effect of the CTAB molecules can be briefly summarized as a condensation effect and stabilization restoring the monolayers' flat structure. For the pure DPPC monolayer, severe buckling was observed for areas per

lipid smaller than 0.55 nm^2 (Figure 3.2). Such buckling has a profound effect on monolayers' properties, e.g., thickness, hydrogen bonding, chain order parameter etc. With increasing CTAB molar fraction, the buckling diminishes quickly even at 20% CTAB molar fraction (Figure 3.4). This shows the cohesive effect the CTAB molecules exert onto the DPPC/CTAB monolayers. The combination of these effects leads to stable flat structures for the DPPC/CTAB monolayers under high surface pressure which could correspond to even negative surface tension. These properties are particularly desirable for obtaining inverted micelle-like structures[300] as packaging materials for drug delivery agents in which hydrophobic acyl tails facing outward to protect the encapsulated the drug during blood circulation and hydrophilic yet cationic headgroups facing inward to bind the anionic DNA/RNA drugs.

Density profile analysis was also performed to show the relative displacement of phosphate and choline groups of DPPC as a result of increasing CTAB molar fraction. We also show that water dipole reorients with the charged functional groups in its vicinity (Figures 3.6 and S.2).

Due to the lack of hydrogen bonding donors in the DPPC/CTAB monolayers, only two flavors of hydrogen bonding can exist, i.e., those between the phosphate groups and the carboxyl groups of DPPC as acceptors and water as donors. These two hydrogen bondings display exactly the same trend as a function of area per lipid and mixture composition. The CTAB molecules generally increase the number of hydrogen bonding between DPPC and water, but the effect diminishes when the CTAB molar fraction is higher than 30%. Similar to the thickness analysis, hydrogen bonding in the pure DPPC system shows a dramatic enhancement at low area per lipid, which again is caused by buckling when high surface pressure is applied.

The chain order parameter shows interesting behavior. First, the acyl chains in the pure DPPC monolayer have very similar order parameters to those in DPPC bilayers in the liquid-expanded phase and similar area per lipid. Second, the CTAB molecules reduce the order parameters of the DPPC lipids in the corresponding monolayer. Third, buckling affects the order parameters in the pure DPPC monolayer in a pronounced way. Significantly lower order parameter was observed in the pure DPPC monolayer with low area per lipid. CTAB molecules also reduce the thickness of the corresponding monolayer. Lipid diffusion generally becomes faster in the presence of CTAB molecules. This can be explained by the fact that CTAB has a smaller projected size on the x-y plane.

The analysis of P-N vector orientation provides an interpretation of the condensation effect of the CTAB molecules. In the pure DPPC monolayer, the P-N vector aligns almost parallel to the air-water interface (Figure 3.12). The presence of CTAB molecules reorients

the P-N vectors of their neighboring DPPC molecules into more vertical directions, which is highly correlated with the condensation effect but also depends on the vertical motion of the CTAB molecules, their binding to DPPCs negatively charged groups and even ions. To support this interpretation, RDF analyses were performed. Our calculations show the RDFs for the two key atoms in the DPPC headgroup (N-N and P-P) and the center of mass of the whole DPPC molecule in the pure DPPC monolayer have similar features as those for DPPC bilayers. The lateral RDFs for the phosphorus atom in the DPPC headgroup and the nitrogen atom in the CTAB headgroup and the subsequent calculation of the coordination number of DPPC with CTAB confirmed our view of how the CTAB molecules reorient the P-N vector of DPPC, i.e., the reorientation effect is generally limited to the first coordination shell of the CTAB molecule. To demonstrate other possible contributions to the condensation effect, the residence time histogram of CTAB-phosphate and CTAB-carbonyl charge pairs were also calculated.

3.5 Supplementary material

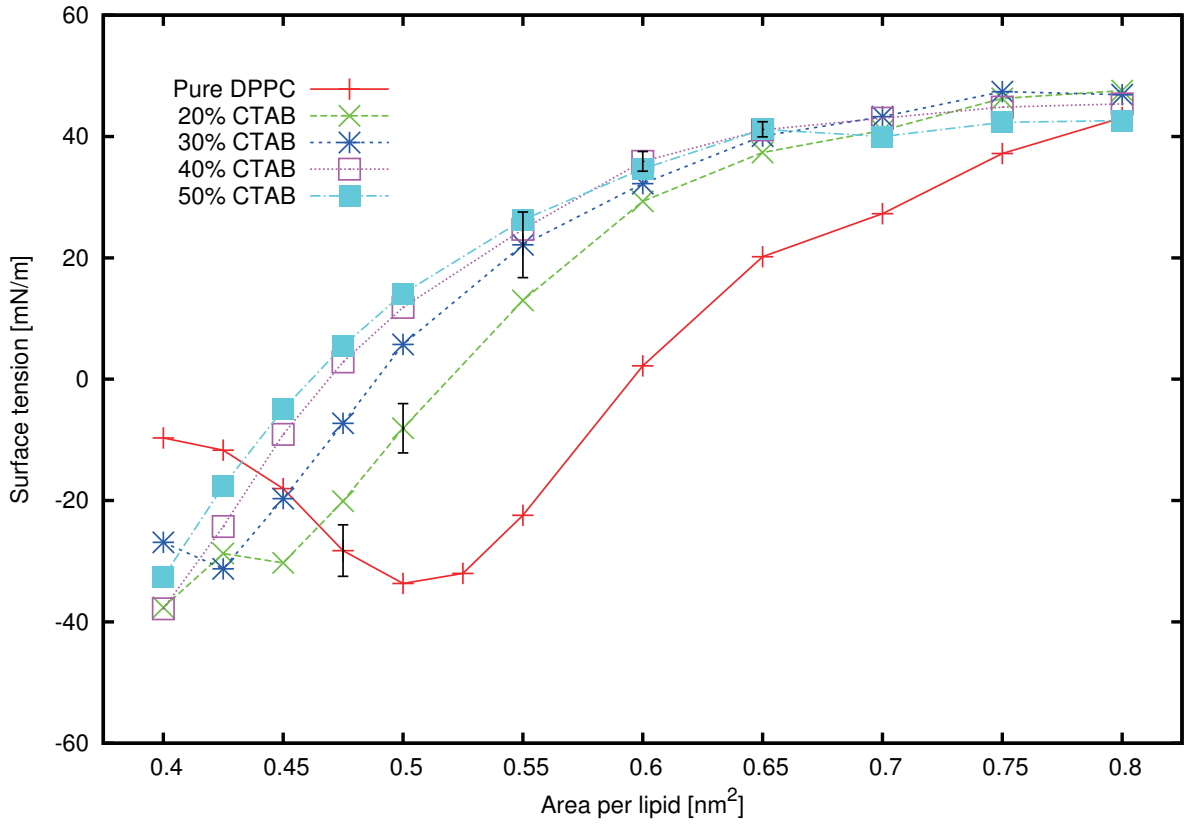

Figure S.1: Tension-area isotherms for the simulated systems. The molar fractions of CTAB in the monolayers are 0% (red, solid), 20% (green, long-dashed), 30% (blue, short-dashed), 40% (magenta, dotted), and 50% (cyan, dotted-dashed). Each curve for the simulation data has one characteristic error bar for clarity which was obtained by block averaging[259].

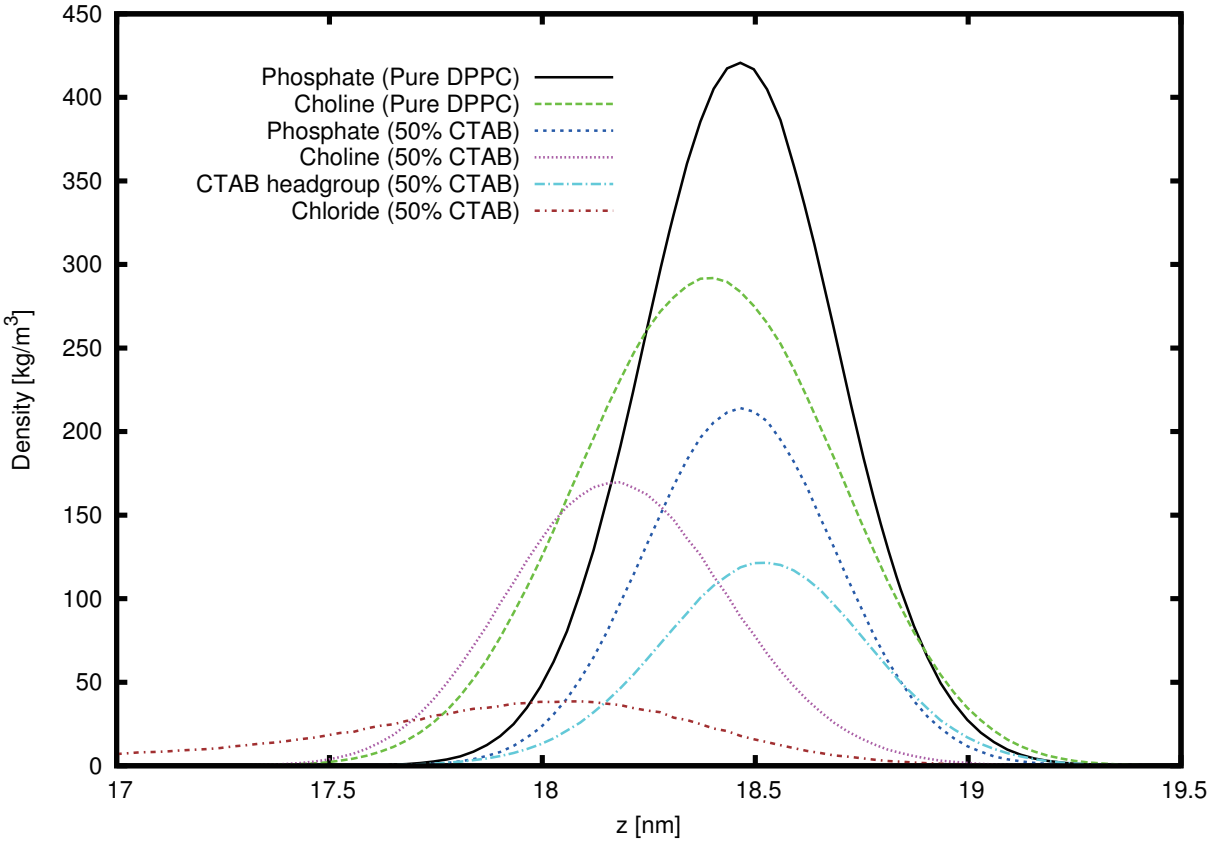

Figure S.2: Density profiles of monolayers with 0% and 50% CTAB molar fraction measured between 100 ns and 1 µs with area per lipid 0.65 nm^2. In the pure DPPC monolayer, the peaks of the density profiles of phosphate and choline have similar z-coordinates, indicating a lateral orientation of the P-N vector in the pure DPPC monolayer. In the mixture, The peaks of the density profiles of DPPC's phosphate groups and CTAB's ammonium groups have similar z-coordinates, which is related to the formation of charge pairs (see the discussion in Radial distribution functions and Electrostatic Interactions of PC and TAB Headgroups), while the peaks for phosphate and choline show a clear separation, which is an evidence of P-N vector reorientation by CTAB (see the discussion in P-N vector orientation section).

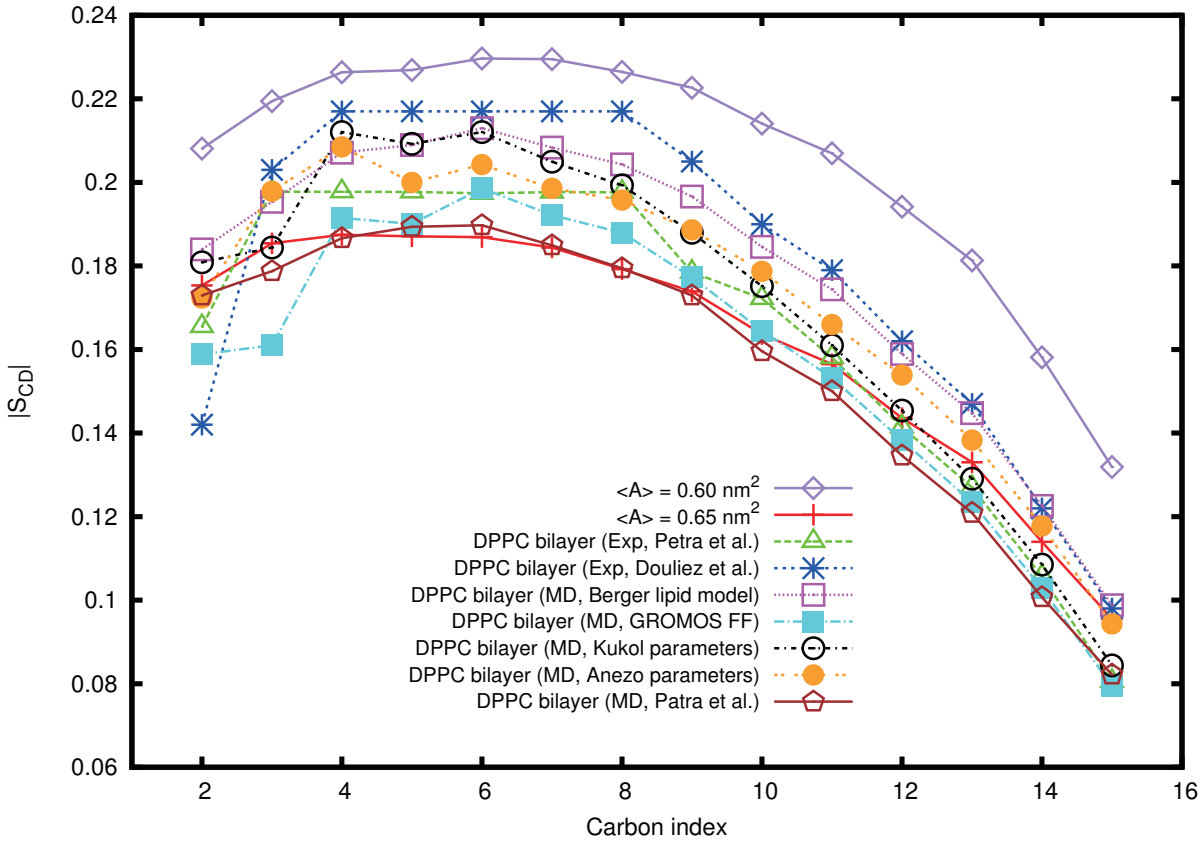

Figure S.3: Chain order parameter $|S_{CD}|$ profiles of the acyl chains in simulated DPPC monolayers (purple, open rhombus for area per lipid = 0.6 nm^2 and red, cross for area per lipid = 0.65 nm^2) and in DPPC bilayers measured experimentally by Petrache et al.[271] (green, open triangle) and by Douliez et al.[272] (blue, star) and in DPPC bilayers simulated by using the Berger lipid model[273] (magenta, open square) and by using the GROMOS 54A7 force field[274, 275] (cyan, filled square) and by using the parameter set by Kukol et al.[274, 276] (black, open circle) and by using the parameter set by Anézo et al.[274, 277] (orange, filled circle) and by Patra et al.[65] (brown, open pentagon). All these simulations and experiments were done at 323 K. All the values for area per lipid used or measured in the experiments and the simulations are between 0.6 nm^2 and 0.65 nm^2. Note Douliez et al.[272] also reported that the $|S_{CD}|$ value for the first hydrocarbon could be challenging to determine accurately.

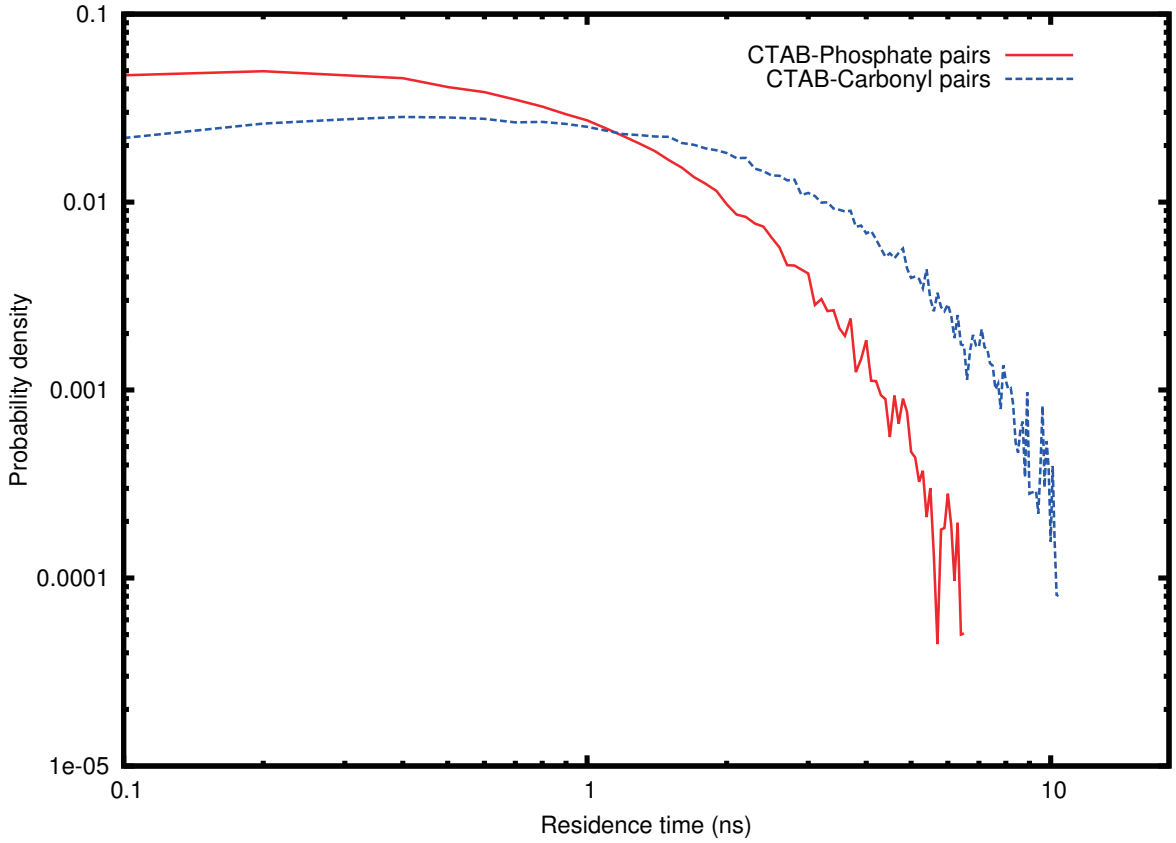

Figure S.4: Residence time of CTAB-phosphate(red, solid line) and CTAB-carbonyl(blue, dashed line) charge pairs. Residence time is defined as the consecutive time spent by CTAB in the 1st coordination shell of the oppositely charged groups of DPPC. The systems has 50% CTAB molar fraction and area per lipid 0.65 nm^2. CTAB spent 65.6% and 83.9% of the total simulated time with phosphate and carbonyl groups respectively in the charge pair state. This indicates CTAB has a limited degree of freedom of moving up or down to minimize the free energy consisiting of the enthalpic contributions from electrostatic interactions between charged groups and entropic contributions from the relative positioning of acyl chains of DPPC and CTAB.

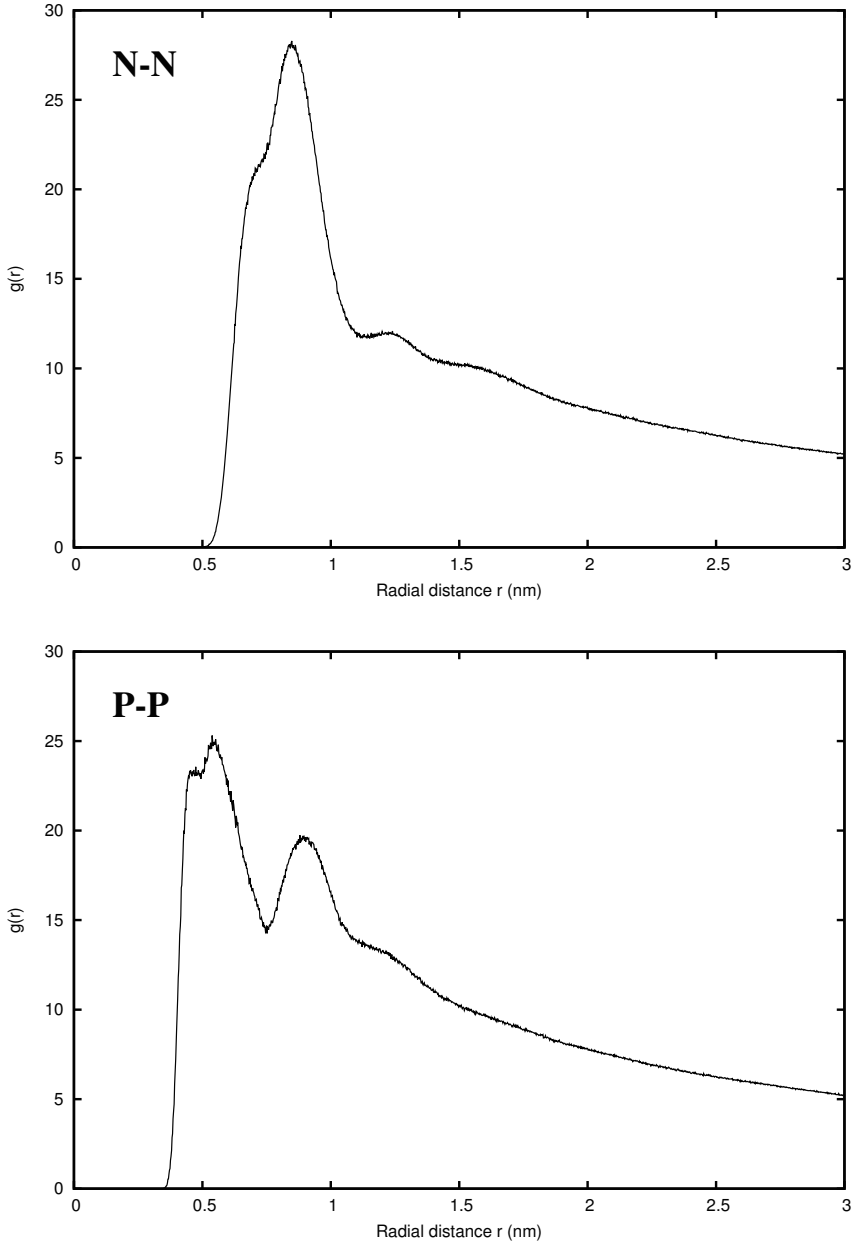

Figure S.5: Radial distribution functions (RDF) $g(r)$ for the two key atoms in the DPPC headgroups in the pure DPPC monolayer: RDFs for N-N and P-P pairs when area per lipid of the monolayer is 0.65 nm^2. Note in 3D RDFs for monolayers, due to the inhomogeneity of the system, RDFs do not converge to 1 at large distance[295]. The x coordinates of the main peak of N-N RDF, the main and the second peaks and the valley of P-P RDF match the calculation for DPPC bilayer by Patra et al[65].

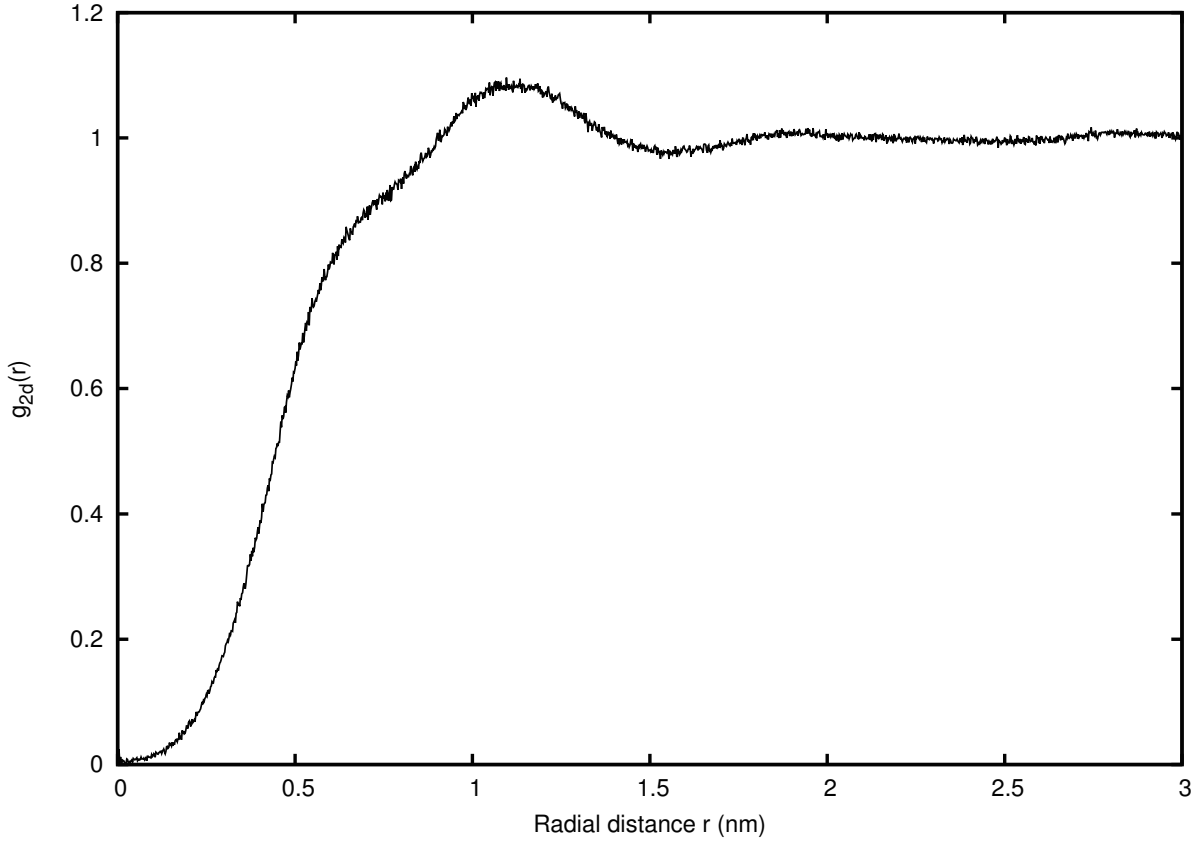

Figure S.6: Lateral radial distribution function (RDF) $g_{2d}(r)$ for the center of mass of the DPPC molecules in the pure DPPC monolayer when area per lipid of the monolayer is 0.65 nm^2. Similar lateral RDF for the center of mass of the DPPC molecules in DPPC bilayer was reported by Patra et al[65]. Compared to the 3D RDFs shown in Figure S.5, the relative soft core of $g(r)$ in the neighborhood of $r = 0$ is caused by the fact that the lipids may be intertwined around each other allowing the x,y coordinates of their center of mass lying close to each other.

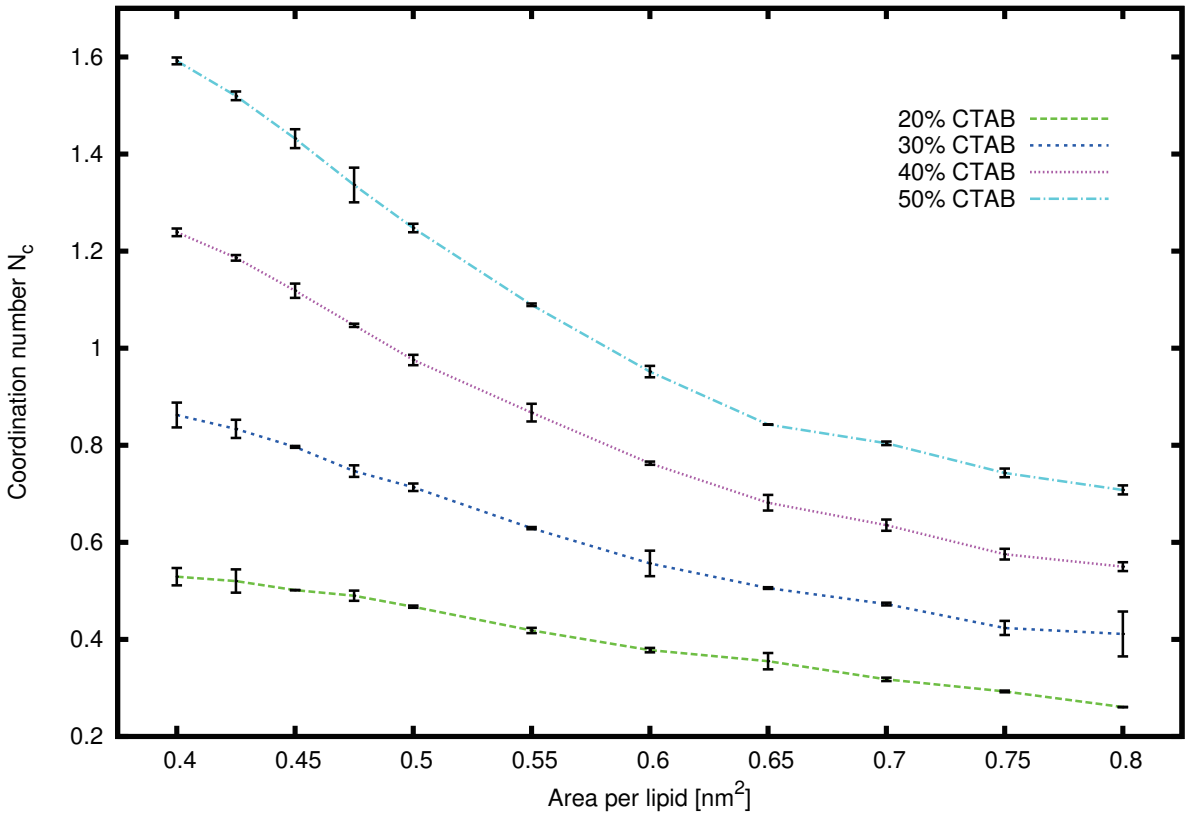

Figure S.7: The coordination number N_C of the phosphorus atom in DPPC with the nitrogen atom in CTAB as a function of area per lipid and CTAB molar fraction. The molar fractions of CTAB in the monolayers are 20% (green, long-dashed), 30% (blue, short-dashed), 40% (magenta, dotted), and 50% (cyan, dotted-dashed). The error bars were calculated from the difference between two leaflets in the same system. The coordinates number doesn't change much as area per lipid varies in the monolayer with 20% CTAB ($0.52 \rightarrow 0.26$), while in the monolayer with 50% CTAB, it changes significantly ($1.59 \rightarrow 0.71$), which has profound effect on the P-N vector orientation of DPPC headgroups.

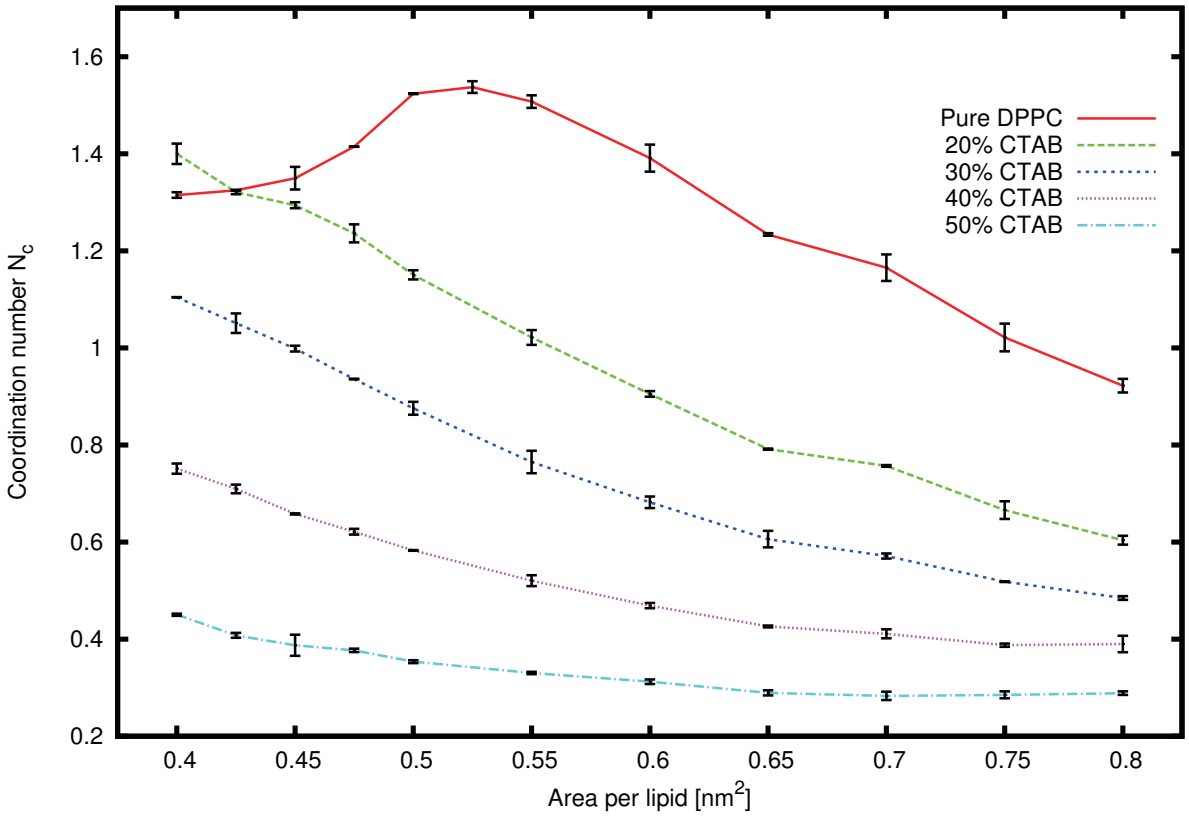

Figure S.8: The coordination number N_C of the phosphorus atom with the nitrogen atom in DPPC (intramolecular pairs excluded) as a function of area per lipid and CTAB molar fraction. The molar fractions of CTAB in the monolayers are 0% (red, solid), 20% (green, long-dashed), 30% (blue, short-dashed), 40% (magenta, dotted), and 50% (cyan, dotted-dashed). The error bars were calculated from the difference between two leaflets in the same system. The formation of intermolecular phosphorus(PC)-nitrogen(PC) pairs was essentially inhibited by the presence of CTAB. Buckling in the pure DPPC monolayer manifests itself again in the form of anomalous decrease in the coordination number with area per lipid below 0.525 nm^2.

Chapter 4

Molecular Dynamics Simulations of mean and Gaussian curvatures of DPPC/CTAB Langmuir Monolayers

4.1 Background

Curvature in biological membranes has posed as a defining feature to characterize various shapes of the cell membrane in recent years[301]. It has been shown that curvature plays a pivotal role in various cellular phenomena, e.g., separation of various membrane components[302] and membrane fusion[111, 303]. Molecular dynamics (MD) simulations in which the coordinates of individual atoms can be precisely recorded in the simulation trajectory provide an ideal framework for evaluating curvature of simulated membranes. The previously challenging task of evaluating curvature for simulated membranes in MD trajectories has been conquered by Pteros[114, 304, 305, 306, 307] which is a fast parallel molecular analysis library for C++ and Python. Dr. Semen Yesylevskyy provided the Pteros source code and the curvature evaluation plugin to the author to accomplish the analysis presented in this chapter. The author contributed to the testing of the Pteros source code and the curvature evaluation plugin.

The concepts of membrane curvatures have been introduced in the membrane elasticity section of the first chapter. The meanings of the mean curvature K_M and Gaussian curvature K_G are summarized in Table 1.1.

In the previous chapter, MD simulations were performed for an in-depth study at the

atomistic level of monolayers consisting of both pure zwitterionic dipalmitoylphosphatidylcholine (DPPC) and a mixture of DPPC and cationic cetyltrimethylammonium bromide (CTAB) at the air/water interface. It was shown that both area per lipid and the CTAB molar fraction have profound effect on if and how the monolayer buckles by showing the representative snapshots of the monolayer. In this chapter, the studies were deepened by evaluating the mean and Gaussian curvatures at the sites of the phosphorus atoms in the DPPC headgroup and the nitrogen atoms in the CTAB headgroup. These atoms are the most heavy ones in the corresponding lipid headgroups, and thus can be used to approximate the surface of the monolayer in contact with water. The distributions of the mean and Gaussian curvatures for monolayer systems with various area per lipid and various CTAB molar fractions were demonstrated and compared. It should be emphasized that for pure DPPC monolayers at very low area per lipid (0.45 nm^2), both a small monolayer with 128 DPPC lipids and a large monolayer with 2048 DPPC lipids were simulated to investigate how the size of the monolayer affects the curvatures and their distributions. We also presented the snapshots of the monolayer systems with only phosphorus and nitrogen atoms displayed and the corresponding normal vectors plotted as arrows to give an intuitive picture of how good our calculations are.

4.2 Methods

We used exactly the same simulation setup, protocols and the resulting trajectories which have been analyzed in the previous chapter.

The method that enables the evaluation of local normal vector, mean and Gaussian curvatures for an arbitrary set of atoms of the membrane was developed under the Pteros framework[114, 304, 305, 306, 307]. The algorithm of the method is based on the analysis of local membrane patches and can be applied to membranes with arbitrary shape and topology. For more details of the algorithm, please refer to Ref. [114].

4.3 Results

Our analysis of the mean and Gaussian curvatures of the pure DPPC and DPPC/CTAB mixture monolayers focuses on three questions. First, we aim to find out how the area per lipid of the monolayer affects the curvatures. Second, we are interested in how the different molar fractions of CTAB affects the curvatures. As discussed in the previous chapter, the area per lipid of the monolayer and the molar fractions of CTAB have essential

effects on the surface tension of the monolayer. When the area per lipid of the monolayer is low combined with low or zero molar fractions of CTAB, the surface tension of the monolayer can reach very low level or even become negative. Low or even negative surface tension could lead to a phenomenon called monolayer collapse in which the monolayer loses its planar structure and develops its geometry into the third dimension. The mean and Gaussian curvatures would experience drastic change in this process. Therefore the mean and Gaussian curvatures can be employed to characterize the monolayer collapse process. Third, we are concerned about if and how the number of DPPC lipids per monolayer for the pure DPPC monolayer introduces any artifacts into the calculated curvatures.

Once the mean and Gaussian curvatures have been obtained, it seems natural to go further into the evaluation of other curvature related quantities. Such quantities, including the spontaneous curvature of the monolayer (see the definition in Eq. 1.39)[88, 250, 308, 309, 310], the bending modulus[108, 309] and the Gaussian curvature modulus[110, 311, 312] have been subjected to extensive theoretical and experimental studies. However our trial tests of fitting the distribution of Gaussian curvatures to get the Gaussian modulus were too sensitive to some parameters we chose. The same issues occurred to the evaluation of the spontaneous curvature too. The fundamental problem here is that local curvature is a microscopic property while the moduli are macroscopic. In order to get the moduli reliably, one must use some macro-observable. Therefore the evaluations of the bending and Gaussian moduli and the spontaneous curvature for the monolayers will be the topics of our future work.

To give an overall sense of how the area per lipid and molar fractions of CTAB affect how monolayers buckle, snapshots of pure DPPC monolayers at a series of area per lipid are shown in Figure 4.2, and snapshots of DPPC/CTAB mixture monolayers with various CTAB molar fractions and area per lipid 0.45 nm^2 which is small are shown in Figure 4.5. The general observation is the pure DPPC monolayer shows severe buckling when the area per lipid is low than a threshold ($\leq$ 0.55 nm^2), and the presence of CTAB essentially alleviates buckling even when the area per lipid is very low (0.45 nm^2).

One of the most intuitive ways to investigate the correctness of the calculation of the mean and Gaussian curvatures is to plot the local normal vectors sitting on the heavy atoms in the DPPC and CTAB headgroups, i.e., phosphorus and nitrogen, for a local patch consisting of the heavy atom itself and its neighboring ones, as shown in Figures 4.1, 4.3 and 4.6. All these figures showed the local normal vectors are correctly calculated and plotted on the corresponding atoms. Figure 4.1 shows the snapshot of the phosphorus atoms and the corresponding local normal vectors in a relatively large pure DPPC monolayer system (2048 lipids per monolayer). Figure 4.3 demonstrates the snapshot of the phosphorus atoms and the corresponding local normal vectors in small pure DPPC monolayer systems

with varying area per lipid (128 lipids per monolayer). And Figure 4.6 demonstrates the snapshot of the phosphorus atoms (DPPC) and the nitrogen atoms (CTAB) in mixture monolayer systems with varying CTAB molar fractions with area per lipid 0.45 nm^2.

Our evaluation of the mean and Gaussian curvatures is only for the hydrophilic headgroups of the monolayer. Theoretically one can also evaluate the curvatures for a set of atoms consisting of the terminal hydrocarbons in the DPPC and CTAB lipid tails, which could generate different values for the curvatures. However, as indicated in our previous work (Figure S.2 in the previous chapter, in the mixture monolayers, the phosphate in DPPC and the choline in CTAB almost have overlapping peaks in their density profile plotted in the z direction, which essentially means the phosphorus atom in DPPC and the nitrogen atom in CTAB are basically located on the same plane or surface. But as DPPC and CTAB are significantly different in term of their lengths, one can not generally expect the terminal hydrocarbons in the DPPC lipid tails and the terminal hydrocarbon in the CTAB lipid tail are located on the same plane, which makes the evaluation of the curvatures for an artificial locally rugged surface composed of the terminal hydrocarbons in the DPPC and CTAB lipid tails together much less useful.

Figure 4.4 gives an insight into the first and the third questions. Pure DPPC monolayers with low area per lipid ($\leq$ 0.55 nm^2) have vastly different distributions for the mean and Gaussian curvatures than the ones with relatively high area per lipid ($\geq$ 0.6 nm^2). Pure DPPC monolayers with relatively high area per lipid ($\geq$ 0.6 nm^2) demonstrates a narrow and symmetrical mean curvature distribution centered on $K_m = 0$ nm^{-1} while the monolayers with low area per lipid ($\leq$ 0.55 nm^2) except for the large monolayer (2048 lipids) show wide and highly negatively skewed distribution. Similar separation into two groups for low area per lipid monolayers and high area per lipid monolayers can also be observed for the distributions of Gaussian curvature. This together with the snapshots in Figures 4.1, 4.2 and 4.3 confirms the buckling and curvatures got essentially reduced by increasing area per lipid for the monolayer. And area per lipid 0.6 nm^2 is an threshold value. When the value of area per lipid increases above it, there is no significant change in the distributions of mean and Gaussian curvatures.

Another fact that can be derived from Figure 4.4 is for monolayers with low area per lipid value, the size of the monolayer, i.e., the number of lipids per monolayer, affects the distributions of mean and Gaussian curvatures to a very large extent. At the same area per lipid 0.45 nm^2, the small monolayer with 128 lipids and the large monolayer with 2048 lipids display distinctively different curvature distributions. The wide and highly negatively skewed distributions only exist for the small monolayer. The large monolayer demonstrates a narrow and symmetrical distribution for mean curvature which is consistently approaching the distribution for mean curvature of the monolayer with higher area

per lipid (0.55 nm^2). This fact indicates for highly buckled monolayers, small simulation box size introduces box sized modulated artifacts into the curvatures. Therefore to obtain the reliable results for highly buckled monolayers, a relatively large simulation box which accommodates a monolayer with adequate number of lipids is required for simulations and the evaluation of curvatures.

Figure 4.7 provides an answer to the second question on how CTAB affects curvatures as well as giving more clues to the third question on whether the number of DPPC lipids per monolayer introduces PBC artifacts. First, the discussion is limited to small monolayers with 128 lipids per monolayer. High molar fraction of CTAB in the monolayer has an effect of reducing the buckling as well as making the curvature distributions for DPPC and CTAB itself narrower and more peaked around zero, which is consistent with the snapshots in Figures 4.5 and 4.6. Monolayers with molar fraction of CTAB no less than 30% show little difference in both mean and Gaussian curvature distributions. Second, the large pure DPPC monolayer with 2048 lipids demonstrated curvature distributions which are very similar to those of the small and less buckled mixture monolayer with 20% CTAB molar fraction. This again signified that a relatively large monolayer is mandatory for the evaluation of curvatures when the buckling is severe.

4.4 Conclusions

In this paper, we analyzed the mean and Gaussian curvatures for the pure DPPC monolayers at various area per lipid and DPPC/CTAB mixture monolayers with various CTAB molar fractions. It is demonstrated that both higher area per lipid and high CTAB molar fraction have the effect of reducing the buckling of the monolayer and making the distributions of the mean and Gaussian curvatures narrower and more peaked around zero. To give an intuitive illustration of how accurate our evaluation of the curvatures is, we also presented the snapshots of the phosphorus atoms (DPPC headgroup) and the nitrogen atoms (CTAB headgroup) in the pure DPPC and mixture monolayers with various area per lipid and various CTAB molar fractions and the corresponding local normal vectors. We also found that for highly buckled monolayers, the size of the monolayer is an essential factor that must be considered if one wants to derive the correct mean and Gaussian curvatures and their distributions. A highly buckled monolayer with too few lipids could introduce severe artifacts into the calculation of curvatures. Therefore a relatively large monolayer consisting of sufficient number of lipids is highly recommended for use if a significant buckling is expected. In practice, determining whether a monolayer is large enough could involve an iterative process in which monolayers with larger and smaller sizes are

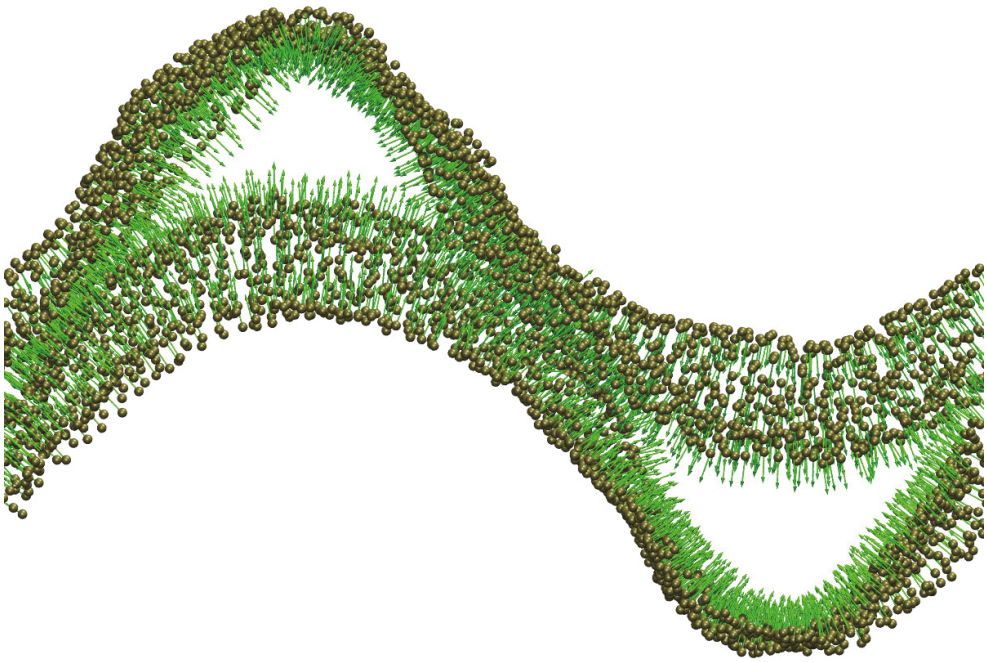

Figure 4.1: The snapshot of the phosphorus atoms (in tan color) representing the headgroups of two highly buckled DPPC monolayers which are decoupled by a sandwiched water slab. Water is disabled for clarity. Each monolayer has 2048 DPPCs. The area per lipid is 0.45 nm^2. The phosphorus atoms can also be regarded as the interface between water and DPPC monolayers. The normal vectors (green arrows) were plotted on each phosphorus atom, pointing towards water. The snapshot was taken for the last frame of the 200 ns trajectory.

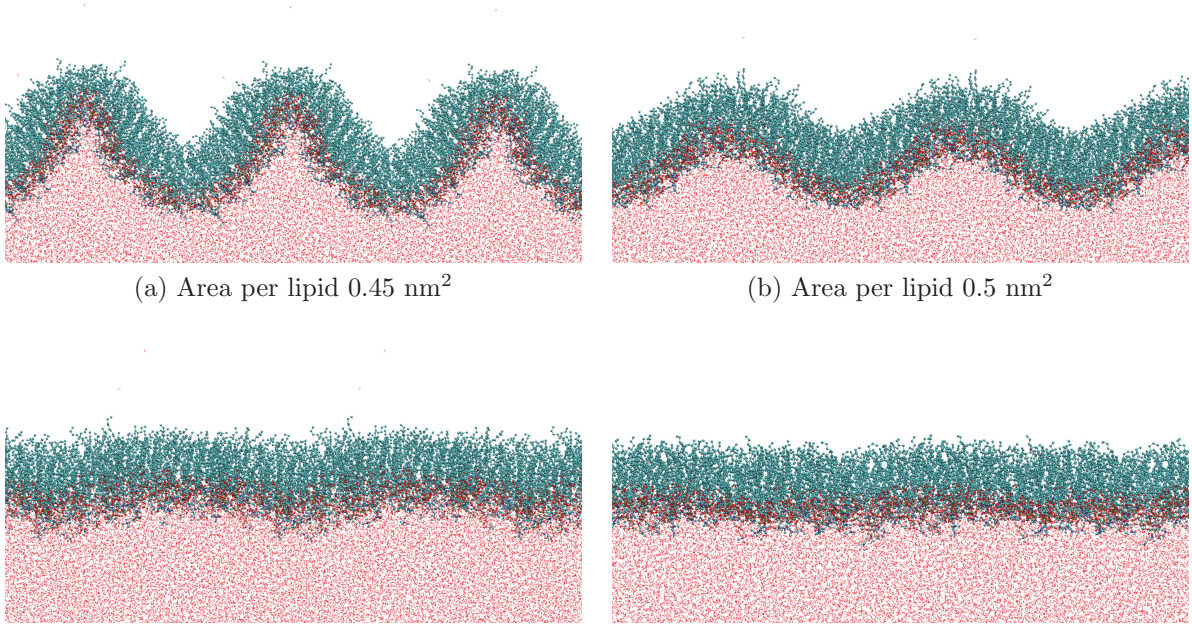

(a) Area per lipid 0.45 nm^2

(b) Area per lipid 0.5 nm^2

(c) Area per lipid 0.55 nm^2

(d) Area per lipid 0.6 nm^2

Figure 4.2: Snapshots of pure DPPC monolayers at the end of the 1 µs trajectories. Water is shown as red dots.

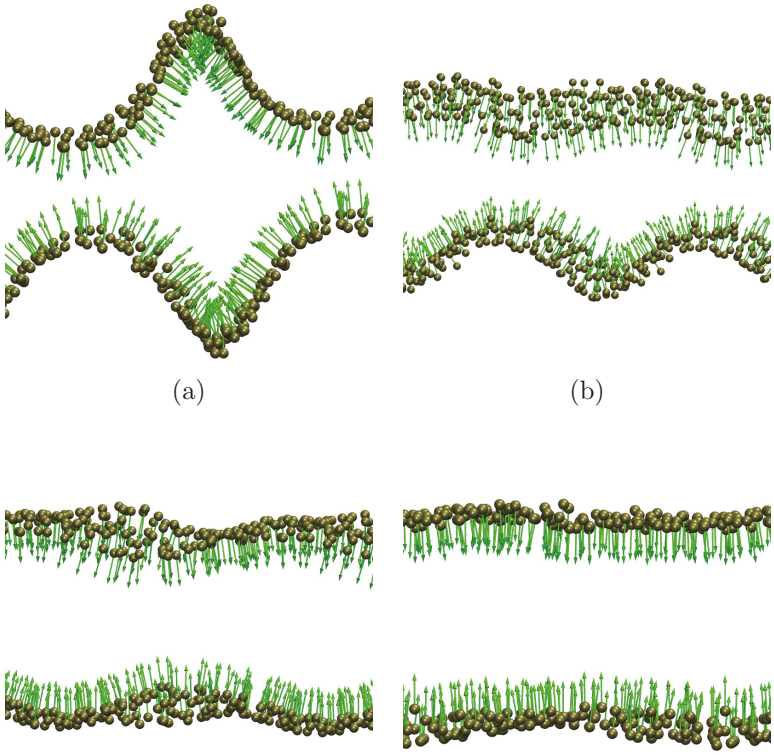

Figure 4.3: Snapshots of the phosphorus atoms (in tan color) and the normal vectors (green arrows) in DPPC monolayers with varying area per lipid values. (a) 0.45 nm^2, (b) 0.5 nm^2, (c) 0.55 nm^2, (d) 0.6 nm^2. Each monolayer has 128 DPPCs. Water is disabled for clarity. Buckling and the associated curvatures decrease significantly as the area per lipid increases. Comparing Figure 4.3a to Figure 4.1, with all other conditions equal, the number of DPPC lipids in the simulation box has essential impact on curvature values, which will be demonstrated in Figure 4.7. The snapshots were taken for the last frames of the 1 µs trajectories.

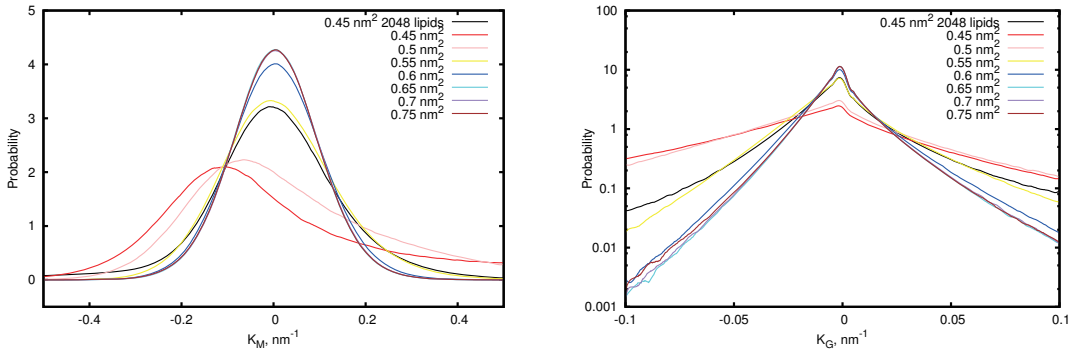

(a) (b)

Figure 4.4: Distributions of mean (a) and Gaussian (b) curvatures for phosphorus atoms during equilibrated parts of trajectories (the last 900 ns with the first 100 ns discarded for equilibration) for pure DPPC monolayers with various area per lipids. The distribution curves were smoothed for clarity. Each monolayer has 128 lipids except for the large monolayer (2048 lipids), corresponding to the snapshots in Figures 4.1, 4.2 and 4.3. The mean curvature distribution curves for area per lipid 0.65 nm^2, 0.7 nm^2, and 0.75 nm^2 are overlapping.

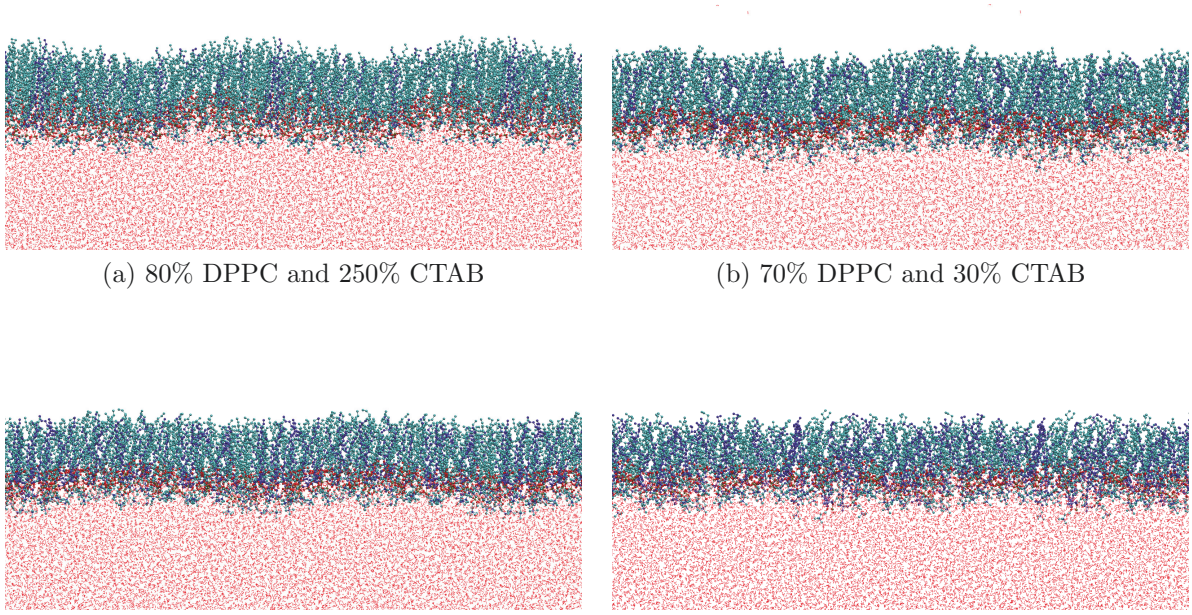

(a) 80% DPPC and 250% CTAB

(b) 70% DPPC and 30% CTAB

(c) 60% DPPC and 40% CTAB

(d) 50% DPPC and 50% CTAB

Figure 4.5: Snapshots of monolayers at the end of the 1 µs trajectories with various CTAB molar fractions and area per lipid 0.45 nm^2. DPPC is shown in cyan, and CTAB in violet. Water is shown as red dots.

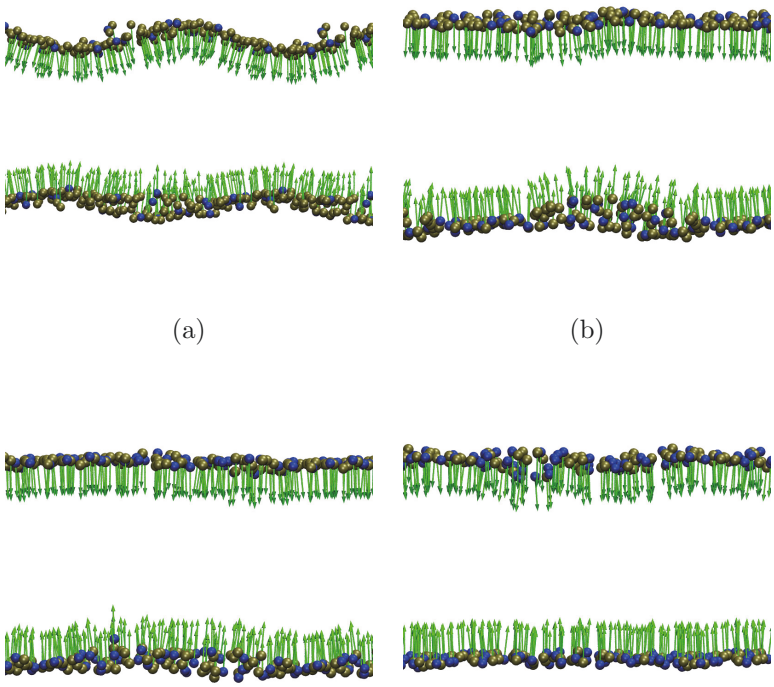

(a) (b)

(c) (d)

Figure 4.6: Snapshots of the phosphorus atoms (in tan color) representing the headgroups of DPPC and the nitrogen atoms (in blue color) representing the headgroups of CTAB in mixture monolayers with various DPPC/CTAB molar fractions. The area per lipid is 0.45 nm^2. (a) 80% DPPC and 20% CTAB, (b) 70% DPPC and 30% CTAB, (c) 60% DPPC and 40% CTAB, (d) 50% DPPC and 50% CTAB. The normal vectors are plotted as green arrows on each phosphorus or nitrogen atom, pointing towards the sandwiched water slab. Each monolayer has 128 lipids. The buckling and the associated curvatures decrease significantly as the molar fraction of CTAB increases. The snapshots were taken for the last frames of the 1 µs trajectories.

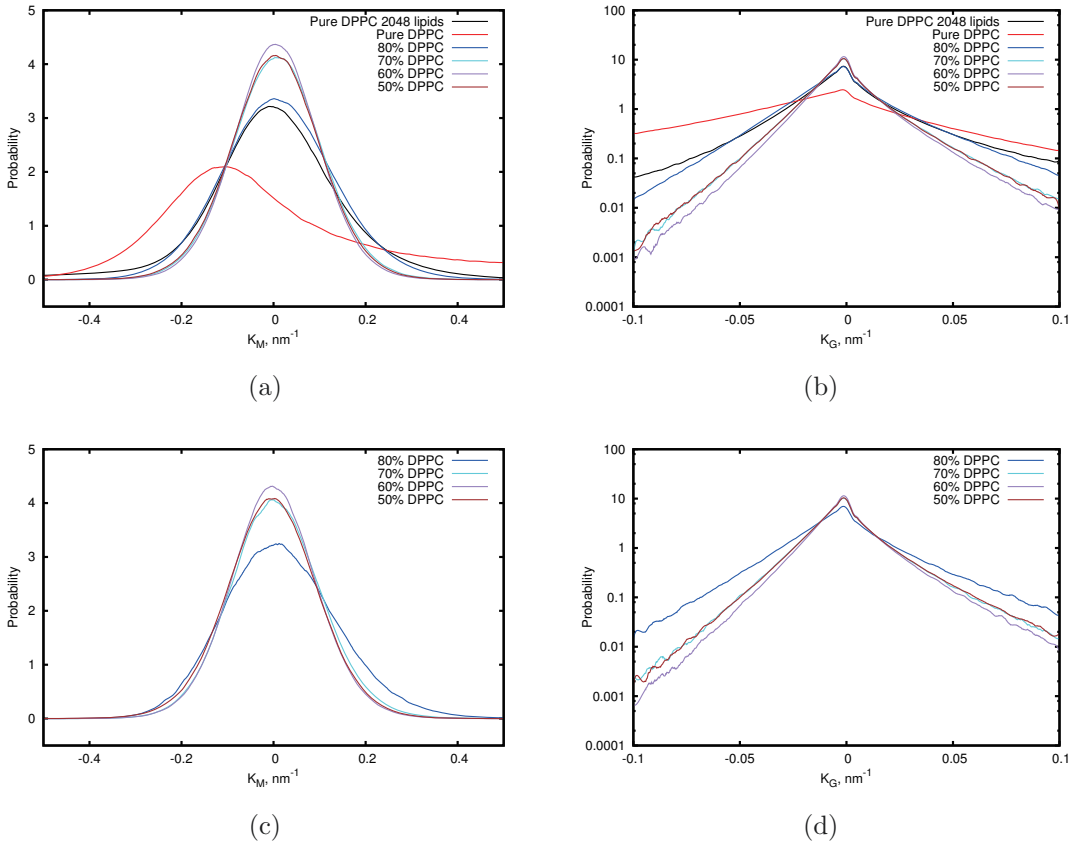

Figure 4.7: Distributions of mean (a) and Gaussian (b) curvatures for DPPC phosphorus atoms and distributions of mean (c) and Gaussian (d) curvatures for CTAB nitrogen atoms during equilibrated parts of trajectories for pure DPPC monolayers (128 lipids per monolayer and 2048 lipids per monolayer) and mixture monolayers with various DPPC/CTAB molar fractions (128 lipids per monolayer). The distribution curves were smoothed for clarity. The area per lipid is 0.45 nm^2. For 128 lipids per monolayer systems, the last 900 ns trajectory was used to collect the statistics with the first 100 ns discarded. For the 2048 lipids per monolayer pure DPPC system, the last 100 ns trajectory was used to collect the statistics with the first 100 ns discarded. The corresponding snapshots can be found in Figures 4.1, 4.3, 4.5 and 4.6.

simulated with the distributions of the curvatures evaluated. A monolayer is large enough for curvature evaluation when the evaluated distributions of the curvatures converge to those obtained by using larger monolayers.

Chapter 5

Subtle Balance of Calcium Ions, Hydrogen Bonding and Charged Lipids is the Key to Daptomycin's Ability to Destabilize Bacterial Membranes

The contents of this chapter were adapted from a manuscript submitted to The Journal of Physical Chemistry Letters

Bin Liu, Mikko Karttunen. Subtle balance of calcium ions, hydrogen bonding and charged lipids is the key to daptomycin's ability to destabilize bacterial membranes. (2016) In review

Daptomycin, trade name Cubicin was approved by the U.S. Food and Drug Administration already in 2003 as an antibiotic to treat infections by Gram-positive pathogens. Daptomycin is special among most antibiotics in that its antibacterial action results from directly acting on membranes[313]. The leading hypothesis is that it enters bacterial membranes, forms channels for ions leading to subsequent depolarization of the membrane and cell death[132]. Whether this happens via oligomerization[145] and disruption or channel formation remains unresolved, although the mechanisms are not mutually exclusive. Importantly, it appears to be quite resistant toward mutations and effective against targets such as methicillin-resistant *S. aureus*[32]. It consists of a total of 13 amino acid residues

including non-standard ones, such as kynurenine (Kyn), ornithine (Orn) and methylglutamic acid (mGlu), (Figure 1.10).

Although it is established that Ca^{2+} ions[36, 141, 142, 143] and anionic phosphatidylglycerol (PG) lipids[144, 145] are required, and that daptomycin acts directly on membranes, the mechanisms for its antimicrobial action remain poorly understood. It is also slightly counterintuitive that anionic daptomycin (net charge about -3) acts on anionic membranes.

Given daptomycin's importance and the success of membrane simulations[314, 315], it is surprising that there appears to be only two prior MD simulation works, by Scott et al. [145] who applied a time-averaged distance-restraining potential to the structural change of daptomycin upon binding to DHPC micelles with and without Ca^{2+}, and by Ho et al. [146] who studied binding to Ca^{2+} in solution.

We parameterized daptomycin using the GROMOS96 53a6 force field[71] at physiological conditions. Figure 1.10 shows the pKa values for the sidechains. Partial charges were evaluated at Mller-Plesset level 2 using the 6-31G(d,p) basis set[179, 181] and GAMESS-US package[176] using Natural Population Analysis (NPA) via the Natural Bond Orbital module[193]. The NPA scheme is not sensitive to the choice of basis set, theory level and geometric structure[191]. The effect of the aqueous environment was taken into account by using the Polarized Continuum Model (PCM)[195, 196]. Parametrization is available at URL www.softsimu.org/downloads.shtml.

Two different membrane setups were used: 1) Single daptomycin in pure DMPC and a bi-component DMPC/DMPG mixture that provides a simple model for bacterial membranes[316], and 2) a tetramer in the bi-component DMPC/DMPG bilayer. The single daptomycin systems were used for free energy calculations. Additionally, using a different setup, 3) we examined daptomycin's micellation and its dependence on calcium ions. The details of the systems are the following: 1) Single daptomycin: DMPC/DMPG bilayer consisting of 64:64 DMPC:DMPG lipids (racemic) and a pure DMPC bilayer (128 lipids) were used. Ca^{2+} concentration was set to 0.1 M. This is higher than the concentration (1.25mM) at which daptomycin reaches its highest antimicrobial potency[134, 317]. This ensures that the absolute number of ions is reasonable. The production simulations were 500 ns each. 2) A daptomycin tetramer was embedded in the upper leaflet of a bilayer consisting 256:256 DMPC:DMPG. About 5 lipids removed upon embedding. The Ca^{2+} concentration was set to 0.1 M and the production simulations were 2 microseconds each. 3) To examine micellation, 64 daptomycin molecules were randomly distributed in the simulation box both with no Ca^{2+} present and at 1:1 molar ratio of $CaCl_2$. The purpose of these 300 ns simulations was to investigate qualitatively if micellation in solution

depends on Ca^{2+}.

The parameterization of Kukol[276] was used for DMPC. The Simple Point Charge (SPC) was used to model water[77]. GROMACS version 4.6[53] was used in all simulations, and the NpT ensemble (constant particle number, pressure & temperature) at T=310K and 1 bar was applied with the V-rescale thermostat[84] and the Parrinello-Rahman barostat[86]. The time step was set to 2 fs. The P-LINCS algorithm[54] was used to constrain all the daptomycin bond lengths and SETTLE[55] for water. The PME algorithm[57] was employed for the long-range Coulomb interactions with a real space cut-off of 1.3 nm. Shifted van der Waals interactions with a cutoff of 1.0 nm were used with shifting starting at 0.9 nm. These protocols have been extensively tested before[62]. Charge neutrality was maintained by adding Cl^- counterions when necessary. The trajectories were visualized by VMD[210].

Free energy umbrella sampling[318, 319] (see SI for details) was employed to calculate the potential of mean force of a single daptomycin as a function of the distance of its center of mass from the midplane for both pure DMPC and the mixed DMPC/DMPG systems, Fig.5.1. Snapshots of representative conformations are shown in Fig.5.2. Figure 5.1 shows that daptomycin has much higher affinity for the mixed PC/PG membranes. At the head group region (phosphorous atoms of the head group) at 2 nm, the free energy difference is around 55 kJ/mol (13 kcal/mol). At the top of the head group region at 2.8 nm, the difference is about 70 kJ/mol (16.7 kcal/mol). Compared to (using the same force field) membrane penetrating peptides such as transportan[320] (about -40 kJ/mol at 2 nm) or the commonly studied transmembrane WALP peptide[321] (about -40 kJ/mol), daptomycin appears to bind more readily to the head group region with values of about -140 kJ/mol for the DMPC/DMPG mixture and about -70 kJ/mol for pure DMPC. Unlike the two, however daptomycin has its free energy minimum at about 2 nm where the phosphorous atoms of the DMPC head group are located. In contrast, transportan and WALP have their free energy minima in the membrane interior. For both pure DMPC and the mixture, the profile is very shallow between about 1.8 and 2.4 nm. Due to the large free energy difference between the pure PC and the mixed PC/PG membrane, and since experimental results support this selectivity, tetramers (below) were studied only with the PC/PG membrane. In unconstrained control simulations daptomycin molecules translocated spontaneously from solution to the free energy minimum.

The free energy profiles in Fig.5.1 are compared to the representative snapshots in Fig.5.2. The most remarkable differences appear at distances of z=2.0 nm and z=2.8 nm. In the case of the PC/PG membrane, daptomycin tries to insert itself to the membrane with the lipid tail first. No preferred orientation or conformation was observed at any distance. In the pure PC membrane, however, daptomycin preferred 100 degrees at z=2.0 and 150

degrees at z=2.8 with respect to the membrane normal albeit with large fluctuations in both cases. The angle is defined in Fig. 1.10. The tail-first insertion mechanism has been proposed based on circular dichroism by Kirkham et al.[322] and its viability is shown here directly by single molecule free energy calculations. Binding is aided by the charged amino acids which interact strongly with the charged PGs. Interestingly, none of this was observed in the case of zwitterionic PC. Instead, daptomycin preferred intramolecular interactions and remained compact. Using differential scanning calorimetry, Jung and Straus6 proposed that daptomycin binds differently to pure PC and bacterial membranes. The current results confirm this and show the detailed origin: upon insertion at z=2.8, daptomycin forms about 7 (10% margin) intramolecular hydrogen bonds when in contact with the pure PC bilayer. This is about double the number compared with the mixed bilayer. The situation is the opposite for daptomycin-lipid hydrogen bonds. It also appears that the PG lipids enable daptomycin to reach deeper inside the bilayer, hydrogen bond and then insert the lipid tail inside the hydrophobic environment. This allows Ca^{2+} ions to bind at the lipid interface; the important (for antibacterial activity[323, 324]) Asp and mGlu residues participate strongly in hydrogen bonding with water in both cases. Inside the membrane, conformational fluctuations are large in both cases as indicated by the free energy penalty in Fig.5.1.

Next, we look at membrane embedded daptomycin tetramers. No constraints were applied and ions were able to diffuse freely. Tetramers were chosen since they have been suggested as intermediate states of water and cation-conducting octamers[36] as well as possible equilibrium structures[325]. Thus, they provide a valid and computationally accessible system to study daptomycin complexes. . Inspection of ion binding shows that Asp-9 is the key to stabilizing the tetramer to remain inside the membrane. Figure 5.3 shows two cases after 2 microseconds of MD simulations each: 1) the tetramer complex remains stably buried inside the membrane (left) and 2) the center of the tetramer slowly moves upwards toward the head group region. We call this case unstable since the tetramer moves upwards. The arrows show the areas where the largest difference occur and the density plots show water density inside the tetramers. Trajectory analysis shows that, most importantly, in the stable case, at least two Ca^{2+} ions remain bound to Asp-9 residues (see Figure 1.10 for numbering) throughout the simulation (not visible since the ions are buried inside the tetramer). In the unstable case, Ca^{2+} binding to Asp-9 was transient. Ca^{2+} ions do also bind to mGlu and Kyn but that is not able to stabilize the tetramer to remain inside the membrane even when binding lasts for 100s of ns.

As the insets show, water density is higher within the tetramer that is buried in the membrane and water is able to cross through it. Although not quantified, but based on inspection of the tetramer structure, penetration and lack of electric potential barriers

implies that the compact tetramer would be able to transport ions as well, thus supporting the leakage and loss of membrane potential hypothesis; umbrella sampling and free energy calculations[326] of potassium ions are beyond the current study but will be performed in the future. Experiments have shown PC/PG embedded daptomycin octamers conduct water and cations[36]. Our simulations support this and show that water enters even the tetrameric state. Although purely a speculation, it may be that water is needed for octamer formation at later stages. In the unstable case with no Ca^{2+} stabilizing Asp-9 (Fig. 5.3, right), the tetramer moves slowly toward the surface and pulls lipids from the lower leaflet with it enhancing curvature. It is possible that that may lead to lipid extraction[139]. This is also supported by the fact that in additional simulations, tetramers moved out of the membrane pulling some lipids with them. Thus, it appears that daptomycin may have more than one pathways to destroy bacterial membranes.

Finally, we briefly investigate daptomycin's behavior in solution. Surprisingly, despite daptomycin's importance and lack of information on how it interacts with and enters membranes, the first direct study of its self-assembly was published only earlier this year by Kirkham et al.[322] using small angle x-ray scattering and cryo-TEM together with other experimental methods for secondary structure. In contrast to the leading hypothesis[145], their results show that daptomycin self-assembles into micelles independently of Ca^{2+} ion concentration at least up to 1:1 molar ratio of $CaCl_2$. Although fully systematic study of micellation is beyond the scope of the present work (larger systems and simulation times of at least tens of microseconds would be necessary), we performed simulations both in the presence and absence of $CaCl_2$ to have a qualitative picture of the situation (only Cl^- counterions to preserve charge neutrality were present). Figure 5.4 shows snapshots after 300 ns both with Ca^{2+} and without Ca^{2+}. The observed independence of micellation from Ca^{2+} ions is significant since it challenges the suggestion that Ca^{2+} ions are required for micellation.

In conclusion, we have demonstrated daptomycin's affinity for model bacterial PC/PG membranes and detailed the origin of the difference in binding to PC membranes. We have, to our knowledge, for the first time, shown in detail how calcium ions stabilize the tetramer complex, in particular by binding to at least two Asp-9 residues for long times - binding was observed over a microsecond. It was also observed that binding to other residues is not able to stabilize the complex to stay within the membrane. We also showed that hydrogen bonding, although subtle, is important for binding to membranes. This, together with transient binding to the charged PG lipids, stabilizes the complex and provides a narrow channel through the membrane.

Several interesting questions remain including daptomycin's precise insertion mechanism into the membrane: The free energy profile in Fig. 5.1 suggests that individual

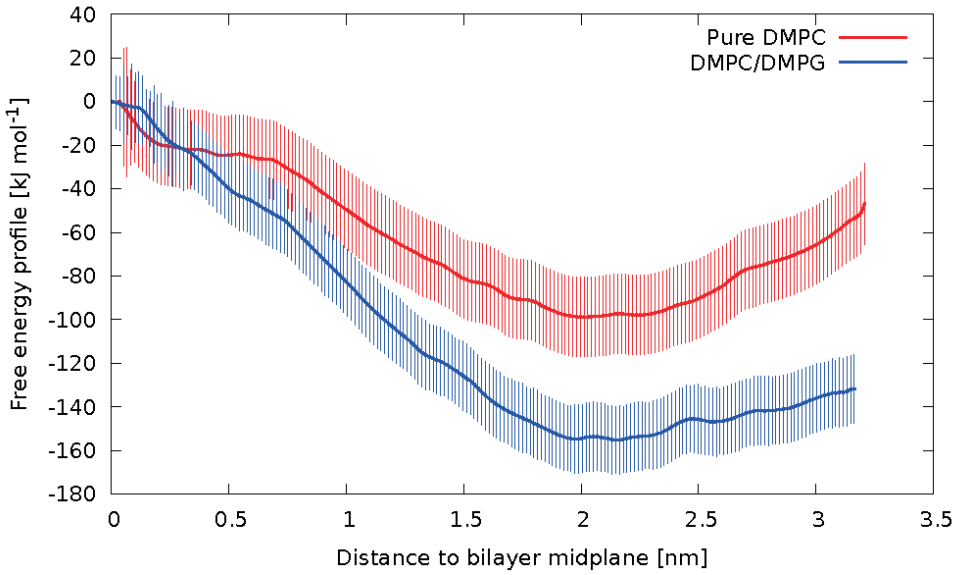

Figure 5.1: Free energy of insertion for a single daptomycin. The distance 2 nm corresponds to the bilayer head group region. Snapshots of representative conformations are shown in Fig.5.2.

molecules are not likely to enter the membrane interior. One of the immediate questions is: does aggregation occur on the membrane surface or in solution? Several scenarios have been suggested[143, 144, 145] and it is likely that multiple pathways for membrane entry exist. Based on the current simulations and the scattering experiments of Kirkham et al.[322], aggregation is independent of calcium (or other ion) concentration. The simulations here show that individual daptomycins seem to be able to insert the lipid tail first (Figure 1.10) into the membrane via assistance from hydrogen bonding, and ions. How complexes form remains, however, an open question. The above results imply that calcium becomes significant in one or more of the main stages: binding, membrane entry, stabilization in the membrane but not in aggregate formation in solution.

Supporting Information

Details of the free energy calculation:

Umbrella sampling[318, 319] was used to calculate the potential of mean force acting on the center of mass of a single daptomycin molecule as a function of distance from the bilayer midplane (z=0). The pure DMPC bilayer that was used in the umbrella sampling calculation had 128 DMPC lipids. The DMPC/DMPG bilayer contained 64 DMPC and

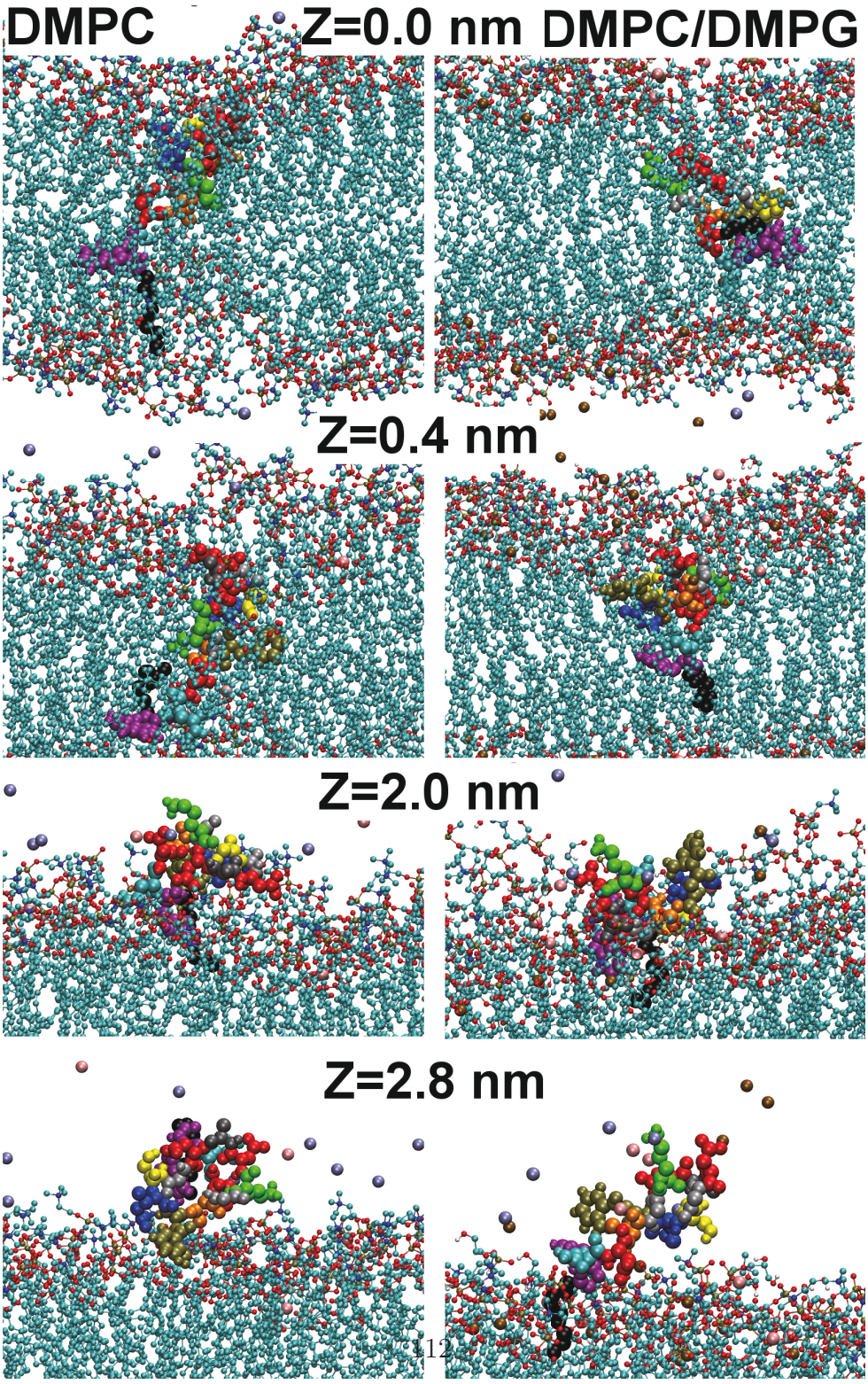

Figure 5.2: Representative conformations from the umbrella sampling simulations of the pure DMPC and the mixed system. The distance (z), corresponds to Fig. 5.1. The color scheme for the peptide is the same as in Figure 1.10.

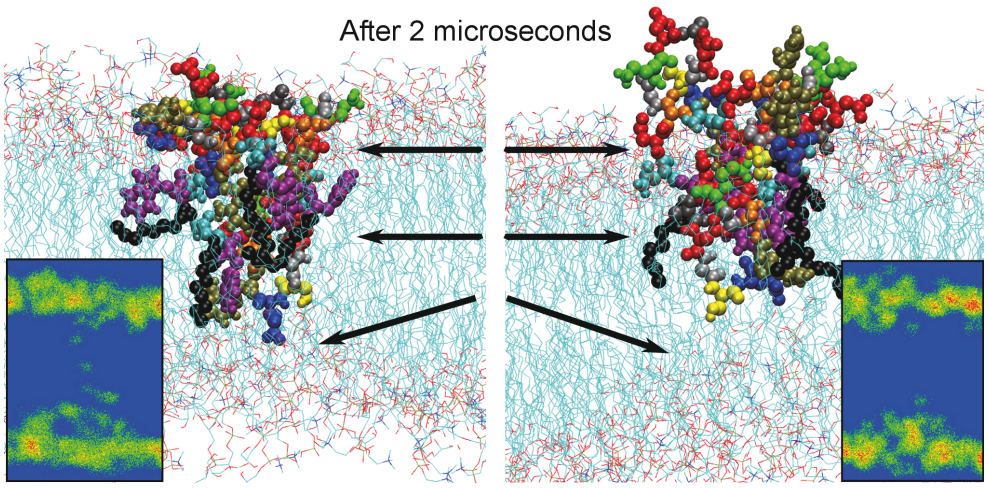

Figure 5.3: Left: Tetramer in a stable position in the PC/PG membrane. It causes only a small perturbation on the opposing leaflet. Stability results from two or more Ca^{2+} ions being bound to the Asp-9 residues. Right: In the absence of Ca^{2+}-Asp-9 binding the tetramer slowly moves out of the membrane and pulls lipids from the opposing side with it. Insets: water density inside the tetramer in the two cases (blue is low, red is high). The color scheme for daptomycin is given in Figure 1.10.

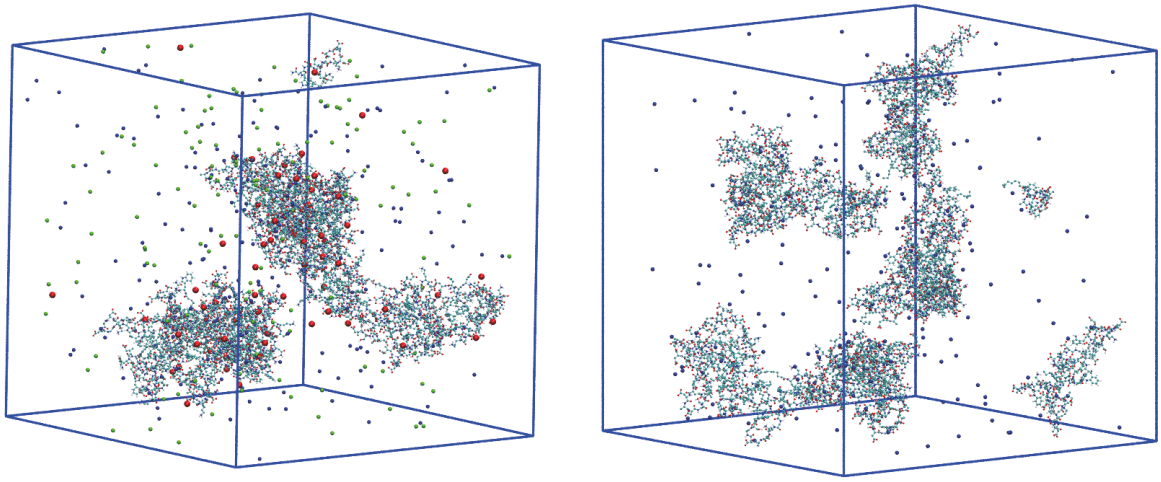

(a) (b)

Figure 5.4: Micellation in the presence (left) and absence (right) of Ca^{2+} ions after 300 ns. The system Ca^{2+} present evolves fast but reaching equilibrium would require (minimally) tens of microseconds.

64 DMPG lipids. The starting configurations for the umbrella sampling calculations were generated from pulling a single daptomycin with its center of mass initially 3.3 nm (in solution) from the bilayer midplane in the z-direction towards the bilayer midplane. The center of mass spacing in the z-direction was selected to be 0.1 nm. This generated 37 initial daptomycin configurations for umbrella sampling windows. Each daptomycin configuration was then constrained at its respective center of mass z-coordinate by a harmonic potential with a force constant of 1000 kJ mol^{-1} nm^{-2}; the constraint acted on the center of mass of the daptomycin molecule and the rest of the molecule was free to move and explore its conformations. For each daptomycin configuration, 100 ns simulations were conducted. The first 50 ns of each simulation was used as the equilibration stage, and the remaining 50 ns to calculate the potential of mean force. We used the weighted histogram analysis method[319] (WHAM) to combine the results from all of the sampling windows in order to calculate the potential of mean force. Error bars were estimated by the bootstrapping method[319]. In addition to the umbrella sampling simulations, control simulations for a single daptomycin without constraints were performed and the molecule moved spontaneously from solution to the free energy minimum.

Details of the setup of daptomycin tetramer systems:

All tetramer simulations were full dynamic simulations without any applied constraints (as was done in umbrella sampling for single daptomycin molecules). It is well known, that computing the free energy profile for complex consisting of several molecules is very challenging due to problems in determining appropriate reaction coordinates. Some current issues regarding calculations of free energy have been recently discussed by Hansen and van Gunsteren[327]. The initial configurations of the daptomycin tetramers were obtained by using the following procedure. The four daptomycin monomers in a tetramer initially had the same orientation and conformation, and differed only in the xy-coordinates of the center of mass. The xy-coordinates of the centers of masses of the four monomers were placed in the corners of a square of 0.8 nm in length. The z-coordinates of the centers of masses were the same. We then applied a random angle to rotate each of the four daptomycin monomers around the z-axis fixed on each monomers respective center of mass. This procedure was repeated to obtain the initial tetramer configurations.

In each of the tetramer simulations, a daptomycin tetramer was placed inside the bilayer by removing a few (5) lipid molecules from the bilayer. The initial z-coordinate of each tetramers center of mass was set to 0.5 nm above the bilayer midplane. After the placement, the system was first relaxed to remove any steric constraints and then left to evolve over time. The tetramer simulations were full dynamic simulations without any positional constraints: the tetramers were free to move out if/when they became unstable. Ions were added to the simulation box by randomly replacing water molecules. 100 Ca^{2+} ions were

added to the simulation box to ensure that the observed interactions between ions, lipids and residues are not rare events. Na^+ ions were added accordingly as the counterions to balance the negative charges of PG lipids and daptomycin molecules, and Cl^- ions were added to balance the charges of Ca^{2+} ions.

We performed simulations for six independent daptomycin tetramer systems. The final configurations for two of the six simulated tetramer systems are shown in Figure 5.3 in the main text. In the remaining four simulated tetramer systems, one displayed similar behavior as the stable tetramer system shown in Figure 5.3, while the remaining three tetramers moved out of the membrane pulling lipids with them: as discussed in the main text, in the stable cases Ca^{2+} ions spontaneously bound to at least of two of the Asp-9 residues for extended times (length of full simulation). This binding distinguished the stable (i.e., remaining stably inside the membrane) from the unstable (moving out of the membrane) cases. In each of unstable cases, the three tetramers remained partially embedded in the lipid bilayer, and all the four daptomycin molecules remained bound to the lipid bilayer for a few hundreds of nanoseconds. Additional snapshots of binding and of an unstable tetramer moving out of the membrane are provided in Figure 5.6.

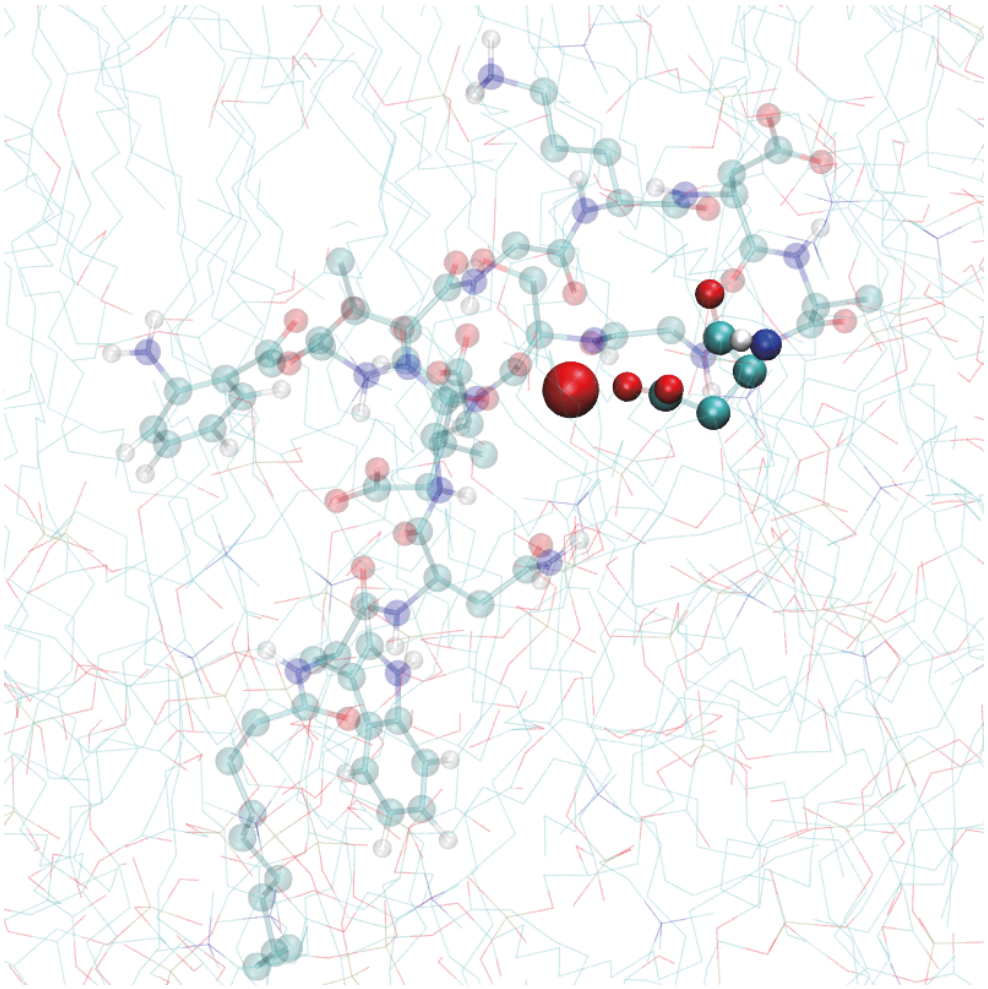

Figure 5.5: Persistent binding between a Ca^{2+} ion and an Asp-9 residue of one of the four daptomycin molecules in the stable tetramer. All the other residues are shown as semi-transparent. The other three daptomycin molecules and the other Ca^{2+} ions were not shown for clarity. Binding was continuous through the whole 2 microsecond trajectory. Asp-9s COO^- functional group attracts the Ca^{2+} ion.

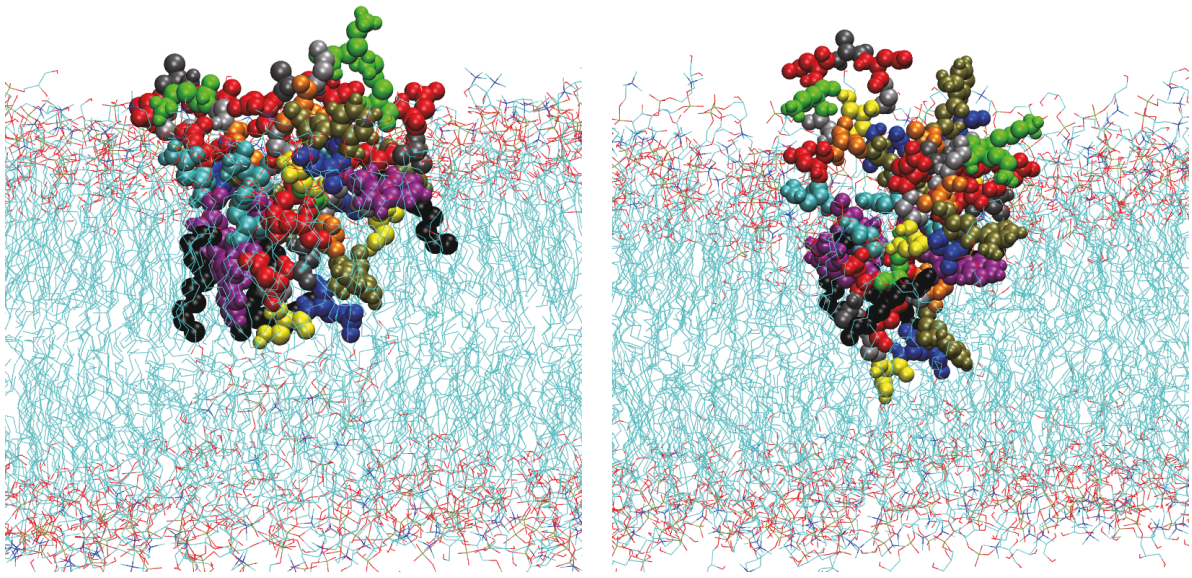

(a) (b)

Figure 5.6: Snapshots of a tetramer moving out of the membrane. Left: after 500 ns. Right: after 1 microsecond. The color scheme for daptomycin is given in Fig. 1.10.

Chapter 6

Summary and Future Work

6.1 Summary

Lipid structures, such as monolayers/bilayers and micelles/liposomes, are gaining their importance as promising packaging material for drug delivery purpose. The studies of lipid bilayers, as the underlying structure of cell membranes, also provides insight into the understanding of the action mode of drugs, paving ways for the development of the next generation of drugs.

In the DPPC/CTAB monolayer project, we performed MD simulations of the pure DPPC and DPPC/CTAB mixture Langmuir monolayers at a series of area per lipid at constant temperature 323 K. We investigated how the composition of the DPPC/CTAB monolayers affects their structural and electrostatic properties in the liquid-expanded phase. The most significant conclusion was the presence of the CTAB molecules has a condensation effect and stabilization restoring the monolayers' flat structure which has an electrostatic origin. For the pure DPPC monolayer, severe buckling was observed for areas per lipid smaller than 0.55 nm^2. Such buckling has a profound effect on monolayers' properties, e.g., thickness, hydrogen bonding, chain order parameter etc. However the buckling diminishes quickly even at 20% CTAB molar fraction in the mixture monolayers for the same range of areas per lipid. The condensation effect leads to stable flat structures for the DPPC/CTAB monolayers under high surface pressure which could correspond to even negative surface tension. The analysis of P-N vector orientation provides an interpretation of the condensation effect of the CTAB molecules. In the pure DPPC monolayer, the P-N vector aligns almost parallel to the air-water interface, which leads to larger projected area onto the air-water interface occupied by the PC headgroup. The presence of CTAB molecules reorients

the P-N vectors of their neighboring DPPC molecules into more vertical directions, which significantly reduces the projected area onto the air-water interface occupied by the PC headgroup.

We also showed that the local normal and the distributions of the mean and Gaussian curvatures for both flat and highly buckled monolayers can be accurately evaluated by using the Pteros framework and the curvature evaluation plugin. However, caveats exist for the evaluation of the distributions of the curvatures when the buckling is severe. A highly buckled monolayer with too few lipids in the simulation box could introduce severe artifacts into the calculation of curvatures. This has been demonstrated by our calculations of the distributions of the mean and Gaussian curvatures for highly buckled pure DPPC monolayers with 256 and 4096 lipids at the same area per lipid. If the artifacts were absent, the small pure DPPC monolayer with 256 lipids and the large one with 4096 lipids should give the same distributions for the mean and Gaussian curvatures. However, while the distributions for the curvatures obtained by using the large monolayer show reasonable symmetry with respect to zero, the distributions obtained by using the small monolayer is highly skewed. Therefore a large monolayer consisting of sufficient number of lipids is highly recommended for use if a significant buckling is expected.

In the daptomycin project, we constructed the first high-quality molecular modeling of the antibiotic molecule, daptomycin, by using the GROMOS force field and partial charges set obtained by the NPA scheme. We then used the modeling for daptomycin to study the mechanism for its antimicrobial action. More specifically, we simulated two of the several stages in the latest version of the proposed mechanism for daptomycin's antimicrobial action.

First, we simulated the spontaneous binding of a single daptomycin to the model PC/PG bacterial membrane surface. We simulated this stage in two ways. We conducted positionally constrained simulations to evaluate the free energy profile of a single daptomycin's binding process to the DMPC/DMPG bilayer. As a reference, we applied the same protocal to evaluate the free energy profile of a single daptomycin's binding to the pure DMPC bilayer. The free energy profiles tell that a single daptomycin has much higher affinity to the mixture PC/PG bilayer than to the pure DMPC bilayer, and the free energy minimum for binding to the PC/PG bilayer is located near the bilayer surface. The free energy profiles were then confirmed by unconstrained control simulations in which a daptomycin molecule translocated spontaneously to the free energy minimum no matter where we initially placed it, such as in the solution or deeply embedded in the PC/PG bilayer. The full dynamics simulation of a free daptomycin's spontaneous binding to the surface of the PC/PG bilayer also revealed that the occurence of persistent hydrogen bonding between daptomycin and the PC/PG phosphate groups plays a vital role in the

binding process.

Second, we performed full dynamics simulations of daptomycin tetramers which were artificially embedded in the model PC/PG bilayer. We were unable to directly simulate the spontaneous oligomerization of daptomycin molecules inside the model PC/PG bilayer due to an intractable time scale issue. Yet our simulations of the daptomycin tetramer state gave an insight into how the tetramers interact with the model PC/PG bilayer. In sharp contrast with the single daptomycin case, daptomycin tetramers did not necessarily translocate to the free energy minimum in a short period, at least not at the microsecond time scale. This means daptomycin tetramers can be stably embedded in the model PC/PG bilayer for a long time. This agrees with the experimental results that tetramers are a plausible and likely intermediate towards octamers and they do exist in PC/PG membranes[36]. We then found the key factor to determine whether a tetramer is stable is the persistent binding between the aspartic acid residues of daptomycin to Ca^{2+} ions.

6.2 Future work

For both projects presented in this thesis, further work is needed to complement the existing studies.

The formation and evolution of membrane curvatures is a highly complex dynamical process. Our existing work is confined to the description of the pure geometric properties of this process, i.e., the mean and Gaussian curvatures and the normal vector. The studies of the dynamical properties of this process will lead to the evaluation of dynamical quantities, such as the spontaneous curvature, and the moduli associated with the mean and Gaussian curvatures. For the moment, the evaluation of the spontaneous curvature and the curvature moduli still poses as a great challenge for us. Taking the Gaussian modulus as an example. The Gaussian curvature modulus is rather tricky to compute despite its simple definition. To our best knowledge, the only reliable way of computing it in MD is the method of Hu et al.[110]. Some tests with fitting the distribution of Gaussian curvature in order to get the Gaussian modulus have been performed. However the results depend on parameters used and are not reliable. The fundamental problem here is that local curvature is a microscopic property while the bending modulus is macroscopic. In order to get the bending modulus reliably, some macro-observables, such as vesicle closure time in the method of Hu et al. are needed. The same is true for the spontaneous curvature. We still have a long way to go before the reliable dynamical quantities can be obtained.

There are a number of future directions for the daptomycin project.

First, applying the same simulation and analysis methodology to the daptomycin octamer state as we did to the tetramer state will hopefully provide a more comprehensive picture of how daptomycin multimers interact with the model PC/PG bacterial membrane. A larger and more persistent pore through the octamer is expected to develop and function as the water and ion channel. Again, we will closely observe how the (persistent) binding of Ca^{2+} ions to specific amino acid residues of daptomycin affects the stability of the daptomycin octamer state. We also expect the daptomycin octamer will disrupt the model PC/PG bacterial membrane even further and may induce significant curvatures. However, the direct calculation of the curvatures of the disrupted membrane is still challenging as our current approach to evaluate the curvatures requires the membrane to be continuous.

Second, more simulations and analysis are needed to understand daptomycin's spontaneous oligomerization/micellation in solution. Significantly longer trajectories are required to equilibrate the daptomycin oligomers in solution. After the equilibrium has been reached, the distribution of the daptomycin oligomer state, i.e., whether they are tetramers, pentamers, etc., and their relative abundance weighted by time, can be obtained. We are also interested in the conformation and orientation of the daptomycin monomers constituting the oligomer states.

Third, if we do substitution of specific amino acid residues in daptomycin, such as the important Asp and mGlu residues for antimicrobial activity, and perform all the simulational procedures and analysis to the new chemical compounds, we could lead to better understanding of daptomycin's interactions with the bacterial membrane, and hence shed light on the understanding of daptomycin's antimicrobial activity and even facilitating the development of the next generation of antibiotics. Obviously this stage will involve huge commitment of human time and computational resources. But this is the ultimate goal of the studies in daptomycin.

Copyright Permission

The following papers have been reproduced with permission as Chapters 2 and 3:

1. Bin Liu, Jirasak Wong-Ekkabut, Mikko Karttunen (2015) "Molecular Dynamics Simulation of Surfactant Monolayers", Chapter 11 in Computational Methods for Complex Liquid-Fluid Interfaces (page 249-264), Edited by Mohammad Taeibi Rahni, Mohsen Karbaschi, and Reinhard Miller Copyright (2015) CRC Press of Taylor and Francis Group LLC Books

2. Bin Liu, Matthew Hoopes, Mikko Karttunen (2014) Molecular Dynamics Simulations of DPPC/CTAB Monolayers at the Air/Water Interface. The Journal of Physical Chemistry B 118, 11723-11737 Copyright (2014) American Chemical Society.

In these publications, the author has been involved in planning the research projects, constructing the model systems, running massive scale computer simulations, and performing the analysis to interpret the results. The author has also contributed essentially to the writing of the drafts for the publications.

References

[1] Shelley McGuire. World Cancer Report 2014. Geneva, Switzerland: World Health Organization, International Agency for Research on Cancer, WHO Press, 2015. *Adv. Nutr.*, 7(2):418–9, 2016.

[2] Y. Luo and G. D. Prestwich. Cancer-targeted polymeric drugs. *Current Cancer Drug Targets*, 2(3):209–226, 2002.

[3] Li Di, Edward H. Kerns, and Guy T. Carter. Drug-like property concepts in pharmaceutical design. *Current Pharmaceutical Design*, 15(19):2184–2194, 2009.

[4] Hywel Williams, Natalie Trevaskis, Susan Charman, Ravi Shanker, William Charman, Colin Pouton, and Christopher Porter. Strategies to address low drug solubility in discovery and development. *Pharmacol. Rev.*, 65(1):315–499, 2013.

[5] Aditi M. Jhaveri and Vladimir P. Torchilin. Multifunctional polymeric micelles for delivery of drugs and siRNA. *Front. Pharmacol.*, 5(April):1–26, 2014.

[6] Magid H. Amer. Gene therapy for cancer: present status and future perspective. *Mol. Cell. Ther.*, 2:27, 2014.

[7] P. G. Higgs. RNA secondary structure: physical and computational aspects. *Q. Rev. Biophys.*, 33(3):199–253, 2000.

[8] Cecilia Guerrier-Takada, Katheleen Gardiner, Terry Marsh, Norman Pace, and Sidney Altman. The RNA moiety of ribonuclease P is the catalytic subunit of the enzyme. *Cell*, 35:849–857, 1983.

[9] Andrew Fire, SiQun Xu, Mary K. Montgomery, Steven A. Kostas, Samuel E. Driver, and Craig C. Mello. Potent and specific genetic interference by double-stranded RNA in Caenorhabditis elegans. *Nature*, 391(6669):806–811, 1998.

[10] John C. Burnett and John J. Rossi. RNA-based therapeutics: Current progress and future prospects. *Chem. Biol.*, 19(1):60–71, 2012.

[11] Xi Qiu Liu, Chun Yang Sun, Xian Zhu Yang, and Jun Wang. Polymeric-micelle-based nanomedicine for siRNA delivery. *Part. Part. Syst. Charact.*, 30(3):211–228, 2013.

[12] Gemma Navarro, Sean Essex, and Vladimir P. Torchilin. The Non-viral Approach for siRNA Delivery in Cancer Treatment: A Special Focus on Micelles and Liposomes. In Volker A. Erdmann and Jan Barciszewski, editors, *DNA RNA Nanobiotechnologies Med. Diagnosis Treat. Dis.*, pages 241–261. Springer Berlin Heidelberg, Berlin, Heidelberg, 2013.

[13] Ying Lu and Kinam Park. Polymeric micelles and alternative nanonized delivery vehicles for poorly soluble drugs. *Int. J. Pharm.*, 453(1):198–214, 2013.

[14] Klaus Strebhardt and Axel Ullrich. Paul Ehrlich ' s magic bullet concept : 100 years of progress. *Nat. Rev. Cancer*, 8:473–480, 2008.

[15] Sonke Svenson. Dendrimers as versatile platform in drug delivery applications. *Eur. J. Pharm. Biopharm.*, 71(3):445–462, 2009.

[16] Erem Bilensoy. Cationic nanoparticles for cancer therapy. *Expert Opin. Drug Deliv.*, 7(7):795–809, 2010.

[17] Hak Soo Choi, Wenhao Liu, Preeti Misra, Eiichi Tanaka, John P. Zimmer, Binil Itty Ipe, Moungi G. Bawendi, and John V. Frangioni. Renal clearance of nanoparticles. *Nat. Biotechnol.*, 25(10):1165–1170, 2007.

[18] Vladimir Torchilin. Tumor delivery of macromolecular drugs based on the EPR effect. *Adv. Drug Deliv. Rev.*, 63(3):131–135, 2011.

[19] Vladimir Torchilin. siRNA delivery: from basics to therapeutic applications. *Front. Biosci.*, 18(1):58, 2013.

[20] Barney L. Bales, Mohammed Benrraou, and Raoul Zana. Krafft temperature and micelle ionization of aqueous solutions of cesium dodecyl sulfate. *J. Phys. Chem. B*, 106(35):9033–9035, 2002.

[21] Xian-zhu Yang, Shuang Dou, Yu-cai Wang, Hong-yan Long, Meng-hua Xiong, Cheng-qiong Mao, Yan-Dan Yao, and Jun Wang. Single-Step Assembly of Cationic

LipidPolymer Hybrid Nanoparticles for Systemic Delivery of siRNA. *ACS Nano*, 6(6):4955–4965, 2012.

[22] C. Wan, T. M. Allen, and P. R. Cullis. Lipid nanoparticle delivery systems for siRNA-based therapeutics. *Drug Deliv. Transl. Res.*, 4(1):74–83, 2014.

[23] Cong-fei Xu and Jun Wang. Delivery systems for siRNA drug development in cancer therapy. *Asian J. Pharm. Sci.*, 10(1):1–12, 2015.

[24] Shu Wen Tong, Bai Xiang, Da Wen Dong, and Xian Rong Qi. Enhanced antitumor efficacy and decreased toxicity by self-associated docetaxel in phospholipid-based micelles. *Int. J. Pharm.*, 434(1-2):413–419, 2012.

[25] Jinqiang Wang, Weiwei Mao, Lye Lin Lock, Jianbin Tang, Meihua Sui, Weilin Sun, Honggang Cui, Dong Xu, and Youqing Shen. The Role of Micelle Size in Tumor Accumulation. *ACS Nano*, 9(7):7195–7206, 2015.

[26] Rupa R. Sawant and Vladimir P. Torchilin. Multifunctionality of lipid-core micelles for drug delivery and tumour targeting. *Mol. Membr. Biol.*, 27(October):232–246, 2010.

[27] G. Salzano, R. Riehle, G. Navarro, F. Perche, G. De Rosa, and V. P. Torchilin. Polymeric micelles containing reversibly phospholipid-modified anti-survivin siRNA: A promising strategy to overcome drug resistance in cancer. *Cancer Lett.*, 343(2):224–231, 2014.

[28] Ken A. Dill and Paul J. Flory. Molecular organization in micelles and vesicles. *Proc. Natl. Acad. Sci. U. S. A.*, 78(2):676–680, 1981.

[29] D. Frenkel and B. Smit. *Understanding Molecular Simulation: From Algorithms to Applications*. Academic Press, 1996.

[30] M.P. Allen and D.J. Tildesley. *Computer Simulation of Liquids*. Oxford Science Publ. Clarendon Press, 1989.

[31] T. Schlick. *Molecular Modeling and Simulation: An Interdisciplinary Guide: An Interdisciplinary Guide*. Interdisciplinary Applied Mathematics. Springer New York, 2010.

[32] David A. Enoch, Jeanine M. Bygott, Marie-Louise Daly, and J. Andreas Karas. Daptomycin. *J. Infect.*, 55(3):205–213, 2007.

[33] Gerrit van Meer, Dennis R. Voelker, and Gerald W. Feigenson. Membrane lipids: where they are and how they behave. *Nat. Rev. Mol. Cell Biol.*, 9(2):112–124, 2008.

[34] João M. Damas, Luís C.S. Filipe, Sara R.R. Campos, Diana Lousa, Bruno L. Victor, António M. Baptista, and Cláudio M. Soares. Predicting the Thermodynamics and Kinetics of Helix Formation in a Cyclic Peptide Model. *J. Chem. Theory Comput.*, 9(11):5148–5157, 2013.

[35] Theodoros Kelesidis. The interplay between daptomycin and the immune system. *Front. Immunol.*, 5(FEB):1–6, 2014.

[36] Tian Hua Zhang, Jawad K. Muraih, Nasim Tishbi, Jennifer Herskowitz, Rachel L. Victor, Jared Silverman, Stephanie Uwumarenogie, Scott D. Taylor, Michael Palmer, and Evan Mintzer. Cardiolipin prevents membrane translocation and permeabilization by daptomycin. *J. Biol. Chem.*, 289(17):11584–11591, 2014.

[37] Tyler Reddy, David Shorthouse, Daniel L. Parton, Elizabeth Jefferys, Philip W. Fowler, Matthieu Chavent, Marc Baaden, and Mark S. P. Sansom. Nothing to Sneeze At: A Dynamic and Integrative Computational Model of an Influenza A Virion. *Structure*, 23(3):584–597, 2015.

[38] S. A. Baeurle. Multiscale modeling of polymer materials using field-theoretic methodologies: A survey about recent developments. *J. Math. Chem.*, 46(2):363–426, 2009.

[39] Dominik Marx and Jurg Hutter. *Ab initio molecular dynamics: Theory and implementation*, volume 1. John von Neumann Institute for Computing, 2000.

[40] Juan J. de Pablo. Coarse-grained simulations of macromolecules: from DNA to nanocomposites. *Annu. Rev. Phys. Chem.*, 62:555–74, 2011.

[41] Alessandro Barducci, Massimiliano Bonomi, and Michele Parrinello. Metadynamics. *Wiley Interdiscip. Rev. Comput. Mol. Sci.*, 1(5):826–843, 2011.

[42] Miguel Preto and Scott Tremaine. A Class of Symplectic Integrators with Adaptive Time Step for Separable Hamiltonian Systems. *Astron. J.*, 118(5):2532–2541, 1999.

[43] Mark E. Tuckerman and Glenn J. Martyna. Understanding Modern Molecular Dynamics: Techniques and Applications. *J. Phys. Chem. B*, 104(2):159–178, 2000.

[44] Murilo L. Tiago and James R. Chelikowsky. First-principles GW-BSE excitations in organic molecules. *Solid State Commun.*, 136(6):333–337, 2005.

[45] John Tatini Titantah and Mikko Karttunen. Hydrophobicity: effect of density and order on water's rotational slowing down. *Soft Matter*, 11(40):7977–7985, 2015.

[46] Adri Van Duin, Siddharth Dasgupta, Francois Lorant, and William A. Goddard. ReaxFF: A reactive force field for hydrocarbons. *J. Phys. Chem. A*, 105(41):9396–9409, 2001.

[47] Loup Verlet. Computer "Experiments" on Classical Fluids. I. Thermodynamical Properties of Lennard-Jones Molecules. *Phys. Rev.*, 159(1):98–103, 1967.

[48] William C. Swope, Hans C. Andersen, Peter H. Berens, and Kent R. Wilson. A computer simulation method for the calculation of equilibrium constants for the formation of physical clusters of molecules: Application to small water clusters. *J. Chem. Phys.*, 76(1):637–649, 1982.

[49] M. Tuckerman, B. J. Berne, and G. J. Martyna. Reversible Multiple Time Scale Molecular Dynamics. *J. Chem. Phys.*, 97(3):1990–2001, 1992.

[50] Ernst Hairer, Christian Lubich, and Gerhard Wanner. Geometric numerical integration illustrated by the StrmerVerlet method. *Acta Numer.*, 12:399–450, 2003.

[51] Søren Toxvaerd. Algorithms for canonical molecular dynamics simulations. *Mol. Phys.*, 72(1):159–168, 1991.

[52] W. F. Drew Bennett, Justin L. MacCallum, and D. Peter Tieleman. Thermodynamic analysis of the effect of cholesterol on dipalmitoylphosphatidylcholine lipid membranes. *J. Am. Chem. Soc.*, 131(5):1972–8, 2009.

[53] Berk Hess, Carsten Kutzner, David van der Spoel, and Erik Lindahl. GROMACS 4 : Algorithms for Highly Efficient, Load-Balanced, and Scalable Molecular Simulation. *J. Chem. Theory Comput.*, 4:435–447, 2008.

[54] Berk Hess. P-LINCS: A Parallel Linear Constraint Solver for Molecular Simulation. *J. Chem. Theory Comput.*, 4(1):116–122, 2008.

[55] Shuichi Miyamoto and Peter A. Kollman. Settle: An analytical version of the SHAKE and RATTLE algorithm for rigid water models. *J. Comput. Chem.*, 13(8):952–962, oct 1992.

[56] Mikko Karttunen, Jörg Rottler, Ilpo Vattulainen, and Celeste Sagui. *Computational Modeling of Membrane Bilayers*, volume 60 of *Current Topics in Membranes*. Elsevier, 2008.

[57] Ulrich Essmann, Lalith Perera, Max L. Berkowitz, Tom Darden, Hsing Lee, and Lee G. Pedersen. A smooth particle mesh Ewald method. *J. Chem. Phys.*, 103(19):8577, 1995.

[58] Abdulnour Y. Toukmaji and John A. Board. Ewald summation techniques in perspective: a survey. *Comput. Phys. Commun.*, 95(2-3):73–92, 1996.

[59] Michael T. Heideman, Don H. Johnson, and C. Sidney Burrus. Gauss and the History of the Fast Fourier Transform. *IEEE ASSP Mag.*, 1(4):14–21, 1984.

[60] G. Andrés Cisneros, Mikko Karttunen, Pengyu Ren, and Celeste Sagui. Classical electrostatics for biomolecular simulations. *Chem. Rev.*, 114(1):779–814, 2014.

[61] Mikko Karttunen, Jrg Rottler, Ilpo Vattulainen, and Celeste Sagui. Chapter 2 electrostatics in biomolecular simulations: Where are we now and where are we heading? In Scott E. Feller, editor, *Computational Modeling of Membrane Bilayers*, volume 60 of *Current Topics in Membranes*, pages 49 – 89. Academic Press, 2008.

[62] Jirasak Wong-ekkabut and Mikko Karttunen. The good, the bad and the user in soft matter simulations. *Biochim. Biophys. Acta - Biomembr.*, (January), 2016.

[63] Jirasak Wong-ekkabut and Mikko Karttunen. Assessment of Common Simulation Protocols for Simulations of Nanopores, Membrane Proteins, and Channels. *J. Chem. Theory Comput.*, 8(8):2905–2911, 2012.

[64] Jirasak Wong-ekkabut, Markus S. Miettinen, Cristiano Dias, and Mikko Karttunen. Static charges cannot drive a continuous flow of water molecules through a carbon nanotube. *Nat. Nanotechnol.*, 5(8):555–557, 2010.

[65] M. Patra, M. Karttunen, M. T. Hyvönen, E. Falck, P. Lindqvist, and I. Vattulainen. Molecular dynamics simulations of lipid bilayers: major artifacts due to truncating electrostatic interactions. *Biophys. J.*, 84(6):3636–45, 2003.

[66] Michael Patra, Mikko Karttunen, Marja T. Hyvönen, Emma Falck, and Ilpo Vattulainen. Lipid Bilayers Driven to a Wrong Lane in Molecular Dynamics Simulations by Subtle Changes in Long-Range Electrostatic Interactions. *J. Phys. Chem. B*, 108(14):4485–4494, 2004.

[67] D. J. Bonthuis, K. Falk, C. N. Kaplan, D. Horinek, A. N. Berker, L. Bocquet, and R. R. Netz. Comment on Pumping of Confined Water in Carbon Nanotubes by Rotation-Translation Coupling. *Phys. Rev. Lett.*, 105(20):209401, 2010.

[68] Douwe Jan Bonthuis, Klaus F Rinne, Kerstin Falk, C. N. Kaplan, Dominik Horinek, A. N. Berker, Lydéric Bocquet, and Roland R. Netz. Theory and simulations of water flow through carbon nanotubes: prospects and pitfalls. *J. Phys. Condens. Matter*, 23(18):184110, 2011.

[69] William L. Jorgensen, David S. Maxwell, and Julian Tirado-Rives. Development and Testing of the OPLS All-Atom Force Field on Conformational Energetics and Properties of Organic Liquids. *J. Am. Chem. Soc.*, 118(45):11225–11236, 1996.

[70] Junmei Wang, Romain M. Wolf, James W. Caldwell, Peter A. Kollman, and David A. Case. Development and testing of a general Amber force field. *J. Comput. Chem.*, 25(9):1157–1174, 2004.

[71] Chris Oostenbrink, Alessandra Villa, Alan E. Mark, and Wilfred F. van Gunsteren. A Biomolecular Force Field Based on the Free Enthalpy of Hydration and Solvation : The GROMOS Force-Field Parameter Sets 53A5 and 53A6. *J. Comput. Chem.*, 25:1656–1676, 2004.

[72] Dirk Matthes and Bert L. De Groot. Secondary structure propensities in peptide folding simulations: A systematic comparison of molecular mechanics interaction schemes. *Biophys. J.*, 97(2):599–608, 2009.

[73] Elio A. Cino, Wing-Yiu Choy, and Mikko Karttunen. Comparison of Secondary Structure Formation Using 10 Different Force Fields in Microsecond Molecular Dynamics Simulations. *J. Chem. Theory Comput.*, 8(8):2725–2740, 2012.

[74] John Hjort Ipsen, Ole G. Mouritsen, and Myer Bloom. Relationships between lipid membrane area, hydrophobic thickness, and acyl-chain orientational order. The effects of cholesterol. *Biophys. J.*, 57(3):405–412, 1990.

[75] Sukit Leekumjorn and Amadeu K. Sum. Molecular studies of the gel to liquid-crystalline phase transition for fully hydrated DPPC and DPPE bilayers. *Biochim. Biophys. Acta*, 1768(2):354–365, 2007.

[76] H.J.C. Berendsen, J.P.M. Postma, W.F. van Gunsteren, and J. Hermans. In B. Pullman, editor, *Intermolecular Forces*, page 331. Reidel, Dordrecht, 1981.

[77] Christian D. Berweger, Wilfred F. van Gunsteren, and Florian Müller-Plathe. Force field parametrization by weak coupling. Re-engineering SPC water. *Chem. Phys. Lett.*, 232:429–436, 1995.

[78] M.W. Evans. On the isolation of possible artifacts due to cubic periodic boundary conditions. *Comput. Phys. Commun.*, 59(3):495–497, 1990.

[79] David J. Adams, Eveline M. Adams, and Graham J. Hills. The computer simulation of polar liquids. *Mol. Phys.*, 38(2):387–400, 1979.

[80] K. Huang. *Statistical mechanics*. Wiley, 1987.

[81] R.K. Pathria and P.D. Beale. *Statistical Mechanics*. Elsevier Science, 1996.

[82] Jacques Hadamard. Book Review: Elementary Principles in Statistical Mechanics, Developed with especial Reference to the Rational Foundations of Thermodynamics. *Bull. Am. Math. Soc.*, 12(4):194–211, 1906.

[83] H. J. C. Berendsen, J. P. M. Postma, W. F. van Gunsteren, a. DiNola, and J. R. Haak. Molecular dynamics with coupling to an external bath. *J. Chem. Phys.*, 81(8):3684, 1984.

[84] Giovanni Bussi, Davide Donadio, and Michele Parrinello. Canonical sampling through velocity rescaling. *J. Chem. Phys.*, 126:014101, 2007.

[85] M. Lingenheil, R. Denschlag, R. Reichold, and P. Tavan. The Hot-Solvent/Cold-Solute Problem Revisited. *J. Chem. Theory Comput.*, 4(8):1293–1306, 2008.

[86] M. Parrinello. Polymorphic transitions in single crystals: A new molecular dynamics method. *J. Appl. Phys.*, 52(12):7182, 1981.

[87] Shuichi Nosé and M.L. Klein. Constant pressure molecular dynamics for molecular systems. *Mol. Phys.*, 50(5):1055–1076, 1983.

[88] Svetlana Baoukina, Luca Monticelli, H. Jelger Risselada, Siewert J. Marrink, and D. Peter Tieleman. The molecular mechanism of lipid monolayer collapse. *Proc. Natl. Acad. Sci. U. S. A.*, 105(31):10803–8, 2008.

[89] Sandra Storm, Sven Jakobtorweihen, Irina Smirnova, and Athanassios Z. Panagiotopoulos. Molecular dynamics simulation of SDS and CTAB micellization and prediction of partition equilibria with COSMOmic. *Langmuir*, 29(37):11582–92, 2013.

[90] Jérôme Hénin, Wataru Shinoda, and Michael L. Klein. Models for phosphatidylglycerol lipids put to a structural test. *J. Phys. Chem. B*, 113:6958–6963, 2009.

[91] Torben Broemstrup and Nathalie Reuter. Molecular dynamics simulations of mixed acidic/zwitterionic phospholipid bilayers. *Biophys. J.*, 99(3):825–833, 2010.

[92] J.B. Reece. *Campbell Biology*. Benjamin Cummings / Pearson, 2011.

[93] Svetlana Baoukina, Siewert J. Marrink, and D. Peter Tieleman. Structure and dynamics of lipid monolayers: theory and applications. In Roland Faller, Thomas Jue, Marjorie L. Longo, and Subhash H. Risbud, editors, *Biomembr. Front. Nanostructures, Model. Des. Life*, volume 2899311, chapter 3, pages 75–99. Humana Press, New York, 2009.

[94] Arnold H. Pelofsky. Surface Tension-Viscosity Relation for Liquids. *J. Chem. Eng. Data*, 11(3):394–397, 1966.

[95] Yasuhiko H. Mori, Nobuhiko Tsui, and Masaaki Kiyomiya. Surface and interfacial tensions and their combined properties in seven binary, immiscible liquid-liquid-vapor systems. *J. Chem. Eng. Data*, 29(4):407–412, 1984.

[96] R. Nagarajan. Amphiphilic surfactants and amphiphilic polymers: Principles of molecular assembly. *ACS Symp. Ser.*, 1070:1–22, 2011.

[97] Feng Chen and Paul E. Smith. Simulated surface tensions of common water models. *J. Chem. Phys.*, 126:221101, 2007.

[98] Rodney L. Biltonen and Dov Lichtenberg. The use of differential scanning calorimetry as a tool to characterize liposome preparations. *Chem. Phys. Lipids*, 64(1-3):129–142, 1993.

[99] O. Enders, A. Ngezahayo, M. Wiechmann, F. Leisten, and H.-A. Kolb. Structural calorimetry of main transition of supported DMPC bilayers by temperature-controlled AFM. *Biophys. J.*, 87(4):2522–2531, 2004.

[100] Karin A. Riske, Roberto M. Fernandez, Otaciro R. Nascimento, Barney L. Bales, and M. Teresa Lamy-Freund. DMPG gel-fluid thermal transition monitored by a phospholipid spin labeled at the acyl chain end. *Chem. Phys. Lipids*, 124(1):69–80, 2003.

[101] Christophe Ybert, Weixing Lu, Gunter Möller, and Charles M. Knobler. Collapse of a Monolayer by Three Mechanisms. *J. Phys. Chem. B*, 106(8):2004–2008, 2002.

[102] Ka Yee C. Lee. Collapse mechanisms of Langmuir monolayers. *Annu. Rev. Phys. Chem.*, 59:771–91, 2008.

[103] Luka Pocivavsek, Shelli L. Frey, Kapilanjan Krishan, Kseniya Gavrilov, Piotr Ruchala, Alan J. Waring, Frans J. Walther, Michael Dennin, Thomas A. Witten, and Ka Yee C. Lee. Lateral stress relaxation and collapse in lipid monolayers. *Soft Matter*, 4:2019–2029, 2008.

[104] Bin Liu, Matthew I Hoopes, and Mikko Karttunen. Molecular Dynamics Simulations of DPPC/CTAB Monolayers at the Air/Water Interface. *J. Phys. Chem. B*, 118(40):11723–37, 2014.

[105] Bin Liu, Jirasak Wong-Ekkabut, and Mikko Karttunen. Molecular Dynamics Simulation of Surfactant Monolayers. In Mohammad Taeibi Rahni, Mohsen Karbaschi, and Reinhard Miller, editors, *Comput. Methods Complex Liq. Interfaces*, chapter 11, pages 249–264. CRC Press, 2015.

[106] Pierre Tremouilhac, Erik Strandberg, Parvesh Wadhwani, and Anne S. Ulrich. Synergistic transmembrane alignment of the antimicrobial heterodimer PGLa/magainin. *J. Biol. Chem.*, 281(43):32089–32094, 2006.

[107] Joël Janin. Physical biology of the cell, Second Edition. *Crystallogr. Rev.*, 19(4):273–274, 2013.

[108] Mingyang Hu, Patrick Diggins, and Markus Deserno. Determining the bending modulus of a lipid membrane by simulating buckling. *J. Chem. Phys.*, 138(21):214110, 2013.

[109] Simon Faiss, Eike Lüthgens, and Andreas Janshoff. Adhesion and rupture of liposomes mediated by electrostatic interaction monitored by thickness shear mode resonators. *Eur. Biophys. J.*, 33(6):555–61, 2004.

[110] Mingyang Hu, John J Briguglio, and Markus Deserno. Determining the Gaussian curvature modulus of lipid membranes in simulations. *Biophys. J.*, 102(6):1403–10, 2012.

[111] Sascha Martens and Harvey T. McMahon. Mechanisms of membrane fusion: disparate players and common principles. *Nat. Rev. Mol. Cell Biol.*, 9(7):543–556, 2008.

[112] K.L. Wardle. *Differential Geometry*. Dover books on mathematics. Dover Publications, 2008.

[113] W. Helfrich. Elastic Properties of Lipid Bilayers: Theory and Possible Experiments. *Zeitschrift fur Naturforsch. - Sect. C J. Biosci.*, 28(11-12):693–703, 1973.

[114] S. O. Yesylevskyy and C. Ramseyer. Determination of mean and Gaussian curvatures of highly curved asymmetric lipid bilayers: the case study of the influence of cholesterol on the membrane shape. *Phys. Chem. Chem. Phys.*, 16(32):17052–61, 2014.

[115] Lars Robbel and Mohamed A. Marahiel. Daptomycin, a bacterial lipopeptide synthesized by a nonribosomal machinery. *J. Biol. Chem.*, 285(36):27501–27508, 2010.

[116] Diana Gaspar, A. Salome Veiga, and Miguel A. R. B. Castanho. From antimicrobial to anticancer peptides. A review. *Front. Microbiol.*, 4(OCT):1–16, 2013.

[117] Min-Duk Seo, Hyung-Sik Won, Ji-Hun Kim, Tsogbadrakh Mishig-Ochir, and Bong-Jin Lee. Antimicrobial Peptides for Therapeutic Applications: A Review. *Molecules*, 17(10):12276–12286, 2012.

[118] Leonard T. Nguyen, Evan F. Haney, and Hans J. Vogel. The expanding scope of antimicrobial peptide structures and their modes of action. *Trends Biotechnol.*, 29(9):464–472, 2011.

[119] Noelle H. O'Driscoll, Olga Labovitiadi, T. P. Tim Cushnie, Kerr H. Matthews, Derry K. Mercer, and Andrew J. Lamb. Production and evaluation of an antimicrobial peptide-containing Wafer formulation for topical application. *Curr. Microbiol.*, 66(3):271–278, 2013.

[120] Robert E. W. Hancock and Hans-Georg Sahl. Antimicrobial and host-defense peptides as new anti-infective therapeutic strategies. *Nat. Biotechnol.*, 24(12):1551–7, 2006.

[121] Katsumi Matsuzaki. Control of cell selectivity of antimicrobial peptides. *Biochim. Biophys. Acta - Biomembr.*, 1788(8):1687–1692, 2009.

[122] Hung Ta Chou, Tsun Yung Kuo, Jung Chun Chiang, Min Ju Pei, Wei Ter Yang, Hui Chun Yu, Shih Bin Lin, and Wei Jung Chen. Design and synthesis of cationic antimicrobial peptides with improved activity and selectivity against Vibrio spp. *Int. J. Antimicrob. Agents*, 32(2):130–138, 2008.

[123] Lucia Becucci, Daniela Valensin, Massimo Innocenti, and Rolando Guidelli. Dermcidin, an anionic antimicrobial peptide: influence of lipid charge, pH and Zn2+ on its interaction with a biomimetic membrane. *Soft Matter*, 10:616–26, 2014.

[124] Ren Lai, Hen Liu, Wen Hui Lee, and Yun Zhang. An anionic antimicrobial peptide from toad Bombina maxima. *Biochem. Biophys. Res. Commun.*, 295(4):796–799, 2002.

[125] J. R. Woodworth, E. H. Nyhart, G. L. Brier, J. D. Wolny, and H. R. Black. Single-dose pharmacokinetics and antibacterial activity of daptomycin, a new lipopeptide antibiotic, in healthy volunteers. *Antimicrob. Agents Chemother.*, 36(2):318–325, 1992.

[126] Christopher F. Carpenter and Henry F. Chambers. Daptomycin: another novel agent for treating infections due to drug-resistant gram-positive pathogens. *Clin. Infect. Dis.*, 38(7):994–1000, 2004.

[127] Barry I. Eisenstein, Frederick B. Oleson, Jr., and Richard H. Baltz. Daptomycin: From the Mountain to the Clinic, with Essential Help from Francis Tally, MD. *Clin. Infect. Dis.*, 50(s1):S10–S15, jan 2010.

[128] Jeremy H. Lakey and Marius Ptak. Fluorescence indicates a calcium-dependent interaction between the lipopeptide antibiotic LY146032 and phospholipid membranes. *Biochemistry*, 27(13):4639–4645, 1988.

[129] Jeremy H. Lakey, Regine Maget-Dana, and Marius Ptak. The lipopeptide antibiotic A21978C has a specific interaction with DMPC only in the presence of calcium ions. *BBA - Biomembr.*, 985(1):60–66, 1989.

[130] Marzia Boaretti, Pietro Canepari, Maria del Mar Lleò, and Giuseppe Satta. The activity of daptomycin on Enterococcus faecium protoplasts: indirect evidence supporting a novel mode of action on lipoteichoic acid synthesis. *J Antimicrob Chemother*, 31:227–235, 1993.

[131] Jared A. Silverman, Nicole Oliver, Ted Andrew, and L. I. Tongchuan. Resistance studies with daptomycin. *Antimicrob. Agents Chemother.*, 45(6):1799–1802, 2001.

[132] Jared A. Silverman, Nancy G. Perlmutter, and Howard M. Shapiro. Correlation of daptomycin bactericidal activity and membrane depolarization in Staphylococcus aureus. *Antimicrob. Agents Chemother.*, 47(8):2538–2544, 2003.

[133] Valerie Laganas, Jeffrey Alder, and Jared A. Silverman. In Vitro Bactericidal Activities of Daptomycin against Staphylococcus aureus and Enterococcus faecalis Are Not Mediated by Inhibition of Lipoteichoic Acid Biosynthesis. *Antimicrob. Agents Chemother.*, 47(8):2682–2684, 2003.

[134] Richard H. Baltz, Vivian Miao, and Stephen K. Wrigley. Natural products to drugs: daptomycin and related lipopeptide antibiotics. *Nat. Prod. Rep.*, 22(6):717, 2005.

[135] Richard H. Baltz. Daptomycin: mechanisms of action and resistance, and biosynthetic engineering. *Curr. Opin. Chem. Biol.*, 13(2):144–151, 2009.

[136] Anna-Barbara A.-B. Hachmann, Esther R. Angert, and John D. Helmann. Genetic Analysis of Factors Affecting Susceptibility of Bacillus subtilis to Daptomycin. *Antimicrob. Agents Chemother.*, 53(4):1598–609, 2009.

[137] Nagendra N. Mishra, Soo Jin Yang, Ayumi Sawa, Aileen Rubio, Cynthia C. Nast, Michael R. Yeaman, and Arnold S. Bayer. Analysis of cell membrane characteristics of in vitro-selected daptomycin-resistant strains of methicillin-resistant Staphylococcus aureus. *Antimicrob. Agents Chemother.*, 53(6):2312–2318, 2009.

[138] Anna Barbara Hachmann, Elif Sevim, Ahmed Gaballa, David L. Popham, Haike Antelmann, and John D. Helmann. Reduction in membrane phosphatidylglycerol content leads to daptomycin resistance in Bacillus subtilis. *Antimicrob. Agents Chemother.*, 55(9):4326–4337, 2011.

[139] Yen-fei Chen, Tzu-lin Sun, Yen Sun, and Huey W. Huang. Interaction of Daptomycin with Lipid Bilayers: A Lipid Extracting Effect. *Biochemistry*, 53:5384–5392, 2014.

[140] P. Canepari, M. Boaretti, M. Del Mar Lleo, and G. Satta. Lipoteichoic acid as a new target for activity of antibiotics: Mode of action of daptomycin (LY146032). *Antimicrob. Agents Chemother.*, 34(6):1220–1226, 1990.

[141] David Jung, Annett Rozek, Mark Okon, and Robert E.W. Hancock. Structural Transitions as Determinants of the Action of the Calcium-Dependent Antibiotic Daptomycin. *Chem. Biol.*, 11(7):949–957, 2004.

[142] Suzana K. Straus and Robert E. W. Hancock. Mode of action of the new antibiotic for Gram-positive pathogens daptomycin: Comparison with cationic antimicrobial peptides and lipopeptides. *Biochim. Biophys. Acta - Biomembr.*, 1758(9):1215–1223, 2006.

[143] Tianhua Zhang, Jawad K Muraih, Evan Mintzer, Nasim Tishbi, Celine Desert, Jared Silverman, Scott Taylor, and Michael Palmer. Mutual inhibition through hybrid oligomer formation of daptomycin and the semisynthetic lipopeptide antibiotic CB-182,462. *Biochim. Biophys. Acta*, 1828(2):302–308, 2013.

[144] David Jung, Jon Paul Powers, Suzana K. Straus, and Robert E. W. Hancock. Lipid-specific binding of the calcium-dependent antibiotic daptomycin leads to changes in lipid polymorphism of model membranes. *Chem. Phys. Lipids*, 154(2):120–128, 2008.

[145] Walter R. P. Scott, Seung Bin Baek, David Jung, Robert E. W. Hancock, and Suzana K. Straus. NMR structural studies of the antibiotic lipopeptide daptomycin in DHPC micelles. *Biochim. Biophys. Acta - Biomembr.*, 1768(12):3116–3126, 2007.

[146] Steven W. Ho, David Jung, Jennifer R. Calhoun, James D. Lear, Mark Okon, Walter R P Scott, Robert E W Hancock, and Suzana K. Straus. Effect of divalent cations on the structure of the antibiotic daptomycin. *Eur. Biophys. J.*, 37(4):421–433, 2008.

[147] Patrick J. Sherman, Rebecca J. Jackway, John D. Gehman, Slavica Praporski, George A. McCubbin, Adam Mechler, Lisandra L. Martin, Frances Separovic, and John H. Bowie. Solution structure and membrane interactions of the antimicrobial peptide fallaxidin 4.1a: An NMR and QCM study. *Biochemistry*, 48(50):11892–11901, 2009.

[148] Stefania Piantavigna, George A. McCubbin, Solveig Boehnke, Bim Graham, Leone Spiccia, and Lisandra L. Martin. A mechanistic investigation of cell-penetrating Tat peptides with supported lipid membranes. *Biochim. Biophys. Acta - Biomembr.*, 1808(7):1811–1817, 2011.

[149] Kristopher Hall, Tzong-Hsien Lee, Adam I. Mechler, Marcus J. Swann, and Marie-Isabel Aguilar. Real-time Measurement of Membrane Conformational States Induced by Antimicrobial Peptides: Balance Between Recovery and Lysis. *Sci. Rep.*, 4:5479, 2014.

[150] G. A. Pankuch, M. R. Jacobs, and P. C. Appelbaum. Postantibiotic effects of daptomycin against 14 staphylococcal and pneumococcal clinical isolates. *Antimicrob. Agents Chemother.*, 47(9):3012–3014, 2003.

[151] W. Brown, B. Iverson, E. Anslyn, and C. Foote. *Organic Chemistry*. Cengage Learning, 2013.

[152] Jiang Qiu and Lee E. Kirsch. Evaluation of lipopeptide (daptomycin) aggregation using fluorescence, light scattering, and nuclear magnetic resonance spectroscopy. *J. Pharm. Sci.*, 103:853–861, 2014.

[153] Walaisiri Muangsiri and Lee E. Kirsch. The kinetics of the alkaline degradation of daptomycin. *J. Pharm. Sci.*, 90(8):1066–1075, 2001.

[154] P.M. Woster and R.A. Casero. *Polyamine Drug Discovery.* RSC drug discovery series. Royal Society of Chemistry, 2011.

[155] Jiang Qiu, Liping Yu, and Lee E. Kirsch. Estimated pKa Values for Specific Amino Acid Residues in Daptomycin. *J. Pharm. Sci.*, 100(10):4225–4233, 2011.

[156] Alexander W. Schüttelkopf and Daan M. F. van Aalten. PRODRG: a tool for high-throughput crystallography of protein-ligand complexes. *Acta Crystallogr. D. Biol. Crystallogr.*, D60:1355–1363, 2004.

[157] Siewert J. Marrink, Alex H. de Vries, and Alan E. Mark. Coarse Grained Model for Semiquantitative Lipid Simulations. *J. Phys. Chem. B*, 108(2):750–760, 2004.

[158] Siewert J. Marrink and D. Peter Tieleman. Perspective on the Martini model. *Chem. Soc. Rev.*, 42(16):6801–6822, 2013.

[159] George A. Kaminski, Richard A. Friesner, Julian Tirado-Rives, and William L. Jorgensen. Evaluation and Reparametrization of the OPLS-AA Force Field for Proteins via Comparison with Accurate Quantum Chemical Calculations on Peptides . *J. Phys. Chem. B*, 105(28):6474–6487, 2001.

[160] Wendy D. Cornell, Piotr Cieplak, Christopher I. Bayly, Ian R. Gould, Kenneth M. Merz, David M. Ferguson, David C. Spellmeyer, Thomas Fox, James W. Caldwell, and Peter A. Kollman. A Second Generation Force Field for the Simulation of Proteins, Nucleic Acids, and Organic Molecules. *J. Am. Chem. Soc.*, 117(19):5179–5197, 1995.

[161] Junmei Wang, Piotr Cieplak, and Peter A. Kollman. How well does a restrained electrostatic potential (RESP) model perform in calculating conformational energies of organic and biological molecules? *J. Comput. Chem.*, 21(12):1049–1074, 2000.

[162] Eric J. Sorin and Vijay S. Pande. Exploring the helix-coil transition via all-atom equilibrium ensemble simulations. *Biophys. J.*, 88(4):2472–93, 2005.

[163] Yong Duan, Chun Wu, Shibasish Chowdhury, Mathew C. Lee, Guoming Xiong, Wei Zhang, Rong Yang, Piotr Cieplak, Ray Luo, Taisung Lee, James Caldwell, Junmei Wang, and Peter Kollman. A point-charge force field for molecular mechanics simulations of proteins based on condensed-phase quantum mechanical calculations. *J. Comput. Chem.*, 24(16):1999–2012, 2003.

[164] Eyal Neria, Stefan Fischer, and Martin Karplus. Simulation of activation free energies in molecular systems. *J. Chem. Phys.*, 105(5):1902, 1996.

[165] A. D. MacKerell, D. Bashford, M. Bellott, R. L. Dunbrack, J. D. Evanseck, M. J. Field, S. Fischer, J. Gao, H. Guo, S. Ha, D. Joseph-McCarthy, L. Kuchnir, K. Kuczera, F. T. Lau, C. Mattos, S. Michnick, T. Ngo, D. T. Nguyen, B. Prodhom, W. E. Reiher, B. Roux, M. Schlenkrich, J. C. Smith, R. Stote, J. Straub, M. Watanabe, J. Wiórkiewicz-Kuczera, D. Yin, and M. Karplus. All-atom empirical potential for molecular modeling and dynamics studies of proteins. *J. Phys. Chem. B*, 102(18):3586–616, 1998.

[166] Alexander D. Mackerell, Michael Feig, and Charles L. Brooks. Extending the treatment of backbone energetics in protein force fields: limitations of gas-phase quantum mechanics in reproducing protein conformational distributions in molecular dynamics simulations. *J. Comput. Chem.*, 25(11):1400–15, 2004.

[167] Walter R. P. Scott, Philippe H. Hünenberger, Ilario G. Tironi, Alan E. Mark, Salomon R. Billeter, Jens Fennen, Andrew E. Torda, Thomas Huber, Peter Krüger, and Wilfred F. van Gunsteren. The GROMOS Biomolecular Simulation Program Package. *J. Phys. Chem. A*, 103(19):3596–3607, 1999.

[168] Xavier Daura, Alan E. Mark, and Wilfred F. van Gunsteren. Parametrization of Aliphatic CHn United Atoms of GROMOS96 Force Field. *J. Comput. Chem.*, 19(5):535–547, 1998.

[169] Oliver Berger, Olle Edholm, and Fritz Jahnig. Molecular Dynamics Simulations of a Fluid Bilayer of Dipalmitoylphosphatidylcholine at Full Hydration , Constant Pressure , and Constant Temperature. *Biophys. J.*, 72:2002–2013, 1997.

[170] http://wcm.ucalgary.ca/tieleman/downloads.

[171] Andrey A. Gurtovenko, Michael Patra, Mikko Karttunen, and Ilpo Vattulainen. Cationic DMPC/DMTAP lipid bilayers: molecular dynamics study. *Biophys. J.*, 86(6):3461–72, 2004.

[172] Michal Bachar, Patrick Brunelle, D. Peter Tieleman, and Arvi Rauk. Molecular dynamics simulation of a polyunsaturated lipid bilayer susceptible to lipid peroxidation. *J. Phys. Chem. B*, 108(22):7170–7179, 2004.

[173] Hector Martinez-Seara, Tomasz Rog, Mikko Karttunen, Ramon Reigada, and Ilpo Vattulainen. Influence of cis double-bond parametrization on lipid membrane properties: How seemingly insignificant details in force-field change even qualitative trends. *J. Chem. Phys.*, 129(10), 2008.

[174] Wei Zhao, Tomasz Róg, Andrey A. Gurtovenko, Ilpo Vattulainen, and Mikko Karttunen. Atomic-scale structure and electrostatics of anionic palmitoyloleoylphosphatidylglycerol lipid bilayers with Na+ counterions. *Biophys. J.*, 92(4):1114–24, 2007.

[175] M. J. Frisch, G. W. Trucks, H. B. Schlegel, G. E. Scuseria, M. A. Robb, J. R. Cheeseman, J. A. Montgomery, Jr., T. Vreven, K. N. Kudin, J. C. Burant, J. M. Millam, S. S. Iyengar, J. Tomasi, V. Barone, B. Mennucci, M. Cossi, G. Scalmani, N. Rega, G. A. Petersson, H. Nakatsuji, M. Hada, M. Ehara, K. Toyota, R. Fukuda, J. Hasegawa, M. Ishida, T. Nakajima, Y. Honda, O. Kitao, H. Nakai, M. Klene, X. Li, J. E. Knox, H. P. Hratchian, J. B. Cross, V. Bakken, C. Adamo, J. Jaramillo, R. Gomperts, R. E. Stratmann, O. Yazyev, A. J. Austin, R. Cammi, C. Pomelli, J. W. Ochterski, P. Y. Ayala, K. Morokuma, G. A. Voth, P. Salvador, J. J. Dannenberg, V. G. Zakrzewski, S. Dapprich, A. D. Daniels, M. C. Strain, O. Farkas, D. K. Malick, A. D. Rabuck, K. Raghavachari, J. B. Foresman, J. V. Ortiz, Q. Cui, A. G. Baboul, S. Clifford, J. Cioslowski, B. B. Stefanov, G. Liu, A. Liashenko, P. Piskorz, I. Komaromi, R. L. Martin, D. J. Fox, T. Keith, M. A. Al-Laham, C. Y. Peng, A. Nanayakkara, M. Challacombe, P. M. W. Gill, B. Johnson, W. Chen, M. W. Wong, C. Gonzalez, and J. A. Pople. Gaussian 03, Revision C.02. Gaussian, Inc., Wallingford, CT, 2004.

[176] Michael W. Schmidt, Kim K. Baldridge, Jerry A. Boatz, Steven T. Elbert, Mark S. Gordon, Jan H. Jensen, Shiro Koseki, Nikita Matsunaga, Kiet A. Nguyen, Shujun Su, Theresa L. Windus, Michel Dupuis, and John A. Montgomery. General atomic and molecular electronic structure system. *J. Comput. Chem.*, 14(11):1347–1363, 1993.

[177] Mark S. Gordon and Michael W. Schmidt. Advances in Electronic structure theory: GAMESS a decade later. In C. E. Dykstra, G. Frenking, K. S. Kim, and G. E. Scuseria, editors, *Theory Appl. Comput. Chem. first forty years*, pages 1167–1189. Elsevier, Amsterdam, 2005.

[178] Alex A. Granovsky. Firefly quantum chemistry package version 8. http://classic.chem.msu.su/gran/firefly/index.html.

[179] R. Ditchfield, W. J. Hehre, and J. A. Pople. Self-Consistent Molecular-Orbital Methods. IX. An Extended Gaussian-Type Basis for Molecular-Orbital Studies of Organic Molecules. *J. Chem. Phys.*, 54(2):724, 1971.

[180] W. J. Hehre, R. Ditchfield, and J. A. Pople. SelfConsistent Molecular Orbital Methods. XII. Further Extensions of GaussianType Basis Sets for Use in Molecular Orbital Studies of Organic Molecules. *J. Chem. Phys.*, 56(5):2257, 1972.

[181] P. C. Hariharan and J. A. Pople. The Influence of Polarization Functions on Molecular Orbital Hydrogenation Energies. *Theor. Chem. Acc.*, 28:213–222, 1973.

[182] Viktor Hornak, Robert Abel, Asim Okur, Bentley Strockbine, Adrian Roitberg, and Carlos Simmerling. Comparison of multiple Amber force fields and development of improved protein backbone parameters. *Proteins*, 65(3):712–25, 2006.

[183] G. A. Petersson, Andrew Bennett, Thomas G. Tensfeldt, Mohammad A. Al-Laham, William A. Shirley, and John Mantzaris. A complete basis set model chemistry. I. The total energies of closed-shell atoms and hydrides of the first-row elements. *J. Chem. Phys.*, 89(4):2193, 1988.

[184] G. A. Petersson and Mohammad A. Al-Laham. A complete basis set model chemistry. II. Open-shell systems and the total energies of the first-row atoms. *J. Chem. Phys.*, 94(9):6081, 1991.

[185] R. S. Mulliken. Electronic Population Analysis on LCAO[Single Bond]MO Molecular Wave Functions. I. *J. Chem. Phys.*, 23(10):1833, 1955.

[186] R. S. Mulliken. Criteria for the Construction of Good Self-Consistent-Field Molecular Orbital Wave Functions, and the Significance of LCAO-MO Population Analysis. *J. Chem. Phys.*, 36(12):3428, 1962.

[187] Per-Olov Löwdin. Advances in Quantum Chemistry Volume 5. 5:185–199, 1970.

[188] L.Ch. Cusachs and P. Politzer. On the problem of defining the charge on an atom in a molecule. *Chem. Phys. Lett.*, 1(11):529–531, 1968.

[189] Donald E. Williams. *Net Atomic Charge and Multipole Models for the ab Initio Molecular Electric Potential*, pages 219–271. John Wiley Sons, Inc., 2007.

[190] Bingze Wang and George P. Ford. Atomic charges derived from a fast and accurate method for electrostatic potentials based on modified AM1 calculations. *J. Comput. Chem.*, 15(2):200–207, 1994.

[191] Kevin C. Gross, Paul G. Seybold, and Christopher M. Hadad. Comparison of different atomic charge schemes for predicting pKa variations in substituted anilines and phenols. *Int. J. Quantum Chem.*, 90(1):445–458, 2002.

[192] Radka Svobodová Vareková, Stanislav Geidl, Crina-Maria Ionescu, Ondrej Skrehota, Michal Kudera, David Sehnal, Tomás Bouchal, Ruben Abagyan, Heinrich J. Huber, and Jaroslav Koca. Predicting pK(a) values of substituted phenols from atomic charges: comparison of different quantum mechanical methods and charge distribution schemes. *J. Chem. Inf. Model.*, 51(8):1795–806, 2011.

[193] E. D. Glendening, J. K. Badenhoop, A. E. Reed, J. E. Carpenter, J. A. Bohmann, C. M. Morales, and F. Weinhold. Nbo 5.9. http://www.chem.wisc.edu/~nbo5, 2012. Theoretical Chemistry Institute, University of Wisconsin, Madison, WI, 2012.

[194] S. Miertuš, E. Scrocco, and J. Tomasi. Electrostatic interaction of a solute with a continuum. A direct utilizaion of AB initio molecular potentials for the prevision of solvent effects. *Chem. Phys.*, 55(1):117–129, 1981.

[195] Jacopo Tomasi and Maurizio Persico. Molecular Interactions in Solution: An Overview of Methods Based on Continuous Distributions of the Solvent. *Chem. Rev.*, 94(7):2027–2094, 1994.

[196] R. Cammi and J. Tomasi. Remarks on the Use of the Apparent Surface Charges (ASC) Methods in Solvation Problems : Iterative versus Matrix-Inversion Procedures and the Renormalization of the Apparent Charges. *J. Comput. Chem.*, 16(12):1449–1458, 1995.

[197] Jacopo Tomasi, Benedetta Mennucci, and Roberto Cammi. Quantum mechanical continuum solvation models. *Chem. Rev.*, 105(8):2999–3093, 2005.

[198] Brett M. Bode and Mark S. Gordon. Macmolplt: a graphical user interface for GAMESS. *J. Mol. Graph. Model.*, 16(3):133–138, 1998.

[199] Yiannis N. Kaznessis, Sangtae Kim, and Ronald G Larson. Simulations of zwitterionic and anionic phospholipid monolayers. *Biophys. J.*, 82(4):1731–42, 2002.

[200] James C. Phillips, Rosemary Braun, Wei Wang, James Gumbart, Emad Tajkhorshid, Elizabeth Villa, Christophe Chipot, Robert D. Skeel, Laxmikant Kalé, and Klaus Schulten. Scalable molecular dynamics with NAMD. *J. Comput. Chem.*, 26(16):1781–802, 2005.

[201] David A. Case, Thomas E. Cheatham, Tom Darden, Holger Gohlke, Ray Luo, Kenneth M. Merz, Alexey Onufriev, Carlos Simmerling, Bing Wang, and Robert J. Woods. The Amber biomolecular simulation programs. *J. Comput. Chem.*, 26(16):1668–88, 2005.

[202] Shuichi Nose. A unified formulation of the constant temperature molecular dynamics methods. *J. Chem. Phys.*, 81(1):511, 1984.

[203] William G. Hoover. Canonical dynamics: Equilibrium phase-space distributions. *Phys. Rev. A*, 31(3):1695–1697, 1985.

[204] Glenn J. Martyna, Michael L. Klein, and Mark Tuckerman. Nose-Hoover chains: The canonical ensemble via continuous dynamics. *J. Chem. Phys.*, 97(4):2635, 1992.

[205] Hans C. Andersen. Molecular dynamics simulations at constant pressure and/or temperature. *J. Chem. Phys.*, 72(4):2384, 1980.

[206] Darrin M. York, Tom A. Darden, and Lee G. Pedersen. The effect of long-range electrostatic interactions in simulations of macromolecular crystals: A comparison of the Ewald and truncated list methods. *J. Chem. Phys.*, 99(10):8345, 1993.

[207] Michael Patra, Marja T. Hyvönen, Emma Falck, Mohsen Sabouri-Ghomi, Ilpo Vattulainen, and Mikko Karttunen. Long-range interactions and parallel scalability in molecular simulations. *Comput. Phys. Commun.*, 176(1):14–22, 2007.

[208] J. A. Barker and R. O. Watts. Monte Carlo studies of the dielectric properties of water-like models. *Mol. Phys.*, 26(3):789–792, 1973.

[209] Christopher J. Johnson, Erik Dujardin, Sean A. Davis, Catherine J. Murphy, and Stephen Mann. Growth and form of gold nanorods prepared by seed-mediated, surfactant-directed synthesis. *J. Mater. Chem.*, 12(6):1765–1770, 2002.

[210] W. Humphrey, A. Dalke, and K. Schulten. VMD: visual molecular dynamics. *J. Mol. Graph.*, 14(1):33–8, 27–8, 1996.

[211] John Stone. An efficient library for parallel ray tracing and animation. Technical report, In Intel Supercomputer Users Group Proceedings, 1995.

[212] Jonathan M. Crane, Günther Putz, and Stephen B. Hall. Persistence of Phase Coexistence in Disaturated Phosphatidylcholine Monolayers at High Surface Pressures. *Biophys. J.*, 77(6):3134–43, 1999.

[213] Angela K. Pannier, Brian C. Anderson, and Lonnie D. Shea. Substrate-mediated delivery from self-assembled monolayers: effect of surface ionization, hydrophilicity, and patterning. *Acta Biomater.*, 1(5):511–22, 2005.

[214] Chiranjeevi Peetla and Vinod Labhasetwar. Effect of molecular structure of cationic surfactants on biophysical interactions of surfactant-modified nanoparticles with a model membrane and cellular uptake. *Langmuir*, 25(4):2369–77, 2009.

[215] Ashwin Basarkar and Jagdish Singh. Nanoparticulate systems for polynucleotide delivery. *Int. J. Nanomedicine*, 2(3):353–60, 2007.

[216] Sylwia Gaweda, M. Carmen Morán, Alberto A. C. C. Pais, Rita S. Dias, Karin Schillén, Björn Lindman, and M. Graça Miguel. Cationic agents for DNA compaction. *J. Colloid Interface Sci.*, 323(1):75–83, 2008.

[217] Amalia Mezei, Ramon Pons, and M. Carmen Morán. The nanostructure of surfactant-DNA complexes with different arrangements. *Colloids Surf. B. Biointerfaces*, 111C:663–671, 2013.

[218] Rema Krishnaswamy, Georg Pabst, Michael Rappolt, V. A. Raghunathan, and A. K. Sood. Structure of DNA-CTAB-hexanol complexes. *Phys. Rev. E*, 73(3):031904, 2006.

[219] Cristina Stefaniu, Gerald Brezesinski, and Helmuth Möhwald. Langmuir monolayers as models to study processes at membrane surfaces. *Adv. Colloid Interface Sci.*, 208:197–213, 2014.

[220] Matti Javanainen, Luca Monticelli, Jorge Bernardino de la Serna, and Ilpo Vattulainen. Free volume theory applied to lateral diffusion in Langmuir monolayers: atomistic simulations for a protein-free model of lung surfactant. *Langmuir*, 26(19):15436–44, 2010.

[221] Markus S. Miettinen, Andrey A. Gurtovenko, Ilpo Vattulainen, and Mikko Karttunen. Ion dynamics in cationic lipid bilayer systems in saline solutions. *J. Phys. Chem. B*, 113(27):9226–34, 2009.

[222] Joachim Seelig, Peter M. Macdonald, and Peter G. Scherer. Phospholipid head groups as sensors of electric charge in membranes. *Biochemistry*, 26(24):7535–41, 1987.

[223] Peter G. Scherer and Joachim Seelig. Electric charge effects on phospholipid headgroups. Phosphatidylcholine in mixtures with cationic and anionic amphiphiles. *Biochemistry*, 28(19):7720–8, 1989.

[224] Jacques P. F. Doux, Benjamin A. Hall, and J. Antoinette Killian. How lipid headgroups sense the membrane environment: an application of N NMR. *Biophys. J.*, 103(6):1245–53, 2012.

[225] Liangfang Zhang, Juliana M. Chan, Frank X. Gu, June-Wha Rhee, Andrew Z. Wang, Aleksandar F. Radovic-Moreno, Frank Alexis, Robert Langer, and Omid C. Farokhzad. Self-assembled lipid–polymer hybrid nanoparticles: a robust drug delivery platform. *ACS Nano*, 2(8):1696–702, 2008.

[226] Vladimir Kaganer, Helmuth Möhwald, and Pulak Dutta. Structure and phase transitions in Langmuir monolayers. *Rev. Mod. Phys.*, 71(3):779–819, 1999.

[227] S. Schürch, H. Bachofen, J. Goerke, and F. Possmayer. A captive bubble method reproduces the in situ behavior of lung surfactant monolayers. *J. Appl. Physiol.*, 67(6):2389–96, 1989.

[228] Feng Wang, Jinghe Yang, Xia Wu, Fei Wang, and Honghong Ding. Investigation of the interaction between curcumin and nucleic acids in the presence of CTAB. *Spectrochim. Acta. A. Mol. Biomol. Spectrosc.*, 67(2):385–90, 2007.

[229] Shiling Yuan, Lixia Ma, Xiuqing Zhang, and Liqiang Zheng. Molecular dynamics studies on monolayer of cetyltrimethylammonium bromide surfactant formed at the air/water interface. *Colloids Surfaces A Physicochem. Eng. Asp.*, 289(1-3):1–9, 2006.

[230] Yiming Li, Yingyan Guo, Mutai Bao, and Xueli Gao. Investigation of interfacial and structural properties of CTAB at the oil/water interface using dissipative particle dynamics simulations. *J. Colloid Interface Sci.*, 361(2):573–80, 2011.

[231] Katja Knauf, Annette Meister, Andreas Kerth, and Alfred Blume. Interaction of alkyltrimethylammonium bromides with DMPC-d(54) and DMPG-d(54) monolayers studied by infrared reflection absorption spectroscopy (IRRAS). *J. Colloid Interface Sci.*, 342(2):243–52, 2010.

[232] Hiromichi Nakahara, Osamu Shibata, and Yoshikiyo Moroi. Examination of surface adsorption of cetyltrimethylammonium bromide and sodium dodecyl sulfate. *J. Phys. Chem. B*, 115(29):9077–86, 2011.

[233] Geyser Fernández Catá, Hansel Comas Rojas, Aurora Pérez Gramatges, Claudio M. Zicovich-Wilson, Luis Javier Álvarez, and Catherine Searle. Initial structure of cetyltrimethylammonium bromide micelles in aqueous solution from molecular dynamics simulations. *Soft Matter*, 7(18):8508, 2011.

[234] V. K. Sharma, S. Mitra, V. Garcia Sakai, P. A. Hassan, J. Peter Embs, and R. Mukhopadhyay. The dynamical landscape in CTAB micelles. *Soft Matter*, 8(27):7151, 2012.

[235] Thomas Ingram, Sandra Storm, Linda Kloss, Tanja Mehling, Sven Jakobtorweihen, and Irina Smirnova. Prediction of micelle/water and liposome/water partition coefficients based on molecular dynamics simulations, COSMO-RS, and COSMOmic. *Langmuir*, 29(11):3527–37, 2013.

[236] D. P. Tieleman and H. J. C. Berendsen. http://wcm.ucalgary.ca/tieleman/downloads Molecular dynamics simulations of a fully hydrated dipalmitoylphosphatidylcholine bilayer with different macroscopic boundary conditions and parameters. *J. Chem. Phys.*, 105(11):4871, 1996.

[237] Scott E. Feller, Yuhong Zhang, and Richard W. Pastor. Computer simulation of liquid/liquid interfaces. II. Surface tension-area dependence of a bilayer and monolayer. *J. Chem. Phys.*, 103(23):10267, 1995.

[238] Yuhong Zhang, Scott E. Feller, Bernard R. Brooks, and Richard W. Pastor. Computer simulation of liquid/liquid interfaces. I. Theory and application to octane/water. *J. Chem. Phys.*, 103(23):10252, 1995.

[239] Anna Skibinsky, Richard M. Venable, and Richard W. Pastor. A molecular dynamics study of the response of lipid bilayers and monolayers to trehalose. *Biophys. J.*, 89(6):4111–21, 2005.

[240] Jeffery B. Klauda, Xiongwu Wu, Richard W. Pastor, and Bernard R. Brooks. Long-range Lennard-Jones and electrostatic interactions in interfaces: application of the isotropic periodic sum method. *J. Phys. Chem. B*, 111(17):4393–400, 2007.

[241] Christine Peter and Kurt Kremer. Multiscale simulation of soft matter systems. *Faraday Discuss.*, 144:9, 2010.

[242] Roger L. McMullen and Stephen P. Kelty. Molecular dynamic simulations of eicosanoic acid and 18-methyleicosanoic acid langmuir monolayers. *J. Phys. Chem. B*, 111(37):10849–52, 2007.

[243] K.S. Birdi, D.T. Vu, L. Moesby, K.B. Andersen, and D. Kristensen. Structures of lipid and biopolymer monolayers investigated as Langmuir-Blodgett films by atomic force microscopy. *Surf. Coatings Technol.*, 67(3):183–191, 1994.

[244] M. Lipp, K. Lee, D. Takamoto, J. Zasadzinski, and A. Waring. Coexistence of Buckled and Flat Monolayers. *Phys. Rev. Lett.*, 81(8):1650–1653, 1998.

[245] Mark A. Borden and Marjorie L. Longo. Dissolution Behavior of Lipid Monolayer-Coated, Air-Filled Microbubbles: Effect of Lipid Hydrophobic Chain Length. *Langmuir*, 18(24):9225–9233, 2002.

[246] Rachel Sibug-Aga and Robert C. Dunn. High-resolution studies of lung surfactant collapse. *Photochem. Photobiol.*, 80(3):471–6, 2004.

[247] Amanda P. Siegel, Noor F. Hussain, Merrell Johnson, and Christoph A. Naumann. Metric between buckling structures and elastic properties in physisorbed polymer-tethered lipid monolayers. *Soft Matter*, 8(21):5873, 2012.

[248] Svetlana Baoukina, Luca Monticelli, Matthias Amrein, and D. Peter Tieleman. The molecular mechanism of monolayer-bilayer transformations of lung surfactant from molecular dynamics simulations. *Biophys. J.*, 93(11):3775–82, 2007.

[249] Wen-Xiong Shi and Hong-Xia Guo. Structure, interfacial properties, and dynamics of the sodium alkyl sulfate type surfactant monolayer at the water/trichloroethylene interface: a molecular dynamics simulation study. *J. Phys. Chem. B*, 114(19):6365–76, 2010.

[250] Hiroshi Noguchi. Anisotropic surface tension of buckled fluid membranes. *Phys. Rev. E*, 83(6):061919, 2011.

[251] D.R. Lide. *CRC Handbook of Chemistry and Physics, 85th Edition*. Taylor & Francis, Boca Raton, FL, 2004.

[252] Susan L. Duncan and Ronald G. Larson. Comparing experimental and simulated pressure area isotherms for DPPC. *Biophys. J.*, 94(8):2965–86, 2008.

[253] V. V. Yaminsky, B. W. Ninham, H. K. Christenson, and R. M. Pashley. Adsorption Forces between Hydrophobic Monolayers. *Langmuir*, 12(8):1936–1943, 1996.

[254] Nirmesh J. Jain, Pierre-antoine Albouy, and Dominique Langevin. Study of Adsorbed Monolayers of a Cationic Surfactant and an Anionic Polyelectrolyte at the Air Water Interface. Role of the Polymer Charge Density. *Langmuir*, 19(20):8371–8379, 2003.

[255] Eva Santini, Jürgen Krägel, Francesca Ravera, Libero Liggieri, and Reinhard Miller. Study of the monolayer structure and wettability properties of silica nanoparticles

and CTAB using the Langmuir trough technique. *Colloids Surfaces A Physicochem. Eng. Asp.*, 382(1-3):186–191, 2011.

[256] Anna Zdziennicka and Bronisław Jańczuk. Behavior of cationic surfactants and short chain alcohols in mixed surface layers at water-air and polymer-water interfaces with regard to polymer wettability. I. Adsorption at water-air interface. *J. Colloid Interface Sci.*, 349(1):374–83, 2010.

[257] C. Stubenrauch, V. B. Fainerman, E. V. Aksenenko, and R. Miller. Adsorption behavior and dilational rheology of the cationic alkyl trimethylammonium bromides at the water/air interface. *J. Phys. Chem. B*, 109(4):1505–9, 2005.

[258] V. Matti J. Säily, Juha-Matti Alakoskela, Samppa J. Ryhänen, Mikko Karttunen, and Paavo K. J. Kinnunen. Characterization of Sphingosine Phosphatidylcholine Monolayers: Effects of DNA. *Langmuir*, 19(21):8956–8963, 2003.

[259] Berk Hess. Determining the shear viscosity of model liquids from molecular dynamics simulations. *J. Chem. Phys.*, 116(1):209, 2002.

[260] Sukit Leekumjorn and Amadeu K Sum. Molecular characterization of gel and liquid-crystalline structures of fully hydrated POPC and POPE bilayers. *J. Phys. Chem. B*, 111(21):6026–33, 2007.

[261] Lucie Huynh, Nahuel Perrot, Veronica Beswick, Véronique Rosilio, Patrick a Curmi, Alain Sanson, and Nadège Jamin. Structural properties of POPC monolayers under lateral compression: computer simulations analysis. *Langmuir*, 30(2):564–73, 2014.

[262] Howard E. Alper, Donna Bassolino-Klimas, and Terry R. Stouch. The limiting behavior of water hydrating a phospholipid monolayer: A computer simulation study. *J. Chem. Phys.*, 99(7):5547, 1993.

[263] Amarjeet Singh and Oleg Konovalov. Measuring elastic properties of a protein monolayer at water surface by lateral compression. *Soft Matter*, 9(10):2845, 2013.

[264] Steven W. Rick, Steven J. Stuart, and B. J. Berne. Dynamical fluctuating charge force fields: Application to liquid water. *J. Chem. Phys.*, 101(7):6141, 1994.

[265] Jacob D. Durrant and J. Andrew McCammon. HBonanza: a computer algorithm for molecular-dynamics-trajectory hydrogen-bond analysis. *J. Mol. Graph. Model.*, 31:5–9, 2011.

[266] S. W. Chiu, M. Clark, V. Balaji, S. Subramaniam, H. L. Scott, and E. Jakobsson. Incorporation of surface tension into molecular dynamics simulation of an interface: a fluid phase lipid bilayer membrane. *Biophys. J.*, 69(4):1230–45, 1995.

[267] P.-L. Chau and A. J. Hardwick. A new order parameter for tetrahedral configurations. *Mol. Phys.*, 93(3):511–518, 1998.

[268] Christofer Hofsäss, Erik Lindahl, and Olle Edholm. Molecular dynamics simulations of phospholipid bilayers with cholesterol. *Biophys. J.*, 84(4):2192–206, 2003.

[269] X. Zhai and J. M. Kleijn. Order in phospholipid Langmuir-Blodgett monolayers determined by total internal reflection fluorescence. *Biophys. J.*, 72(6):2651–9, 1997.

[270] J. Yang and J. M. Kleijn. Order in phospholipid Langmuir-Blodgett layers and the effect of the electrical potential of the substrate. *Biophys. J.*, 76:323–332, 1999.

[271] H. I. Petrache, S. W. Dodd, and M. F. Brown. Area per lipid and acyl length distributions in fluid phosphatidylcholines determined by (2)H NMR spectroscopy. *Biophys. J.*, 79(6):3172–92, 2000.

[272] Jean-Paul Douliez, Alain Léonard, and Erick J. Dufourc. Restatement of order parameters in biomembranes: calculation of C-C bond order parameters from C-D quadrupolar splittings. *Biophys. J.*, 68(5):1727–39, 1995.

[273] Sagar A. Pandit, David Bostick, and Max L. Berkowitz. Molecular dynamics simulation of a dipalmitoylphosphatidylcholine bilayer with NaCl. *Biophys. J.*, 84(6):3743–50, 2003.

[274] David Poger and Alan E. Mark. Lipid Bilayers: The Effect of Force Field on Ordering and Dynamics. *J. Chem. Theory Comput.*, 8(11):4807–4817, 2012.

[275] David Poger, Wilfred F. Van Gunsteren, and Alan E. Mark. A new force field for simulating phosphatidylcholine bilayers. *J. Comput. Chem.*, 31(6):1117–25, 2010.

[276] Andreas Kukol. Lipid Models for United-Atom Molecular Dynamics Simulations of Proteins. *J. Chem. Theory Comput.*, 5(3):615–626, 2009.

[277] Céline Anézo, Alex H. de Vries, Hans-Dieter Höltje, D. Peter Tieleman, and Siewert-Jan Marrink. Methodological Issues in Lipid Bilayer Simulations. *J. Phys. Chem. B*, 107(35):9424–9433, 2003.

[278] John F. Nagle and Stephanie Tristram-Nagle. Structure of lipid bilayers. *Biochim. Biophys. Acta - Rev. Biomembr.*, 1469(3):159–195, 2000.

[279] Wei Zhao, Andrey A. Gurtovenko, Ilpo Vattulainen, and Mikko Karttunen. Cationic dimyristoylphosphatidylcholine and dioleoyloxytrimethylammonium propane lipid bilayers: atomistic insight for structure and dynamics. *J. Phys. Chem. B*, 116(1):269–76, 2012.

[280] T. Brumm, C. Naumann, E. Sackmann, A.R. Rennie, R.K. Thomas, D. Kanellas, J. Penfold, and T.M. Bayerl. Conformational changes of the lecithin headgroup in monolayers at the air/water interface. *Eur. Biophys. J.*, 23(4):289–295, 1994.

[281] H. Möhwald. Phospholipid and phospholipid-protein monolayers at the air/water interface. *Annu. Rev. Phys. Chem.*, 41:441–76, 1990.

[282] Gang Ma and Heather C. Allen. DPPC Langmuir monolayer at the air-water interface: probing the tail and head groups by vibrational sum frequency generation spectroscopy. *Langmuir*, 22(12):5341–9, 2006.

[283] H. Dominguez, A. M. Smondyrev, and M. L. Berkowitz. Computer Simulations of Phosphatidylcholine Monolayers at Air/Water and CCl 4 /Water Interfaces. *J. Phys. Chem. B*, 103(44):9582–9588, 1999.

[284] Delara Mohammad-Aghaie, Emilie Macé, Charles A. Sennoga, John M. Seddon, and Fernando Bresme. Molecular dynamics simulations of liquid condensed to liquid expanded transitions in DPPC monolayers. *J. Phys. Chem. B*, 114(3):1325–35, 2010.

[285] Ruthven N. A. Lewis, Nanette Mak, and Ronald N. McElhaney. A differential scanning calorimetric study of the thermotropic phase behavior of model membranes composed of phosphatidylcholines containing linear saturated fatty acyl chains. *Biochemistry*, 26(19):6118–26, 1987.

[286] Linda R. De Young and Ken A. Dill. Solute partitioning into lipid bilayer membranes. *Biochemistry*, 27(14):5281–9, 1988.

[287] Alexander M. Smondyrev and Max L. Berkowitz. United atom force field for phospholipid membranes: Constant pressure molecular dynamics simulation of dipalmitoylphosphatidicholine/water system. *J. Comput. Chem.*, 20(5):531–545, 1999.

[288] Kechuan Tu, Douglas J. Tobias, J. Kent Blasie, and Michael L. Klein. Molecular dynamics investigation of the structure of a fully hydrated gel-phase dipalmitoylphosphatidylcholine bilayer. *Biophys. J.*, 70(2):595–608, 1996.

[289] J. J. López Cascales, T. F. Otero, A. J. Fernandez Romero, and L. Camacho. Phase transition of a DPPC bilayer induced by an external surface pressure: from bilayer to monolayer behavior. a molecular dynamics simulation study. *Langmuir*, 22(13):5818–24, 2006.

[290] G. Buldt, H. U. Gally, A. Seelig, J. Seelig, and G. Zaccai. Neutron diffraction studies on selectively deuterated phospholipid bilayers. *Nature*, 271(5641):182–184, 1978.

[291] W. L. Vaz, R. M. Clegg, and D. Hallmann. Translational diffusion of lipids in liquid crystalline phase phosphatidylcholine multibilayers. A comparison of experiment with theory. *Biochemistry*, 24(3):781–6, 1985.

[292] P. F. Almeida, W. L. Vaz, and T. E. Thompson. Lateral diffusion in the liquid phases of dimyristoylphosphatidylcholine/cholesterol lipid bilayers: a free volume analysis. *Biochemistry*, 31(29):6739–47, 1992.

[293] S. Konig, W. Pfeiffer, T. Bayerl, D. Richter, and E. Sackmann. Molecular dynamics of lipid bilayers studied by incoherent quasi-elastic neutron scattering. *J. Phys. II France*, 2(8):1589–1615, 1992.

[294] J. J. Giner Casares, L. Camacho, M. Martín-Romero, and J. López Cascales. Effect of Na+ and Ca2+ ions on a lipid Langmuir monolayer: an atomistic description by molecular dynamics simulations. *Chemphyschem*, 9(17):2538–2543, 2008.

[295] Peter Ahlstrom and Herman J. C. Berendsen. A molecular dynamics study of lecithin monolayers. *J. Phys. Chem.*, 97(51):13691–13702, 1993.

[296] Pentti Somerharju, Jorma A. Virtanen, and Kwan Hon Cheng. Lateral organisation of membrane lipids. The superlattice view. *Biochim. Biophys. Acta*, 1440(1):32–48, 1999.

[297] Raymond M. Schiffelers, Aslam Ansari, Jun Xu, Qin Zhou, Qingquan Tang, Gert Storm, Grietje Molema, Patrick Y. Lu, Puthupparampil V. Scaria, and Martin C. Woodle. Cancer siRNA therapy by tumor selective delivery with ligand-targeted sterically stabilized nanoparticle. *Nucleic Acids Res.*, 32(19):1–10, 2004.

[298] Baojian Li, Qingquan Tang, Du Cheng, Chuan Qin, Frank Y Xie, Qiang Wei, Jun Xu, Yijia Liu, Bojian Zheng, Martin C Woodle, Nanshan Zhong, and Patrick Y Lu. Using siRNA in prophylactic and therapeutic regimens against SARS coronavirus in Rhesus macaque. *Nat. Med.*, 11(9):944–51, 2005.

[299] Jinkang Wang, Xin Guo, Yuhong Xu, Lee Barron, and Francis C Szoka. Synthesis and characterization of long chain alkyl acyl carnitine esters. Potentially biodegradable cationic lipids for use in gene delivery. *J. Med. Chem.*, 41(13):2207–15, 1998.

[300] Purnendu Chakraborty and Michael R. Zachariah. "Effective" negative surface tension: a property of coated nanoaerosols relevant to the atmosphere. *J. Phys. Chem. A*, 111(25):5459–64, 2007.

[301] Harvey T. McMahon and Jennifer L. Gallop. Membrane curvature and mechanisms of dynamic cell membrane remodelling. *Nature*, 438(7068):590–596, 2005.

[302] A. Tian and T. Baumgart. Sorting of lipids and proteins in membrane curvature gradients. *Biophys. J.*, 96(7):2676–2688, 2009.

[303] Andrey Ivankin, Ivan Kuzmenko, and David Gidalevitz. Cholesterol mediates membrane curvature during fusion events. *Phys. Rev. Lett.*, 108(23):1–5, 2012.

[304] Semen O. Yesylevskyy and Alexander P. Demchenko. How cholesterol is distributed between monolayers in asymmetric lipid membranes. *Eur. Biophys. J.*, 41(12):1043–54, 2012.

[305] Semen O. Yesylevskyy. Pteros: Fast and easy to use open-source C++ library for molecular analysis. *J. Comput. Chem.*, 33(19):1632–1636, 2012.

[306] S. O. Yesylevskyy, S. Kraszewski, and C. Ramseyer. Determination of the shape and curvature of nonplanar lipid bilayers that are bent in a single plane in molecular dynamics simulations. *J. Mol. Model.*, 20(4), 2014.

[307] Semen O. Yesylevskyy. Pteros 2.0: Evolution of the fast parallel molecular analysis library for C++ and python. *J. Comput. Chem.*, 36:1480–1488, 2015.

[308] Derek Marsh. Lateral pressure profile, spontaneous curvature frustration, and the incorporation and conformation of proteins in membranes. *Biophys. J.*, 93(11):3884–3899, 2007.

[309] Hayato Shiba and Hiroshi Noguchi. Estimation of the bending rigidity and spontaneous curvature of fluid membranes in simulations. *Phys. Rev. E*, 84(3):031926, 2011.

[310] Benjamin Kollmitzer, Peter Heftberger, Michael Rappolt, and Georg Pabst. Monolayer spontaneous curvature of raft-forming membrane lipids. *Soft Matter*, 9(45):10877–10884, 2013.

[311] Xin Wang and Markus Deserno. Determining the pivotal plane of fluid lipid membranes in simulations. *J. Chem. Phys.*, 143(16):164109, 2015.

[312] Mingyang Hu, Djurre H. de Jong, Siewert J. Marrink, and Markus Deserno. Gaussian curvature elasticity determined from global shape transformations and local stress distributions: a comparative study using the MARTINI model. *Faraday Discuss.*, 161:365–382, 2013.

[313] C. Vilhena and A. Bettencourt. Daptomycin: A review of properties, clinical use, drug delivery and resistance. *Mini-Reviews in Medicinal Chemistry*, 12(3):202–209, 2012.

[314] Siewert J. Marrink, Alex H. de Vries, and D. Peter Tieleman. Lipids on the move: Simulations of membrane pores, domains, stalks and curves. *Biochim. Biophys. Acta - Biomembr.*, 1788(1):149–168, 2009.

[315] W. F. Drew Bennett, Nicolas Sapay, and D. Peter Tieleman. Atomistic simulations of pore formation and closure in lipid bilayers. *Biophys. J.*, 106(1):210–219, 2014.

[316] Wei Zhao, Tomasz R??g, Andrey A. Gurtovenko, Ilpo Vattulainen, and Mikko Karttunen. Role of phosphatidylglycerols in the stability of bacterial membranes. *Biochimie*, 90(6):930–938, 2008.

[317] George M Eliopoulos, Claudie Thauvin, Benjamin Gerson, and Robert C Moellering. In Vitro Activity and Mechanism of Action of A21978C1 , a Novel Cyclic Lipopeptide Antibiotic L-Asp L-Orn D-Ser L-Kyn L-Asp. *Antimicrob. Agents Chemother.*, 27(3):357–362, 1985.

[318] G. M. Torrie and J. P. Valleau. Nonphysical sampling distributions in Monte Carlo free-energy estimation: Umbrella sampling. *J. Comput. Phys.*, 23(2):187–199, 1977.

[319] Jochen S. Hub, Bert L. de Groot, and David van der Spoel. g-whams-A free Weighted Histogram Analysis implementation including robust error and autocorrelation estimates. *J. Chem. Theory Comput.*, 6(12):3713–3720, 2010.

[320] Mohsen Pourmousa and Mikko Karttunen. Early stages of interactions of cell-penetrating peptide penetratin with a DPPC bilayer. *Chem. Phys. Lipids*, 169:85–94, 2013.

[321] Tristan Bereau, W. F Drew Bennett, Jim Pfaendtner, Markus Deserno, and Mikko Karttunen. Folding and insertion thermodynamics of the transmembrane WALP peptide. *J. Chem. Phys.*, 143(24), 2015.

[322] Steven Kirkham, Valeria Castelletto, Ian W. Hamley, Katsuaki Inoue, Robert Rambo, Mehedi Reza, and Janne Ruokolainen. Self-Assembly of the Cyclic Lipopeptide Daptomycin: Spherical Micelle Formation does not Depend on the Presence of Calcium Chloride. *ChemPhysChem*, (17):1–6, 2016.

[323] Jan Grünewald, Stephan A. Sieber, Christoph Mahlert, Uwe Linne, and Mohamed A. Marahiel. Synthesis and derivatization of daptomycin: A chemoenzymatic route to acidic lipopeptide antibiotics. *J. Am. Chem. Soc.*, 126(51):17025–17031, 2004.

[324] Chuda Raj Lohani, Robert Taylor, Michael Palmer, and Scott D. Taylor. Solid-phase synthesis and in vitro biological activity of a Thr4Ser4 analog of daptomycin. *Bioorg. Med. Chem. Lett.*, 25(23):5490–5494, 2015.

[325] Tianhua Zhang. *Daptomycin : Mechanism of action and bacterial resistance*. PhD thesis, University of Waterloo, 2014.

[326] Jirasak Wong-ekkabut and Mikko Karttunen. Molecular dynamics simulation of water permeation through the alpha-hemolysin channel. *J. Biol. Phys.*, 42(1):133–146, 2016.

[327] Niels Hansen and Wilfred F. Van Gunsteren. Practical aspects of free-energy calculations: A review. *J. Chem. Theory Comput.*, 10(7):2632–2647, 2014.